Measurement of the top-quark pair production cross section with soft muon b-tagging in pp collisions at $\sqrt{s} = 7$ TeV with the ATLAS detector

Andrew James Poll

A thesis submitted in fulfilment of the requirements
for the degree of Doctor of Philosophy to

Queen Mary University of London

2011

Declaration

The work presented in this thesis was undertaken for the international collaboration of the ATLAS experiment on particle physics. Therefore, though it contains a significant amount of original work by the author it is based on the work of predecessors and collaborators. Chapter 2 is a summary of previous work by the ATLAS collaboration on the design of the detector and its many elements. Chapter 3 covers the motivation of this study from a theoretical point of view and gives a brief historical account of works by numerous authors referenced where appropriate.

The general ATLAS software used for this analysis was built by the collaboration over many years, but chapter 6 contains all original analysis coding by the author. Chapter 7 utilises the InsituMuon software package referenced in that section with additions made by the author. Chapter 8 expands on the analysis coding from chapter 6 with additional work by the author on background determinations and cross section measurements.

Relevant systematic uncertainties in Chapter 8 are included from recent ATLAS Top Quark Group publications and are referenced where appropriate.

Abstract

This thesis presents a study of the measurement of the top pair production cross section in the semileptonic decay channel with soft muon b-tagging at the ATLAS detector using early LHC data. A theoretical overview of current research in particle physics, motivating the construction of the LHC and the ATLAS detector is discussed followed by the main motivations behind a measurement of the top cross section.

A summary of my work undertaken for the semiconductor tracker (SCT) collaboration on ATLAS, including shift work and the refurbishment of the SR1 barrel sector and spare endcap disk is detailed. Following this the electron isolation in top and Z boson events was examined with Monte Carlo simulated events to optimise the selection criteria for electrons from W boson decay in top events.

As part of the top cross section measurement, the efficiency and scale factor, compared to Monte Carlo studies, of using a χ^2_{match} cut on soft muons was calculated using the decay of the J/ψ in early LHC data. The last chapter details the development of an analysis framework and measurement of the top pair production in the semileptonic decay channel with soft muon b-tagging. This measurement builds on the work in the previous chapters utilising both the electron isolation requirement from Monte Carlo simulations and the scale factor on the soft muon χ^2_{match} cut for b-tagging to yield a measurement of the top cross section in 2.9 pb^{-1} of LHC data.

Acknowledgements

There are many people I would like to thank for their support and guidance during the course of my PhD, namely Lucio Cerrito (my supervisor), Steve Lloyd, Graham Thompson (who was always interested in an idea, no matter how crazy it may at first seem) and Eram Rizvi for their availability, assistance and helpful discussion throughout my time at Queen Mary. I would also like to thank the rest of the Queen Mary particle physics group for all their support during my time at the department, with special mention to Alex, Cozmin and Chris. I would also like to give a mention to the other students I have met during my time at QM, especially Akira (who first introduced me to the glorious early versions of the Atlas software), Melissa, Katy, Alex, Matilde, Elisa, Tom and Jack, you all made the office and working environment a friendly and welcoming place, long may it continue, you will all be missed. Also I doubt many of the problems I came across would have been fixed without the input and help of the post-docs at QM, big thanks to Ben, Kyle, John and Dan.

I would also like to mention a few people I have worked closely with from Royal Holloway while undertaking my PhD, Veronique Boisvert, Ricardo Goncalo and Matt Rose. The discussions, email correspondence and input to my analysis over the years was always gladly received and I thank you.

With 18 months spent working out at CERN I met and worked with many other colleagues and students who made the time living there one of the most memorable in my life. I would like to thank the members of the SCT collaboration (Sandra, Tom, Dave, Nick and many others) for their warm welcome to a complete stranger and showing me the in's and out's of their pride and joy. Thank you for entrusting me not to break it while on shift, I only wish I could have had more of a hand in building what is an amazing piece of hardware. I could not mention CERN without thanking the UK administration staff based at CERN for their assistance in all things related to working out there and STFC for funding this PhD. I'd like to give a special mention to the other PhD students I met and worked with while out at CERN, the time spent on conference in Chicago, skiing in white outs and cycling around Lake Léman really are things I will take with me for many years to come.

I could not write this thesis without the time and support given to me by my family. Most importantly I would like to thank my parents for the numerous times they have picked me up from the airport and driven my belongs to and from University over the years.

I have spent 8 years of my life at Queen Mary as first an undergraduate student and now a post-grad, the warm welcome and friendly atmosphere I experienced on my first day has continued throughout my time here and it will be sorely missed.

Contents

List of Figures

List of Tables

Chapter 1

Motivation

The study of elementary particles and the theory behind their interactions has for the past 35 years been governed by the Standard Model. It has had great success in predicting a number of interactions and particles that have subsequently been confirmed through experimental observation. The theory's robustness and accuracy has been confirmed through numerous experiments that have been performed since its inception.

This thesis focuses on proton-proton interactions produced at the Large Hadron Collider (LHC) at the European Organization for Nuclear Research (CERN). The LHC is to date the most powerful particle accelerator in operation with multiple detectors placed at collision points around the 27km ring. One of these detectors is the ATLAS detector which has been designed to study a wide range of physics processes with extremely high accuracy.

One area of particular interest where ATLAS will have a large role to play is in the potential discovery of the Higgs boson, one of the few remaining missing pieces of the Standard Model. Alongside the search for the Higgs the ATLAS detector will provide an ideal platform to refine current knowledge of known particles as well as searching for signs of new physics beyond that of the Standard Model.

The interactions that this thesis will focus on will be those when two top quarks are produced and the resultant particles from their decay detected. As the last quark to be discovered there still exists a certain amount of uncertainty about its various properties, such as why the mass of the top quark is ≈40 times larger than that of the bottom quark, its nearest in mass. There also exists the possibility that the large mass of the top quark could indicate that it has a special role in the electroweak symmetry breaking mechanism of the Higgs boson.

This thesis will focus on making a measurement of the cross section of the $t\bar{t}$ process in early data and a study into various aspects involved in the measurement. This measurement is important in establishing the top-quark production at ATLAS and verifying that the cross section is in agreement with expectations of QCD and that there are no new physics processes visible. Also in using the soft muon tagging algorithm in this measurement and validating it, it allows for the use of the tagging algorithm in other analyses at ATLAS.

Chapter 2

The Detector and the Collider

The story of the Standard Model is a long one that has been built up over many years of research and multitudes of different experiments and yet even after nearly half a century of research it does not explain everything that we see.

There are many different areas that are not complete in the Standard Model, for example it does not attempt to explain gravity in any way and requires the use of 19 numerical constants whose values are unrelated and arbitrary.

Thus the LHC was designed with the idea of probing the Standard Model and creating collisions an order of magnitude higher in energy and luminosity than those previously seen. With centre of mass energies of the order of $\sim$14 TeV it is hoped that the LHC will be able to help bridge the gaps that currently exist in our knowledge of the elementary particles and fundamental interactions.

To observe new states of matter and possible new interactions the ATLAS detector was designed to accurately measure the full range of fundamental particles and cover as many different models/scenarios as possible for new physics. The ATLAS detector will explore the TeV mass scale where ground-breaking discoveries are expected. A focus will also be placed on the investigation of electroweak symmetry breaking and linked to this the search for the Higgs boson and Physics beyond the Standard Model.

2.1 The Large Hadron Collider

The Large Hadron Collider (LHC) is situated in the 27 km long former Large Electron-Positron Collider (LEP) tunnel at CERN, Geneva, Switzerland. It is designed to accelerate two counter-rotating beams of protons that are delivered from the Super Proton Synchrontron (SPS). There are four main interaction points where there are detectors located. These include Point 1 (ATLAS detector), Point 2 (ALICE detector), Point 5 (CMS detector) and Point 8 (LHCb detector) as shown in Figure 2.1

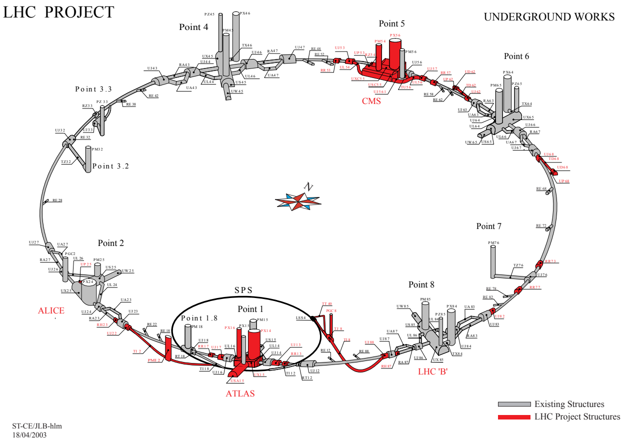

Figure 2.1: Schematic view of the LHC and SPS accelerator rings

The LHC first entered beam commissioning in September 2008 but 9 days later a fault occurred in the electrical connection between two of the superconducting dipole magnets that produced an electrical arc, compromising the liquid-helium containment. The resultant shock wave produced from the liquid-helium filling the vacuum was sufficient to break the 10 tonne magnets from their mountings.

Repairs to the LHC ring lasted until late November 2009 when the proton beams were successfully circulated once more at energies of 450 GeV. Shortly after on 30th of November 2009 the circulating beams reached an energy of 1.18 TeV per beam, surpassing the previous record held by the then current highest energy collider, the Tevatron at Fermilab.

On 30th March 2010 the LHC was started up again after winter shut down and achieved 3.5 TeV per beam, which till now is the energy the beams will be kept at until further upgrades are undertaken. These upgrades are planned for 2011 and are required as a result of the investigation into the incident that occurred in September 2008. It is currently planned that the LHC will produce $\sim 1fb^{-1}$ before the next shut down.

2.1.1 The Beam and Magnets

The performance requirements of the LHC set significant challenges for the design and construction of the accelerator. The LHC is the last part of a series of accelerator systems that are combined to produce the beam that finally circulates within the LHC itself.

The first system is the linear particle accelerator (LINAC 2) which generates 50 MeV protons that are fed into the Proton Synchrotron Booster (PSB). Within the PSB the protons are accelerated to 1.4 GeV and injected into the Proton Synchrotron (PS), where the protons energy reaches 26 GeV. The last stage before entering the LHC is the SPS which is used to further increase the protons energy to 450 GeV before they are at last injected into the LHC. Within the LHC the protons are accumulated into bunches of about 10^{11} particles that are then accelerated up to the desired energy, currently set at 3.5 TeV but with a design goal of 7 TeV.

To keep the beams circulating within the ring, the LHC employs 1,232 dipole (Fig 2.2) magnets, which cover $\sim$ 20 km of the ring length. The focusing of the beam is done using quadrupole magnets that boost the luminosity at the collision points. These quadrupole magnets are also employed along the straight sections of the ring and number 392 in total.

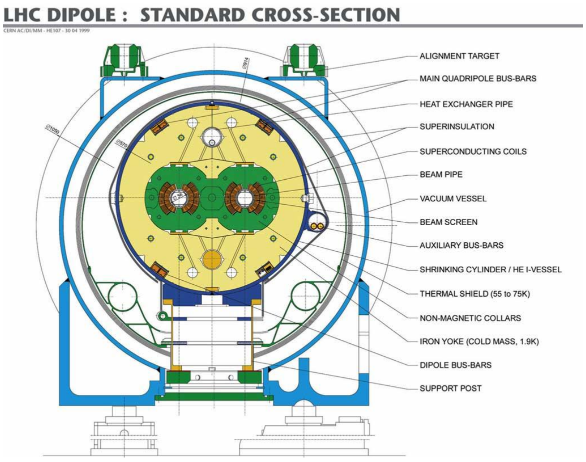

Figure 2.2: Cross section of the LHC dipole magnet system

One of the main drawbacks with any circular accelerator is synchrotron radiation, which is released as ultra relativistic charged particles are accelerated in a circular motion by magnet field. Indeed this was the main limiting factor for the LEP collider that inhabited the ring where the LHC now resides.

However, as the LHC is based on accelerating protons and not electrons/positrons the energy loss incurred is much less. The energy loss due to synchrotron radiation in an accelerator ring of radius R per revolution is:

$$\delta E = \tfrac{4\pi e^2}{3R}\beta^3\gamma^4$$

where $v = \beta c$ and $E = \gamma mc^2$. In the case of the LEP collider a 50 GeV electron has a γ of 98,000 while a proton in the LHC would have a γ of 54 for the same energy.

Although the problem associated with having a circular ring could be solved by having a linear accelerator, the benefit of keeping 2808 bunches circulating creates a far higher luminosity over time than what would be achieved with a linear accelerator. The luminosity, the number of events per unit cross-section of a circulating accelerator is given by:

$$Luminosity = nf\tfrac{N_1 N_2}{A}$$

where there are n bunches in each beam revolving at a frequency f, with N_1 and N_2

particles in the colliding bunches with an overlapping area of A.

The LHC is designed as a discovery machine, the collisions that occur between the two proton beams will generally create “messy” events with large number of particles in them. The focus of the physics programmes will tend to be searches for signatures of new physics, that could have large implications on our current understanding, these signatures are likely to appear in events where the centre of mass energy is at its highest. The high luminosity and increased cross-sections at the LHC will enable further high precision tests of QCD, electroweak interactions, and flavour physics.

2.1.2 Event Rate and Pile Up

The design luminosity of the LHC envisaged a peak luminosity of $10^{34} cm^{-2} s^{-1}$ that would produce on average 23 interactions per bunch crossing [1], varying according to a Poisson distribution. With the starting luminosity expected to be a factor of 100 less than the optimal running (assuming the same number of bunches in each case) we expect to see a mean of 0.23 events per bunch crossing.

In early running the effect of multiple events per bunch crossing, known as pile up, is therefore expected to be low and when an event is triggered there is most likely only going to be one interaction. However in later running as the luminosity increases the effect of multiple interactions per bunch crossing is going to be closely monitored to account for it in the calibrations, such as in the background subtraction in the calorimeter.

2.2 The ATLAS Detector

ATLAS is an acronym for **A** **T**oroidal **L**HC **A**pparatu**S**

Figure 2.3 shows an overview of the ATLAS detector with the main components listed as follows; the inner detector, electromagnetic (EM) calorimeter, hadronic calorimeter, muon spectrometer and magnet system.

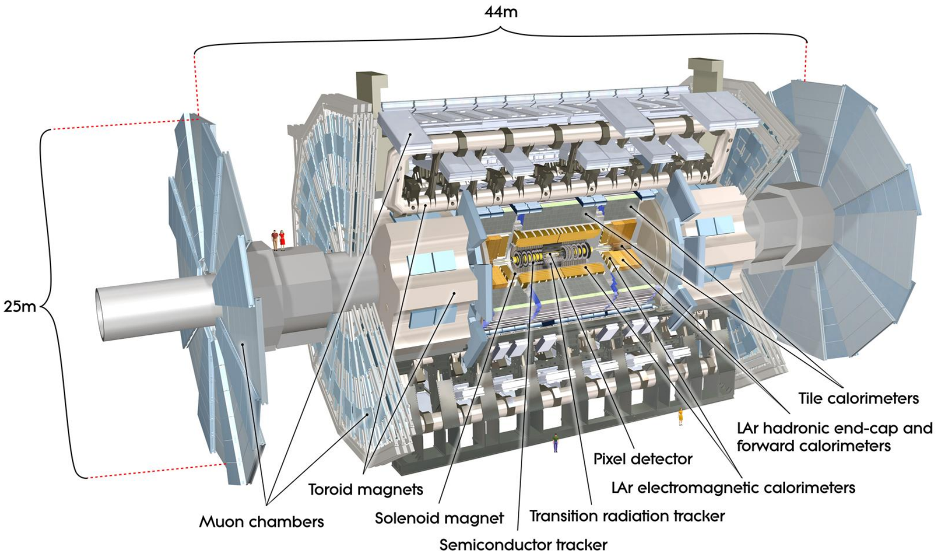

Figure 2.3: Overview of the ATLAS detector layout [1].

2.2.1 Physics at ATLAS

Placed at Point 1 on the LHC ring the ATLAS detector is one of the largest particle detectors ever built and the collaboration consists of more than 2000 physicists.

The ATLAS detector is one of two “general purpose detectors” that are placed on the LHC ring, the other being CMS. They are designed to take advantage of the rich physics potential of the LHC to perform more precise measurements of the Standard Model parameters and to search for new physics phenomena.

One of the main considerations when designing ATLAS was to ensure that the detector would maximise its discovery potential for the long sought after Higgs particle. Depending on its mass, the Higgs has a number of different production mechanisms. These range from photon pairs, $H \rightarrow ZZ \rightarrow 4l$ ($l =$ muons or electrons).

To cover all the possible decay modes of the Higgs particle and allow for the full range of discovery potential the ATLAS detector has been designed as general purpose detector with excellent particle identification, excellent calorimetry and excellent tracking and vertex detection, details of which are covered in the next section.

2.2.2 Important Definitions

A common set of coordinate axes are defined within ATLAS, with the z axis oriented along the beam pipe, and x and y axes defined as shown in Figure 2.4. The x axis is horizontal and points from the interaction point towards the centre of the LHC ring. The y axis is perpendicular to the x axis and points upwards; it is inclined by 1.23% with respect to the local vertical. This inclination of the y axis is because the detector is inclined to follow the beam slope. The cylindrical coordinates radial coordinate $r = \sqrt{x^2 + y^2}$ is sometimes also used. ϕ is measured around the z axis and pseudo-rapidity η is measured from the beam axis around the point of interaction as shown.

Pseudo-rapidity, η defined as:

$$\eta = -\ln(\tan\frac{\theta}{2}) \tag{2.1}$$

and the difference in pseudo-rapidity between two particles independent of Lorentz boosts along the beam axis.

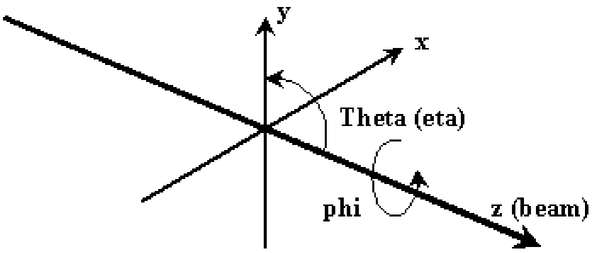

Figure 2.4: Definition of the ATLAS coordinate system

Within the detector the $\eta - \phi$ space is used to define the position of a given particle.

The angular separation between two particles is measured as ΔR:

$$\Delta R = \sqrt{\Delta\phi^2 + \Delta\eta^2}, \tag{2.2}$$

where $\Delta\phi$ and $\Delta\eta$ are the differences in η and ϕ for the given two particles.

2.2.3 Overall Concept

To support a range of physics programmes envisaged, a series of general requirements were set for the detector:

- Due to the experimental environment of the LHC, the detectors require fast, radiation-hard electronics and sensor elements.
- Large acceptance in pseudo-rapidity and azimuthal angle.
- Good charged-particle momentum resolution and inner track reconstruction efficiency.
- Very good electromagnetic (EM) and hadronic calorimetry for identification of electrons, photons, jets and E_T^{miss}.
- Good muon reconstruction across a wide range of momenta.

The Atlas detector is nominally forward-backward symmetric with respect to the interaction point, about 44 metres long, 25 metres in diameter and weighs approximately 7000 tonnes.

Atlas is essentially divided up into 4 sub-detector systems moving from the beam interaction point out:

- The inner detector which is immersed in a 2 T solenoidal field, crucial for the measurement of charged particles;

- Liquid-argon calorimetry systems provide energy and position measurement for electromagnetic and hadronic particles;
- Muon spectrometer for identification and position measurements of muons;
- Outer eight-fold azimuthal magnet system for bending the trajectory of (charged particles) muons.

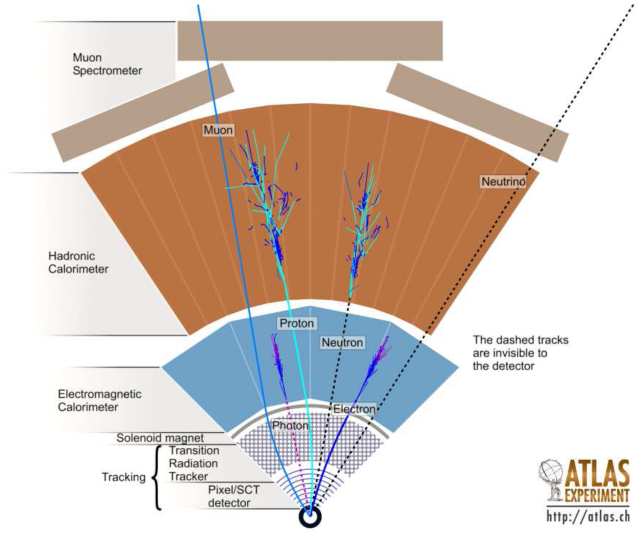

Figure 2.5: Schematic view of the particle detectors within Atlas responding to different particle types. Not drawn are the toroid magnets between the hadronic calorimeter and the muon spectrometer.

2.2.4 Inner Detector

The innermost detector module is aptly named the Inner Detector (Figure 2.6); it consists of three different types of tracking modules: the Pixel Detector, Semiconductor Tracker (SCT) and the Transition Radiation Tracker (TRT). At smaller $|\eta|$ the modules are placed parallel to the beam pipe but at larger $|\eta|$ their orientation is changed so that they are perpendicular to it (Table 2.1).

Closest to the beam pipe are the pixel detectors, they cover the region of $|\eta| < 2.5$. From 4 cm to 13 cm from the beam pipe, coverage is provided by three layers of pixel detectors. The pixel modules within the inner detector provide the highest granularity of all the components in the detector but at a high financial cost, therefore the number of layers is limited to 3. With a fine resolution of 12 μm in $\eta - \phi$ and 66 μm in z the pixel detector is very well suited to the detection and identification of the secondary vertices caused by $b-$ and $c-$flavoured hadrons and τ leptons. The innermost layer of the pixel detector is critical for reconstructing displaced vertices from b-quark decays and is referred to as the "b-layer".

Surrounding the pixel detector is the SCT, it consists of 4 barrel layers and 9 end-cap disks that span the radius from 30 cm to 52 cm. It is designed to provide up to 8 measurements per track with a resolution of 16 μm in $\eta - \phi$ and 580 μm in z. The SCT within ATLAS provides a surface area an order of magnitude larger than that of previous generations of silicon microstrip detectors.

The TRT detector is made up of a large number of straws that detect the transition-radiation photons given off as charged particles pass through the foils of radiator material that are placed between the straws. It is expected that the TRT will provide up to 36 measurements per track on average covering the detector radius up to 107 cm with a resolution of 170 μm per straw.

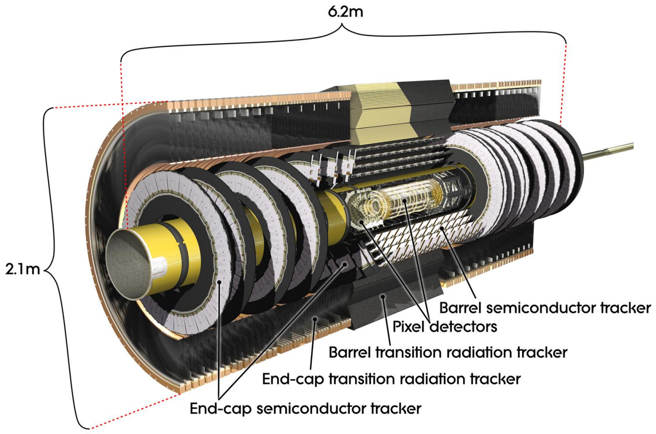

Figure 2.6: Overview of the ATLAS Inner Detector, with labels and dimensions. [1]

2.2.5 Calorimeter

The Atlas calorimeter, see Figure 2.7, is one of the central components used for the triggering of events and energy measurements. It consists of three main parts: the electromagnetic (EM) calorimeter, the hadronic calorimeter, and forward calorimeters. All play an important role for electron/photon identification and measurements of missing transverse energy ($\not\!\!E_T$), the total vector momentum sum of an event, electron, photon and jet energy.

There are two main sections to the calorimeter, the barrel and the end-cap regions that are both lead-liquid argon (LAr) detectors with accordian-shaped kapton electrodes and lead absorber plates over its full coverage. The accordion-shaped Kapton electrodes are designed in such a way that they give complete ϕ coverage without azimuthal cracks over the covered area. The total thickness of the EM calorimeter is > 22 radiation lengths (X_0) in the barrel and $> 24X_0$ in the end-caps. In the region of $|\eta| < 1.8$, a presampler detector is employed to correct for the energy lost by electrons and photons upstream of the calorimeter. This is achieved by measuring the multiplicity of a particle shower that develops due to interactions with inactive material. The amount of inactive material in front of the calorimeter varies between 1 X_0 and 3 X_0, with occasional spikes towards 5 X_0 close to the beampipe.

In the forward regions and the end-cap ($\sim 1.5 < |\eta| < 4.9$) the LAr is also used for hadronic calorimetry but the majority of detection in the barrel is covered by a sampling calorimeter called the tile calorimeter. The tile calorimeter is made from different materials to that of the LAr and instead uses iron as the absorber and scintillating tiles

$\lvert\eta\rvert$	0	0.7	1.4	1.7	2.5
Pixel	3 barrel layers			5 end-cap disks	
SCT	4 barrel layers		9 end-cap disks		
TRT	barrel layers	end-cap disks			

Table 2.1: Inner detector placement.

are placed radially to the beam.

For photons or electrons of moderate transverse energy (E_T) (50 GeV), the combined energy resolution of the EM calorimeter is expected to be of the order 1.6% or better. For lower energy photons or electrons (10 GeV) the total resolution is about 5% in the barrel and 3% in the end cap.

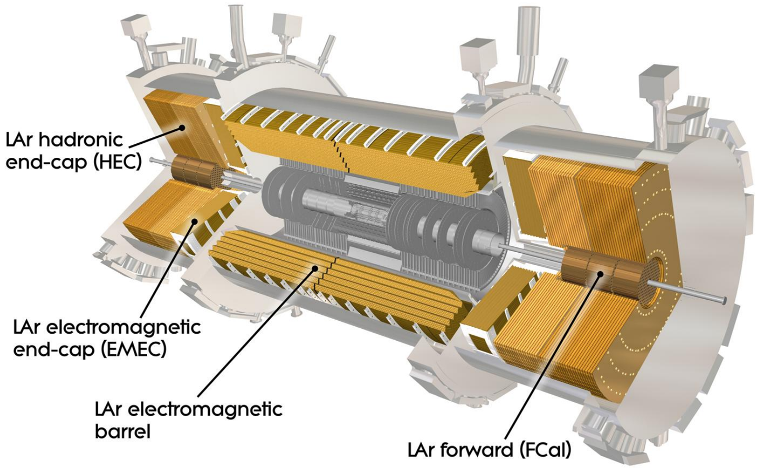

Figure 2.7: The ATLAS calorimeter system.

$\|\eta\|$	0	0.5	1.0	1.5	2.0	2.5	3.0	3.5	4.0	4.5	5.0
EM	barrel			end-cap							
Hadronic	barrel			end-cap							
Forward							forward				

Table 2.2: Relative calorimeter placement, rounded to nearest 0.5 in η.

2.2.6 Magnet System

The ATLAS magnet system is shown in Figure 2.8. The inner magnet system, the central solenoid (CS), enables ATLAS to take momentum measurements on charged particles within the inner detector, it is placed around the inner detectors in front of the EM calorimeter. The $2T$ magnetic field runs parallel to the beam pipe and will bend any charged particles that enter the field.

In the region outside the hadronic calorimeter and within the barrel region (BT) of the detector there are eight toroid magnets that generate a circular field centered in the beam pipe. The 8 coils of the toroid magnet are assembled radially around the beam and the peak field strength is $3.9T$. The use of toroidal magnets was chosen because a solenoid magnet of sufficient size would be prohibitively expensive to build and momentum measurements in the large volume of the muon system are not required to be as precise.

At the far ends of the detector are the End-cap toroids (ECT), installed either side of the BT they produce a magnetic field of $4.1T$. The coils in the ECT have been rotated by 22.5° with respect to the BT system to provide a radial overlap. As superconducting magnets both the BT and ECT are cooled down to $4.5K$ by enclosing them within aluminium casings and using liquid helium to hold them at temperature. The BT roughly covers the range $|\eta| < 1.0$ and from $1.4 < |\eta| < 2.7$ the ECT field is dominant. In the area between these two regions the effective field is a combination of the two.

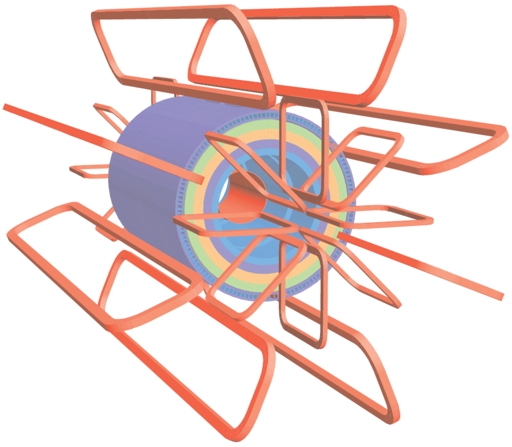

Figure 2.8: The magnet system (CS, BT and ECT) [1].

2.2.7 Muon Spectrometer

There are two main sections of the muon system, see Figure 2.9: the barrel region and the end-cap region. In the barrel region the muon chambers are arranged cylindrically and in the end-cap region they are instead placed perpendicular to the beam direction. In each region there is both one tracking section and one trigger section.

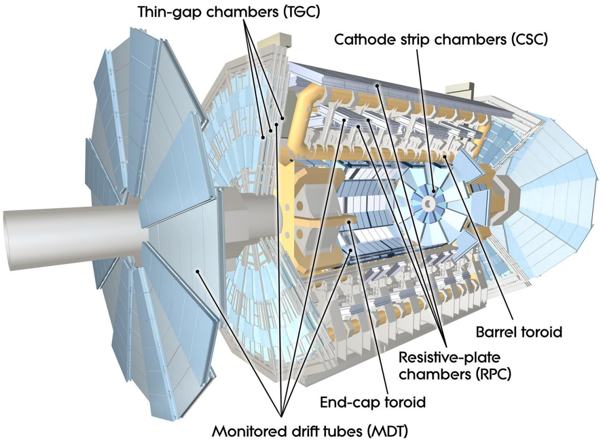

Figure 2.9: The ATLAS muon system.

The muon spectrometer in the barrel consists of Monitored Drift Tubes (MDT's) which are used for tracking. They are aluminium gas chambers with a wire in the centre and are arranged in multilayer pairs to help improve accuracy. The trigger section in the barrel comes from Resistive Plate Chambers (RPC's) and are used as they provide good time resolution for triggering. Between the plates of the RPC's there is a narrow gap filled with a gas mixture.

Located in the end-cap are the Cathode Strip Chambers (CSC's) and they are used for the precision measurements in this region. They are multi-wire proportional chambers with a cathode strip readout. For trigging in the end-caps, Thin Gap Chambers (TGC's) are instead used; they are are multi-wire proportional chambers whose anode wire pitch is larger than the cathode-anode distance.

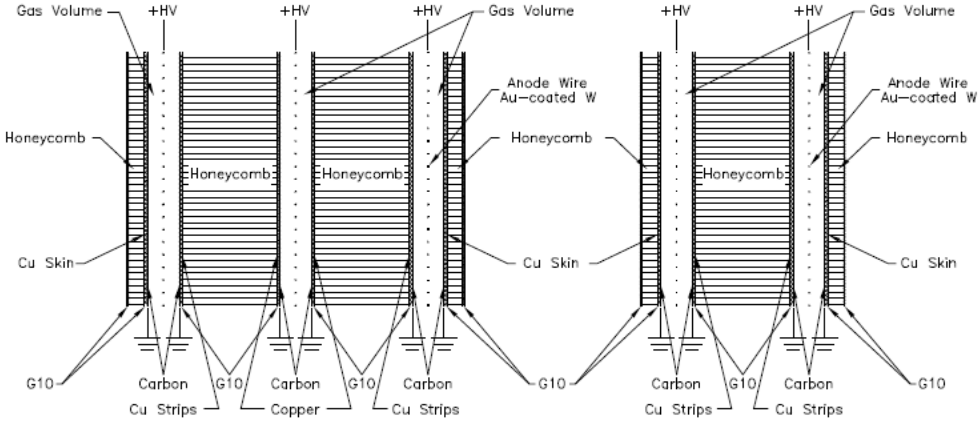

Figure 2.10: Cross-section of a TGC triplet and doublet module from the Atlas muon system. The triplet has three wire layers but only two strip layers. The dimensions of the gas gaps are enlarged with respect to the other elements.[1]

2.2.8 Trigger and Data Acquisition

At full luminosity the pp interaction rate within Atlas is of the order of 1 GHz [1] (bunch crossing rate 40 MHz with 23 interactions per bunch crossing). This creates far too much data to be stored. Most of this data is not interesting and as a result a trigger system, see Figure 2.11, has been designed to select events of interest, and record at a rate of $\sim$200 Hz with a rejection factor of 5×10^6 against the undesired minimum-bias events that produce many low-p_T particles.

The level-1 (LVL1 or L1) trigger makes the initial selection based on crude single or multiple object selections such as high-p_T electrons, photons, jets and τ-jets. There is also an initial E_T^{miss} and sum E_T calculation preformed that can also be trigged on. Information regarding the muon system comes from the RPCs and TGCs. The L1 decision is performed with custom integrated electronics with a maximum accept rate of 75 kHz (upgradable to 100 kHz) and a maximum latency of 2.5 μs.

When the L1 accepts an event it identifies regions of interest (ROI). The second level of trigger (LVL2 or L2) is then provided with the full detector information for that ROI. The L2 trigger further reduces the event rate to below 3.5 kHz, with an average event processing time of ∼40 ms.

The last stage of the Atlas trigger system is the event filter (EF) which uses offline analysis algorithms to further select events down to a rate of 200 Hz, with an average processing time per event of ∼4 s.

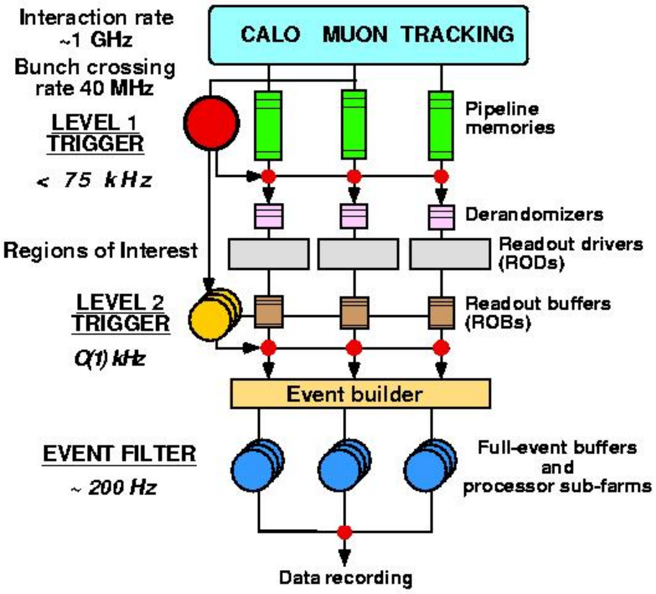

Figure 2.11: Block diagram of the Trigger system.

Chapter 3

Physics at the LHC

Our current knowledge of physics is based around the understanding of four fundamental interactions, namely: gravity, electromagnetism, the weak and strong interaction. For particle physics the effect of gravity is of minor importance since it is postulated that we would need to produce particles with energy of the order of the Planck scale (10^{19}GeV) before its effects would become important. The electromagnetic interaction, described by Quantum Electrodynamics (QED), is experienced by all charged particles and provides the binding forces in atoms and molecules. The weak interaction is present in a wide range of particle decays, including nuclear β decay and all processes involving neutrinos. The strong interaction is described by Quantum Chromodynamics (QCD) and only takes place between quarks and gluons.

It was in 1961 that one of the first milestones in particle physics happened. The unification of the electromagnetic and the weak interaction was proposed by Glashow[2]. Shortly after, in 1967 Glashow's electroweak theory included the Higgs mechanism [3] incorporated into it by Steven Weinberg and Abdus Salam [4, 5]. Glashow, Salam and Weinberg would later on be awarded the 1979 Nobel Prize in Physics for their work on the electroweak theory.

Following the work done by Gell-Mann [6] and Zweig [7] on the strong interaction and the quark model, experimental evidence throughout the mid 1970s confirmed that hadrons were composed of fractionally charged quarks.

Together the theories of electroweak interactions and QCD form the basis of the Standard Model and have been used to create the current table of fundamental particles (Table 3.1).

Particle Type	Name	Spin	Charge [e]	Mass
Quarks (Fermions)	up (u)	$\frac{1}{2}$	$+\frac{2}{3}$	1.5 to 3.3 MeV
	down (d)	$\frac{1}{2}$	$-\frac{1}{3}$	3.5 to 6.0 MeV
	charm (c)	$\frac{1}{2}$	$+\frac{2}{3}$	$1.27^{+0.07}_{-0.11}$ GeV
	strange (s)	$\frac{1}{2}$	$-\frac{1}{3}$	105^{+25}_{-35} MeV
	top (t)	$\frac{1}{2}$	$+\frac{2}{3}$	$171.3 \pm 1.1 \pm 1.2$ GeV
	bottom (b)	$\frac{1}{2}$	$-\frac{1}{3}$	$4.20^{+0.17}_{-0.07}$ GeV
Leptons (Fermions)	electron (e)	$\frac{1}{2}$	-1	0.511 MeV
	muon (μ)	$\frac{1}{2}$	-1	105.66 MeV
	tau (τ)	$\frac{1}{2}$	-1	1776.84 ± 0.27 MeV
	e-neutrino (ν_e)	$\frac{1}{2}$	0	$<<$ 1 MeV
	μ-neutrino (ν_μ)	$\frac{1}{2}$	0	$<<$ 1 MeV
	τ-neutrino (ν_τ)	$\frac{1}{2}$	0	$<<$ 1 MeV
Gauge Bosons	photon (γ)	1	0	0
	Gluon (g)	1	0	0
	$W^{\pm}$	1	± 1	80.398 ± 0.025 GeV
	Z^0	1	0	91.1876 ± 0.0021 GeV
Higgs Boson[1]	H^0	0	0	> 114.4 GeV

Table 3.1: The fundamental particles of the Standard Model.[8]

3.1 The Standard Model

The Standard Model has two types of fundamental particles accounting for all of known objects in the universe, these are called Leptons and Quarks. The model includes three generations of both leptons and quarks, with each generation consisting of two leptons and two quarks. This “family” of particles can be seen in Table 3.1 with each member also having its anti-particle, which creates a total of 12 leptons and 12 quarks as fundamental particles for the model.

---

[1] No observation to date.

The interaction of quarks and leptons with each other is determined by the properties and behaviours of the gauge bosons (Table 3.1) which are the force carriers in the Standard Model.

As all the forces of the Standard Model act on the top quark, I will give a brief summary of them.

3.1.1 Quantum Chromo-Dynamics (QCD)

The theory of the strong force in the Standard Model is Quantum Chromo-Dynamics (QCD), it describes the interactions of coloured particles. There are three colours, or quantum states, used in QCD, “red”, “blue” and “green” but they have nothing to do with colours of the visible electromagnetic spectrum. The strong interaction is mediated by 8 gauge bosons through the exchange of a quantum number, in this case colour.

Quarks come with a specific colour, but the observation of a free quark is not possible due to “confinement”, whereby the self-coupling of gluons, which occurs because they too are coloured, induces a larger potential at distance. Therefore all free particles appear as colour-singlet states called hadrons which are colourless combinations of quarks, anti-quarks and gluons. This process can be seen when a high momentum particle is incident on a quark in a hadron, the separated quarks undergo a process called “hadronisation” whereby the coloured quarks group themselves into colour-neutral objects such as new hadrons. These new objects which originate from the outgoing partons form a “jet” [9] which carries the momentum of the original quark.

The coupling strength of the strong force (α_s) has also been shown to be dependent on the interaction energy, Q. The strong coupling constant decreases logarithmically as a function of interaction energy, conversely this also means that it increases with decreasing energy making perturbative calculations at low energy extremely impossible. [10]

3.1.2 Quantum Electro-Dynamics (QED)

Quantum Electro-Dynamics (QED) is a combination of relativistic quantum field theory (QFT) and electrodynamics. It describes how light and matter interact and was the first theory that successfully combined quantum mechanics and special relativity.

QED describes electromagnetic effects by probabilities for the emission, flow and absorption of photons (γ). Photons act as the gauge bosons of the electromagnetic force, they have no rest mass, a spin of 1 and cannot interact with each other because they have no electric charge. The rules of QED apply to all electromagnetic phenomena with charged fundamental particles, such as electron-position annihilation and Compton scattering, (Figure 3.1).

The agreement between QED and experimental results has been stringently tested in various energy ranges and has been found to be correct to within ten parts in a billion (10^{-8}). This is based on the comparison between the electron anomalous magnetic dipole moment and the Rydberg constant from atomic recoil.[11, 12]

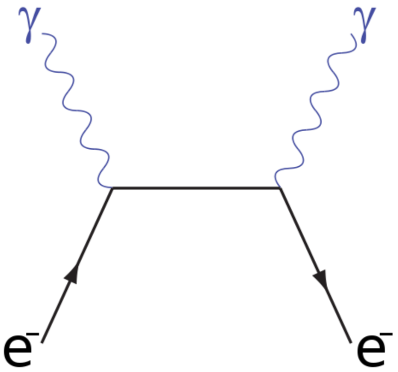

Figure 3.1: Compton scattering showing photon emission

3.1.3 The Weak and Electroweak Interaction

The weak interaction is mediated by the exchange of heavy W and Z bosons and the weak interaction is so aptly named because relative to the electromagnetic force is 10^{-11}

times weaker and some 10^{-13} times weaker than the strong force. The weak interaction was first postulated in the 1930s by Enrico Fermi [13] and experiments in subsequent years also established that it violates parity because it exclusively acts on left-handed particles.

The weak interaction is the only force within the Standard Model that allows for flavour changing, this can be seen clearly in β^- decay whereby one of the down quarks of the neutron changes to an up quark. This change occurs via the emission of a W^- boson which then goes on to decay into an electron and electron anti-neutrino, as shown in Figure 3.2.

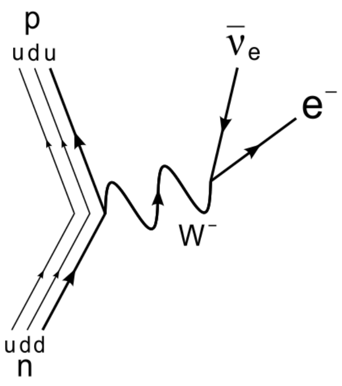

Figure 3.2: Feynman diagram for β^- decay.

The flavour-changing in the quark sector via the weak interaction is parametrised by the Cabbibio-Kobayashi-Maskawa (CKM) matrix [14, 15]. The CKM matrix, Eq. 3.1.3, allows for each generation of quarks to couple to other generations via the small off-diagonal elements. Flavour changing in the lepton sector was confirmed in 1998 by the observation of neutrino oscillation at the Super-Kamiokande experiment [16], implying that neutrinos have non-zero mass.

$$\begin{pmatrix} d^{'} \\ s^{'} \\ b^{'} \end{pmatrix} = \begin{pmatrix} V_{u,d} & V_{u,s} & V_{u,b} \\ V_{c,d} & V_{c,s} & V_{c,b} \\ V_{t,d} & V_{t,s} & V_{t,b} \end{pmatrix} \begin{pmatrix} d \\ s \\ b \end{pmatrix} \equiv \hat{V}_{CKM} \begin{pmatrix} d \\ s \\ b \end{pmatrix} \tag{3.1}$$

In 1961 Glashow put forward his theory of unification of the weak and electromagnetic interaction [2] and with further developments by Weinberg and Salam the theory was solidified. The existence of electroweak interactions was proven with the discovery of neutral current neutrino scattering at the Gargamelle experiment [17, 18, 19] in 1973. In 1983 the predicted force carriers of the electroweak force, the $W^{\pm}$ and Z^0, were discovered by the UA1 and UA2 experiments at CERN.

One of the major elements of the electroweak theory is the spontaneous symmetry breaking mechanism suggested by Higgs [3], which explains why the $W^{\pm}$, Z^0 and all other massive SM particles have mass. The Higgs mechanism also predicts the ratio between the W boson and Z boson masses as well as their couplings with each other and with the SM quarks and leptons. The LHC will cover the full range of potential Higgs masses in its search, for this boson which is currently not possible at Fermilab. Direct searches for the Higgs at LEP excluded a Higgs boson with a mass below 114.4 GeV with a 95% confidence level [20] and the Tevatron excluded a mass range between 158 GeV and 175 GeV at 95% confidence level [21]. The Standard Model requires that the Higgs to be is not heavier than ~ 1 TeV.

3.2 Beyond the Standard Model

One aspect of the Standard Model that leaves physicists puzzled is the fact that it requires 19 free parameters that can only be determined from experiment. More importantly, the Standard Model contains no particles with the right properties to form the dark matter that accounts for 83% of the known matter in the universe [22]. The existence of these gaps in the Standard Model predictions and others not mentioned here, has led physicists to look for ways to incorporate the ideas of the Standard Model into new theories.

One of the models that seems to solve some of the limitations of the Standard Model is Supersymmetry, or more commonly SUSY models. It is based on the premise that for every elementary particle with spin s there is a corresponding SUSY particle with spin $s - \frac{1}{2}$.

There currently exists no direct evidence for Supersymmetry and since no partners of any of the Standard Model particles have been observed to date, Supersysmmetry, if it exists, will be of a broken symmetry to allow the particles to be heavier than their corresponding Standard Model particles.

Although Supersymmetry has no evidence to date, it is appealing for a number of reasons, some of which are:

- If Supersymmetry exists close to the TeV energy scale it will allow for a solution to the hierarchy problem within the Standard Model, whereby quantum corrections to the couplings and masses within the Standard Model can lead to inconsistencies, especially in the case of the Higgs.
- Supersymmetry at the TeV scale also allows for the high-energy unification of the electroweak and strong interactions [23].
- It provides a number of dark matter candidates in the form of super-symmetric weakly interacting massive particles (WIMPS), thought to have around 100 times the mass of a proton.

Supersymmetry, although quite appealing, is just one of a large number of different theories that have been put forward to help explain the inconsistencies of the Standard Model. However at the moment the Standard Model has preformed remarkably well with any measured phenomena seen in particle physics and its parameters are continuing to be tested at the LHC.

3.3 Introduction to Top Quark Physics

The existence of a third generation of quarks was first postulated in 1973 by research done by Makoto Kobayashi and Toshihide Maskawa in an effort to explain the observed CP violations in kaon decay [15]. They showed that the CP violation seen could not be explained with just four flavours of quarks, but only with six flavours and that the Standard Model could accommodate such a model.

With the discovery of the Tau lepton at SLAC [24] confirming a third generation of leptons in the mid 1970's the search for the two members of the third generation of quarks began. The 5th quark, the bottom, was discovered in 1977 at Fermilab [25] but discovery of the 6th and final quark took a lot longer than many at the time believed.

It was finally discovered in 1995 [26, 27], roughly two decades after the discovery of the bottom quark and was named the top quark. The eventual discovery of the top quark caused a wave of interest as its mass was considerably heavier than any of the other quarks. With the top's mass being so large it has opened up a new area of research into investigating the cause of the higher mass and the overall effect it plays on its own properties and that of other particles, such as the theorized Higgs boson.

Investigations into the top quark will form a major element of the research that will take place at the LHC, not only since further understanding of this fermion is desired but also because top quark events will form one of the major backgrounds for many different studies.

Current data on the top quark comes from only two sources: LEP, and the Tevatron. Although the top quark was never directly seen at LEP, data was gathered by the DELPHI, ALEPH and OPAL experiments via indirect higher order processes that gave an indirect measurement on the top quark mass that was later confirmed at the Tevatron. The only experiments directly producing top quarks before the LHC are CDF and DØ at the Tevatron.

Since the discovery of the top quark, the experiments at the Tevatron have continued to collect data to the present day and with refinements in analysis techniques and accumulated data the error on the top quark mass is now only ±1.1 GeV with the measured mass of $173.3 \pm 0.6(stat) \pm 0.9(sys)$ GeV [28].

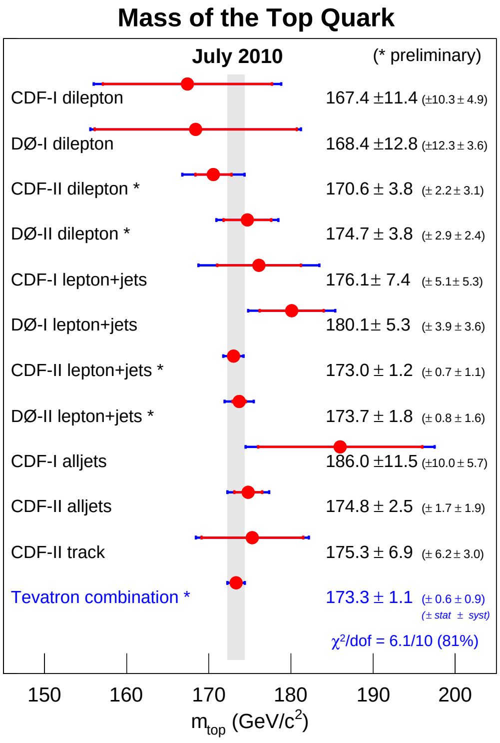

Figure 3.3: Combined results of CDF and DØ on the mass of the top quark [28].

With the initial design of the LHC stated to achieve a centre-of-mass energy of 14 TeV and luminosity of $10^{34}\text{cm}^{-2}\text{s}^{-1}$ the LHC could, in one day, achieve the equivalent of ten years of data collection at the Tevatron. However, with the stated problems with the LHC the current running is planned to only have collisions at 7 TeV and a peak luminosity of no more than $10^{33}\text{cm}^{-2}\text{s}^{-1}$.

Fortunately even with these reductions in beam energy and luminosity the LHC will still produce top quarks in quantities far in excess of those seen at the Tevatron.

3.3.1 Top Quark Production

By far the largest production of top quarks at the LHC will come from $t\bar{t}$ events. The dominant $t\bar{t}$ production process at the LHC is shown in Figure 3.4 with the highest contributions from gluon-initiated processes. The total cross section for $t\bar{t}$ at the LHC is presently calculated as $164.8^{+11.4}_{-15.7}$ pb [29] for 7 TeV collisions at near-NNLO precision.

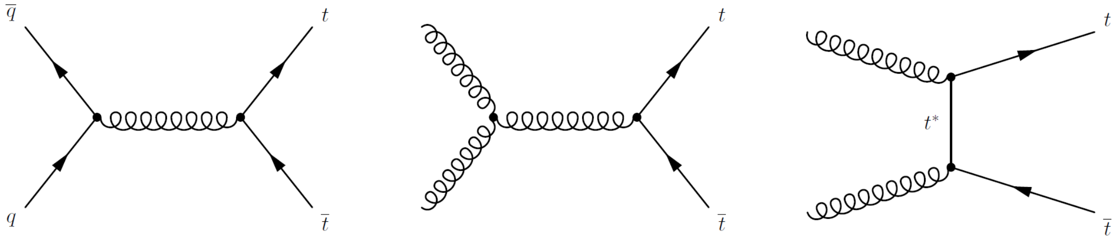

Figure 3.4: Leading order $t\bar{t}$ production.

Single top-quark production will also occur at the LHC and contributes a large fraction to the overall top quark production. The leading order diagrams for this process are shown in Figure 3.5 and the LHC will offer the first real chance to study this channel with large statistics. The cross section for single top quark is approximately half of that for $t\bar{t}$.

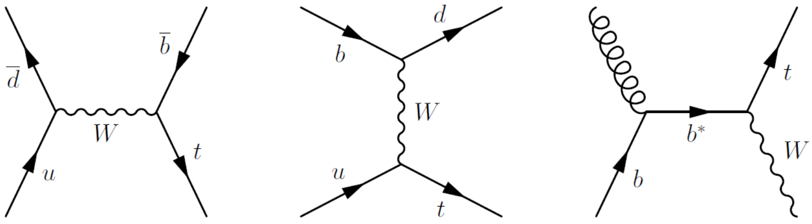

Figure 3.5: Single top-quark production diagrams.

The $t\bar{t}$ events are likely to be the primary source of data when measuring the top-quark properties at the LHC.

3.3.2 Top Quark Decay

With a mass of ~ 175 GeV and a lifetime of $\sim 5 \cdot 10^{-25}$ seconds the decay of the top quark is interesting by itself. With such a short lifetime the top quark decays before hadronization and will also not form any bound states, which would require about 10^{-24} seconds.

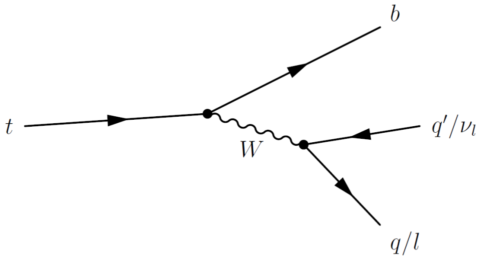

Figure 3.6: Feynman diagram of top quark decay.

According to the SM the top quark decays almost exclusively to a W boson and a b quark as shown in Figure 3.6. In fact about 99.8% top quarks will decay through $t \rightarrow W + b$, while the remaining 0.2% includes Cabbibo suppressed $t \rightarrow W + s$. Figure 3.7 shows the relative percentages for each different decay of top quark pairs. The decay modes of the W boson are used as a way to classify the events, whereby it is possible to have “all-hadronic”, “dileptonic” or “lepton + jets”.

The work presented in this thesis will focus on the “lepton + jets” channel shown in Figure 3.8.

The “lepton + jets” channel is of interest for a few reasons: requiring that one of the W bosons decays leptonically to an e or μ, substantially reduces the amount of background without reducing significantly the branching ratio, which is $\sim 30\%$ of all $t\bar{t}$ events. One of the important tools for selecting clean top quark samples, particularly in the single lepton plus jets channel, is the ability to identify b-quarks. One of the main sources of background for $t\bar{t}$ decay to lepton plus jets are the W + multi-jet processes. Requiring a tagged b-quark jet in an event can substantially reduce this source.

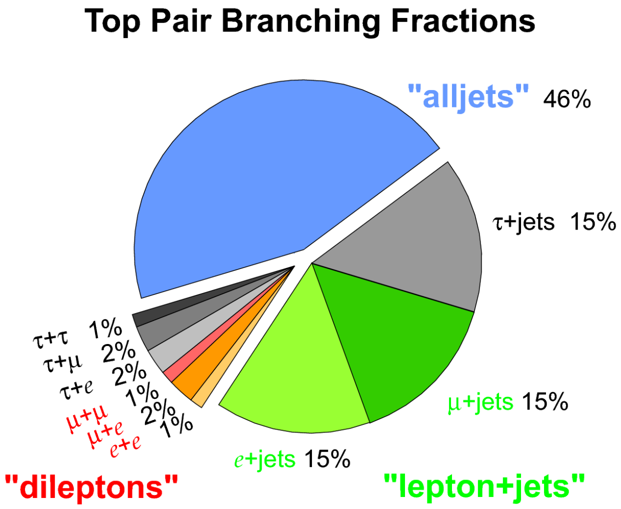

Figure 3.7: Proportion of different $t\bar{t}$ decay modes.

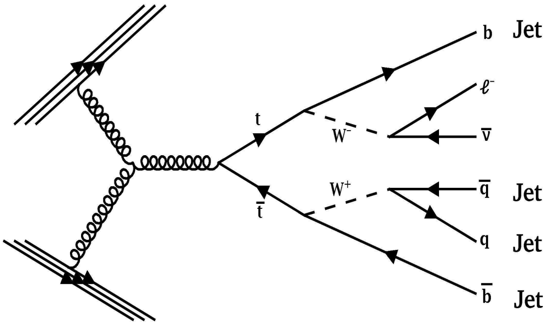

Figure 3.8: Lepton + Jets decay mode of $t\bar{t}$.

Jets originating from the decay of a b-quark can be identified using two different techniques: vertex or soft lepton tagging. For this analysis we will be using soft lepton tagging which will be further discussed in Section 6.2. There are several properties of the b quark that can be used to identify them from jets which contain only lighter quarks.

- The fragmentation of the b quark is hard and the b-hadron retains about 70% of the original b quark momentum;
- The semi-leptonic decays of the b-hadrons can be used by tagging the lepton in the jet, soft lepton tagging;
- Hadrons containing a b quark have a relatively long lifetime, of the order of 1.5 ps. A b-hadron in a jet with a $p_T = 50$ GeV will therefore have a significant flight path length $< l >= \beta\gamma c\tau$, travelling on average about 3 mm in the transverse plane before decaying. Such displaced vertices can be identified by measuring the impact parameters of the tracks from the b-hadron decay products;
- The mass of b-hadrons is relatively high ($>$ 5 GeV). Thus, their decay products may have a large transverse momentum with respect to the jet axis and the opening angle of the decay products is large enough to allow for separation.

Chapter 4

Detector Simulation and Event Reconstruction

4.1 Introduction

Before any measurements are taken using ATLAS on the particle collisions from the LHC it is important to investigate the various different models of particle interactions that exist.

Moreover with a totally new detector it is important to understand as best we can the predicted detector response via the simulation of a range of different particle interactions within it.

In this chapter, the main generators used in top-quark physics studies and the simulation and reconstruction of Monte Carlo (MC) events and data within ATLAS will be briefly described.

4.2 Monte Carlo Generators

Before any data was taken with ATLAS and like numerous experiments before it, a vast programme of simulation was undertaken to try and understand the performance of the detector in regards to important physical processes. This was done using Monte Carlo generators. These are programmes which use theoretical or empirical models built from data collected by previous experiments as a basis for simulating potential processes.

Monte Carlo generators follow a paradigm that divides the collision event into stages shown in Figure 4.1. This is stated in [30] as the following:

- Hard Scattering - This is the core of the interaction between two hadrons. It is usually the theoretically best understood and experimentally interesting part. The scattering of the two partons within the hadron is governed by the parton distribution function $f(x_i, Q_i^2)(PDF)$ that gives the probability to resolve a parton i with longitudinal momentum fraction x_i inside a hadron by a momentum transfer of Q_i^2 between the incoming particle and the resolved parton. This can be calculated to leading order (LO) and next to leading order (NLO) relatively easily.

- QCD-Bremsstrahlung - This is also commonly known as the parton shower and consists of gluons emitted by accelerated colour partons. This leads to a cascade of partons which are modelled by perturbation theory and has a low energy cut of ≈ 1 GeV where perturbation theory becomes unreliable.

- Hadronisation - This step confines coloured partons into uncoloured hadrons. This is an enormously complex part of the process and currently there are two phenomenological models used to predict this, the string model [31] which is used in the PYTHIA [32] and Sherpa[33] generators and the cluster model which is used in the HERWIG [34] generator.

- QED-Bremsstrahlung - Photons are emitted from charged accelerated particles in a mathematically similar fashion to that of QCD-Bremsstrahlung, except in this case limited to the QED sector.

- Underlying Event - Refers to the beam remnants and multiple particle interactions. As hadrons are not fundamental in nature, there can be an initial hard scatter between two partons, leaving a background of particles from the fragmentation of the remaining object.

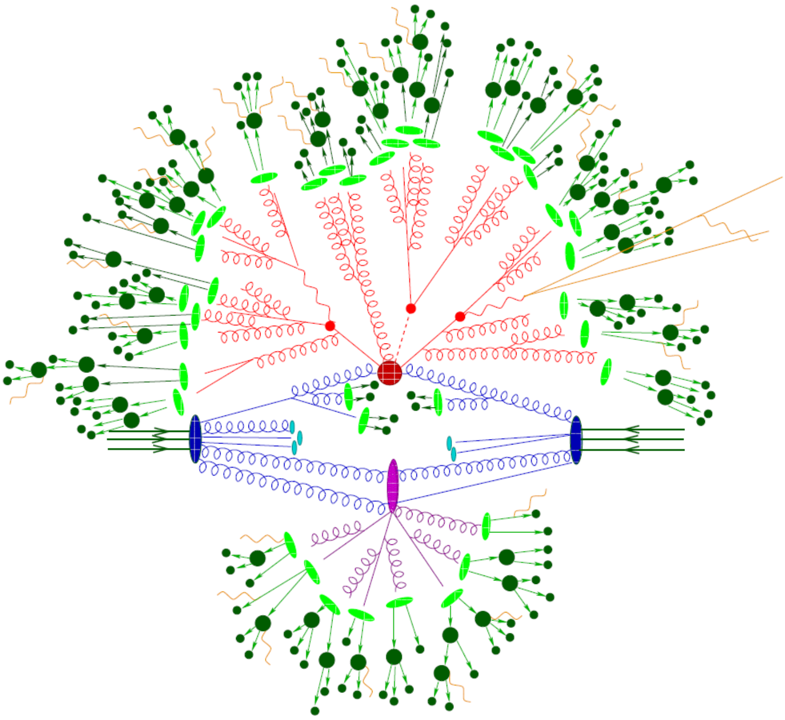

Figure 4.1: Representation of a proton-proton collision event simulated by Monte Carlo. The incoming protons are drawn in dark blue. The hard scattering process is shown at the dark red circle. QCD-Bremsstrahlung is drawn for the initial state (blue) and final state (red). The underlying event, in this case multiple parton interactions, is shown in purple. The hadronization of partons is depicted by light green ellipses. The decay of hadrons is represented by dark green. QED-Bremsstrahlung is shown in yellow. [35].

There exist many different Monte Carlo generators and they can each take a slightly different approach in modelling certain aspects of a particle interaction. Table 4.1 gives a brief overview of the main properties of the three Monte Carlo generators that I will use throughout my analysis. Details studies on the differences between the generators can be found in [36].

Generator	Matrix Element	Parton Shower[1]	Hadronization	Underlying Event
HERWIG	LO	angular ordered	cluster model	Jimmy [37]
MC@NLO[38]	NLO	p_T ordered	via HERWIG	via HERWIG
PYTHIA	LO	p_T ordered	string model	multiple interactions, beam remnants
Alpgen[39]	LO	p_T ordered	via HERWIG	via HERWIG

Table 4.1: Main properties of the Monte Carlo generators used within this analysis.

The default generator for the $t\bar{t}$ production within ATLAS is MC@NLO [38, 36]. Due to the various different approaches used in each of the generators there is often slight discrepancies between them, therefore during first collisions there will be a lot of investigation into well understood regions of data. These control regions will enable the extraction of scale factors and distributions that are often poorly predicted by MC simulations, due to either theoretical uncertainty or detector simulation limitations.

4.3 The ATLAS Software

The development of the software tools used in the ATLAS collaboration have been under way since 1990 and have a crucial role to play in an experiment of this size and complexity. It is based on object-oriented (OO) design with C++ and is called under its framework name, Athena, which was fully released in 2000.

The Athena framework is an enhanced version of the Gaudi framework that was originally used by the LHCb experiment, but the development has now become a combined ATLAS-LHCb project. The Athena framework handles all levels of processing of ATLAS data, from the initial high-level trigger, through event simulation,

---

[1] Order in which the Monte Carlo shower algorithm evolves the parton.

reconstruction and analysis. Keeping the same framework throughout the "Full Chain" of data reconstruction allows for a common set of tools to be made with the knowledge that all geometry and conditions data will universal across applications.

4.3.1 Full Detector Simulation and Reconstruction

Producing a complete description of the ATLAS detector is a major challenge as it involves the modelling of a large number of different physics processes within the various detector elements of ATLAS. There has been considerable testing of detector components in test beam and the GEANT4 [40, 41] simulation toolkit was chosen as it provided the required agreement [42].

The initial test-beam data showed very good agreement, of the order 1% or better in most cases [43], in particular the performance of electromagnetic calorimetry is well understood. However with the recent full LHC in operation an updated comparison has shown room for improvement in hadronic shower modelling [42].

The complexity of the ATLAS detector and of the events that are simulated to occur within it, requires a lot of computational resources and this has been in operation successfully for a number of years on the Grid. Figure 4.2 shows how the simulated raw data, Raw Data Object (RDO), is produced from the generated Monte Carlo events.

During simulation these events will create hits within the GEANT detector geometry and may produce secondary particles which can also be reconstructed as separate objects.

4.3.2 Data Formats

The ATLAS detector is expected to produce approximately 3 PB of raw data per year [43]. This is quite a staggering amount of data that has required the building of the Grid for the distribution and storage across multiple sites around the world. The

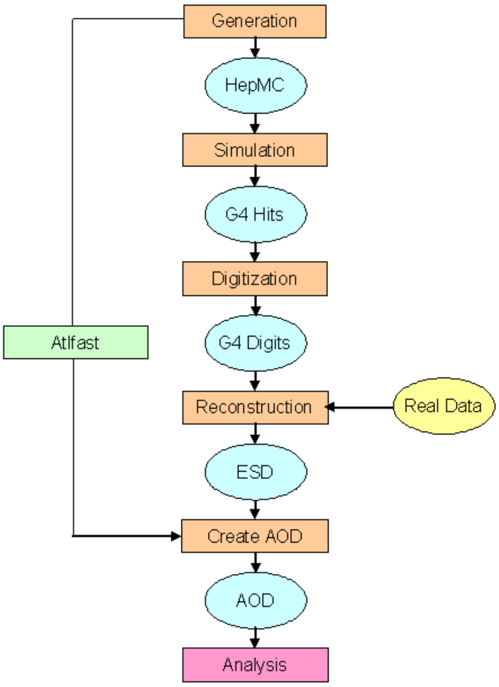

Figure 4.2: Schematic diagram of “full chain” Monte Carlo production.

computation demands of such large amounts of data in physics analysis have also dictated that the data not be stored in one location. Depending on the requirement there are various stages of data reconstruction:

- Byte-stream Data - This is a persistent presentation of the event data flowing from the high level trigger.
- Raw Data Object (RDO) - A C++ object representation of the byte-stream data. RDO files produced from simulation are designed to mirror precisely the RDO's from data.
- Event Summary Data (ESD) - Contains the full output of the detector reconstruction produced from raw data. Holds all the required information for particle identification, track reconstruction, jet calibration etc.
- Analysis Object Data (AOD) - A summary of the ESD, containing sufficient information for common object analysis, such as tracks, calorimeter clusters, jets,

photons, electrons and muons.

- Derived Physics Data (DPD) - A user or physics group derived format from AOD's that contains objects or properties relevant to a particular analysis.

From the typical user point of view the data format you are expected to run your analysis on is either the AOD or a centrally produced DPD from a physics group.

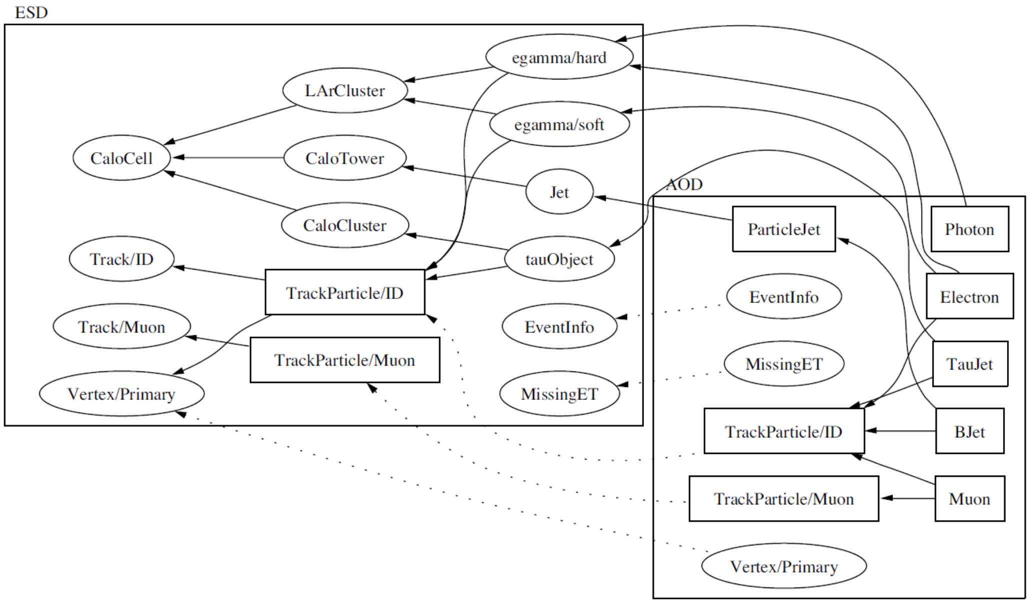

Figure 4.3: A simplified view of the contents of the ESD and AOD. The solid lines indicate objects that allow "back navigation" to a more generic object. The dotted lines indicate objects that are duplicated between the ESD and AOD. [43]

4.4 Object Reconstruction

The aim of reconstruction is to derive from the stored raw data a series of particle and objects necessary for physics analysis, such as: photons, electrons, muons, jets, missing transverse energy. The full detector information is used and combined to give optimal information on the four-momentum of an object for use in an analysis.

A typical reconstruction algorithm will take information from one or more collections as an input (such as the inner detector tracking and muon spectrometer) and outputs one collection of reconstructed objects. The finer details of some of the more complex reconstruction algorithms is beyond the scope of this thesis but a full account can be found in [44].

4.4.1 Tracking

A seeded track finding tool takes measurements from the SCT and pixel sub-detectors and extrapolates them out towards the straw tracker [45]. Firstly track seeds are formed from a combination of space-points in the three pixel layers and the first SCT layer. These seeds are then extended throughout the SCT to form track candidates. Next, these candidates are fitted and “outlier” clusters are removed, ambiguities in the cluster-to-track association are resolved, and fake tracks rejected. This is achieved by applying quality cuts. For example, a cut is made on the number of associated clusters, with explicit limits set on the number of clusters shared between several tracks and the number of holes per track (a hole is defined as a silicon sensor crossed by a track without generating any associated cluster). Track candidates are extended out to the TRT with a global refit performed when necessary.

A complementary track-finding strategy, called back-tracking[45], searches for unused track segments in the TRT. The back-tracking procedure finds unused segments in the TRT and the extends them into the SCT and pixel detectors in an effort to recover tracks whose seed was not found and to improve the tracking efficiency for secondary tracks from conversions or decays of long-lived particles.

4.4.2 Electron/Photon Reconstruction

The seed for an electron or photon starts with a cluster of electromagnetic energy in the calorimeter. The separation of electron and photon candidates is achieved by requiring the electrons to have an associated track in the inner detector but no associated conversion into an electron/position pair. Only EM clusters that have been matched to an inner detector track of greater than 5 GeV and that point to within $\Delta\eta < 0.05$ and $\Delta\phi < 0.1$ of the cluster form electron candidates. Similarly for photons we require that there is no matched track to the EM energy deposit, but there can be a matched reconstructed conversion.

The main background for electron/photon candidates comes from hadronic jets, most of which are composed of neutral pions that decay into pairs of photons. In the case of photons it is quite easy for a hadronic jet to fake a photon, especially when they contain single or multiple neutral hadrons that decay to produce a high fraction of photons from decays such as $\pi^0 \to \gamma\gamma$. To aid in rejecting hadronic jets from real electrons and photons a series of calorimeter and inner detector information is stored regarding numerous variables, such as the lateral and longitudinal EM shower shapes. The shower shape allows for the distinction between an electromagnetic shower, that typically has a very narrow deposit of energy, and that of an hadronic jet which tends to spread its energy over a wider area.

Specifically during this analysis I will be using two particular ATLAS definitions for electron identification, the "Egamma author" = 1 or 3 and the "IsEM" = medium bit mask. The author definition refers to only electron candidates that have been reconstructed using seeds in the calorimeter and not candidates based solely on track information.

The IsEM definition provides three reference sets of cuts based on calorimeter, tracker and combined calorimeter/tracker information. The reference set of cuts are defined with increasing background rejection power: Loose, Medium and Tight. The Loose definition uses shower shape variables of the second calorimeter layer and hadronic leakage variables in its selection[1]. The Medium definition adds on to the loose selection, first layer calorimeter cuts, track quality requirements and track-cluster matching in $|\eta|$. The Tight definition adds further selection information on cluster energy E and

---

[1] The hadronic leakage is defined as the ratio of the transverse energy reconstructed in the first compartment of the hadronic calorimeter in a window $\Delta\eta \times \Delta\phi = 0.2 \times 0.2$ to the transverse energy reconstructed in the electromagnetic calorimeter.

momentum p ratio, E/p, b-layer hit requirements and the particle identification of the TRT [46].

4.4.3 Muon Reconstruction

Atlas has a variety of strategies for identifying and reconstructing muons:

- Standalone - This approach reconstructs muons by finding tracks in the muon spectrometer and then extrapolates these to the beam line.
- Combined - Uses standalone muons and matches them to nearby inner detector tracks and then combines the measurements of from the muon spectrometer and inner detector.
- Tagged - Inner detector tracks are extrapolated to the muon spectrometer and matched to any nearby hits if they exist.

Each strategy for muon reconstruction within Atlas includes two algorithms:

- STACO [47], which uses the MuonBoy algorithm [47].
- MuID [48], which uses the MOORE algorithm [49].

Throughout this analysis only the STACO algorithm is used, as required by the top-quark working group. Both algorithms operate in similar fashion and start by identifying muon spectrometer tracks and extrapolate them back to the inner detector, where a search is done to match them to tracks within the inner detector.

Of particular interest in this analysis is the "combined" muon: this is a muon candidate that has both a muon spectrometer track and a matched inner detector track. With a combined muon it is possible to use the χ^2_{match}, defined as the difference between the outer and inner track vectors weighted by their combined covariance matrix [45]:

$$\chi^2_{match} = (\overrightarrow{T}_{MS} - \overrightarrow{T}_{ID})^T (\hat{C}_{ID} + \hat{C}_{MS})^{-1} (\overrightarrow{T}_{MS} - \overrightarrow{T}_{ID}) \tag{4.1}$$

Where $\overrightarrow{T}$ is a vector of five track parameters expressed at the point of closest approach to the beam line and $\hat{C}$ is its covariance matrix.

Muons with a p_T between 3 and 6 GeV will loose a large fraction or most of their energy in the calorimeters and may not cross the full muon spectrometer, this can cause problems with starting the reconstruction there. In this case, muon tracks are first found within the inner detector and extrapolated to hit segments in the spectrometer.

4.4.4 Hadronic Jet Reconstruction

The calorimeter system is the main sub system used in the reconstruction of hadronic jets within ATLAS. As the ATLAS calorimeter has about 200,000 cells of different size and geometry it is necessary to combine all the cell information in a way that is practical as an input for a jet finder algorithm. At present this is done in two possible ways, either as CaloTowers or CaloClusters objects [43]. The CaloTower objects represent a tower of cells on a fixed grid in pseudo-rapidity and azimuth with a typical bin size of $\Delta\eta \times \Delta\phi = 0.1 \times 0.1$. The CaloCluster objects represent groups of cells with correlated signals to the neighbouring cells. Both CaloCluster and CaloTower carry the required four-momentum information required for the input into different jet algorithms.

There are many different jet reconstruction algorithms available for use, the details of which are beyond the scope of this analysis. The top-quark group within ATLAS has an object recommendation [50] that allows for consistent comparison between different top analyses. The recommended jet reconstruction algorithm is the the anti-k_T algorithm [51, 52], based on topological clusters, with a cone size of $D = 0.4$, where $D = \sqrt{\Delta\eta^2 + \Delta\phi^2}$, with $\Delta\phi$ and $\Delta\eta$ the separation in η and ϕ for the cluster deposits used in the jet reconstruction.

4.4.5 Calorimetric Isolation Variables

The amount of energy surrounding a lepton is often used to discriminate lepton candidates from W or Z decays from objects faking their signature; isolated electrons and muons will deposit their energy in a narrow calorimeter cluster. In the case of non-isolated electrons, muons and jets, the candidate is accompanied by further particles, which deposit additional energy in the vicinity. Throughout this analysis I will make use of the calorimetric isolation of both electrons and muons. The way in which the isolation energy is calculated for electrons and muons differs, although both are calorimetric variables.

In the case of electrons, the calorimetric isolation is computed from the amount of energy that is deposited in a cone of radius R_0 around the electron candidate, where the 5×7 ($\eta \times \phi$) cells of the electron cluster are removed [53]:

$$E_T^{cone}(R_0) = \sum_{\substack{\text{cells} \\ \Delta R < R_0}} E_T(\text{cell}) - E_T(5 \times 7 \text{ cells})[\text{GeV}] \tag{4.2}$$

A range of standard cone sizes are used in ATLAS, such as $R_0 \epsilon \{0.2, 0.3, 0.4\}$. The corresponding isolation variables named $E_T^{cone}(0.2)$, $E_T^{cone}(0.3)$, $E_T^{cone}(0.4)$ respectively are stored in the AOD. Graphically, E_T^{cone} for e/γ objects is represented in Figure 4.4

In the muon system the difference between the energies in two cones is used to compute the E_T^{cone} around a muon candidate [45]. An inner cone of radius 0.05 is used to define the E_T^{core} of the muon with varying outer cone sizes such as 0.2, 0.3 and 0.4. Visually E_T^{cone} is shown in Figure 4.5 and is defined mathematically as:

$$E_T^{cone}(R_0) = \sum_{\substack{\text{cells} \\ \Delta R < R_0}} E_T(\text{cell}) - \sum_{\substack{\text{cells} \\ R = 0.05}} E_T^{core}[\text{GeV}] \tag{4.3}$$

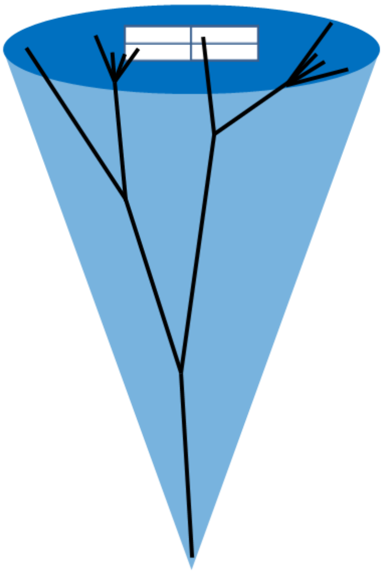

Figure 4.4: Graphical representation of E_T^{cone} for e/γ objects.

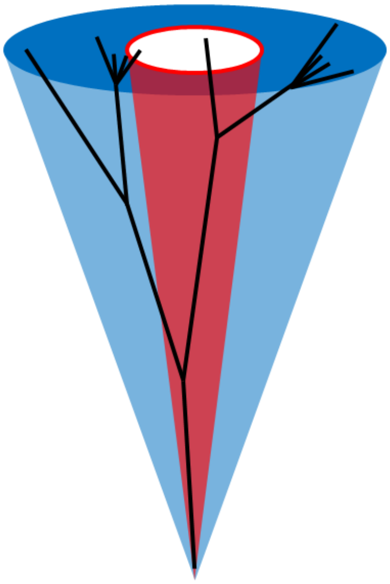

Figure 4.5: Graphical representation of E_T^{cone} for Muon objects.

Chapter 5

Electrons in $Z \rightarrow ee$ and $t\bar{t}$ decays

5.1 Introduction

The tagging of events where the top quark decays via the emission of a W boson is heavily dependent on the correct identification of the high-p_T lepton from the W. This is also the case when looking into Z decays where both products are high-p_T leptons. One way to distinguish the electrons from the decay of W and Z bosons from those present in light and heavy-flavour decays is to use a discriminating variable that takes into account the jet activity surrounding the electron. Electrons that decay from the W and Z will in general be more isolated than those present in light and heavy-flavour jets.

Prior to this analysis the recommendation by the top-quark working group within ATLAS was to use a quantity called E_T^{cone20} as a cut on isolation energy. E_T^{cone20} is the total transverse energy E_T in a cone of opening $\Delta R = 0.2$ around an EM cluster centroid, minus the EM cluster E_T. The requirement was $E_T^{cone20} < 6$ GeV, however we found upon initial examination of this cut that the efficiency drops off as a function of electron p_T as there is no consideration of the increased bremsstrahlung and electromagnetic shower at high-p_T.

This analysis was instigated to try and find a cut that would maintain efficiency at high-p_T, whilst also ensuring that background rejection of QCD jets faking electron signatures is not altered, if not improved upon. Maintaining efficiency at high-p_T is important for detecting boosted top quark events and to study differential cross sections which may be sensitive to new physics with top-like signatures, as well as being important for searches into SUSY with W and Z-like signatures.

The analysis presented in this chapter aims to highlight the deficiency in a constant isolation cut and propose an alternative choice of isolation requirement that maintains efficiency across a large p_T range whilst improving background rejection of QCD jets faking isolated electrons.

5.2 Event Selection and Monte Carlo samples

The AOD simulated samples were produced with a centre of mass energy of 10 TeV and with ATLAS Athena release version 14. The $t\bar{t}$ sample was used alongside the $Z \rightarrow e^+e^-$ sample as a way to gauge whether increased event noise in $t\bar{t}$, (for example nearby hadronic jets, increased calorimeter activity) events would have an effect when optimising the alternative isolation requirement. Care was taken to ensure both samples used the same ATLAS reconstruction and simulation version. The MC@NLO $t\bar{t}$ sample was semi-leptonic, in that it had one top quark forced to decay via $W + b \rightarrow l\nu b$ decay. Table 5.1 provides a summary of the cross sections, number of events and equivalent luminosity.

Process	Generator	σ_{eff} [pb]	N_{EV}	L [pb^{-1}]
$t\bar{t}$	MC@NLO	$202.86 \cdot 1.07$	1106024	5095.47 (NNLO)
$Z \rightarrow e^+e^-$	Pythia	$1143.96 \cdot 0.96$	1500000	1365.87 (LO)

Table 5.1: Cross section (times the filter efficiency), number of events and integrated luminosity for the two samples used in this study. For the $t\bar{t}$ sample the number of events is the sum of the weights.

Electrons were considered to have come from the decay of a W or Z if they passed the following selection criteria:

- $p_T > 20$ GeV/c
- $|\eta| \leq 2.47$ except barrel/end-caps "crack" region $1.37 < |\eta| < 1.52$
- "Egamma author" = 1 or 3
- "IsEM" = mediumNoIso

Information regarding the "Egamma author" and "IsEM" definitions can be found in Section 4.4.2. Note the use of "IsEM" = mediumNoIso is to remove an upper isolation cone requirement that was present in version 14 of the ATLAS software, this requirement was removed in version 15, the "mediumNoIso" definition is otherwise identical to "medium" definition in version 15. Other event selection criteria is as listed in [54].

Truth information from Monte Carlo simulation is used in this analysis to ensure that the electron candidates used in this analysis were from real W-electrons reconstructed within the detector. This was achieved by first matching the reconstructed electron to a truth electron from the Monte Carlo information by requiring that the angular separation between reconstructed electron and truth electron, was $\Delta R < 0.01$, and then requiring that this electron has either a W or Z boson as its parent.

5.3 Electron E_T^{cone20} distributions

Figure 5.1 shows the distribution of isolation energy measured as E_T^{cone20} for an electron from W decay (in top quark events) and $Z \rightarrow e^+e^-$ decay. Using the standard reconstruction and selection cuts to find potential electrons from W decay in $t\bar{t}$ events and electrons from Z decay, Figures 5.1a, 5.1c show the profile plots of the mean and RMS of the E_T^{cone20} distributions as a function of E_T. Using the same candidate electrons but adding an additional requirement that the electrons are truth matched to either a W, in $t\bar{t}$ events or from a Z decay, produces Figures 5.1b, 5.1d. Matching to truth is done by requiring that the parent particle in the decay chain matches a W or Z boson.

What can be clearly seen in the figures is that there is an increase in the electromagnetic energy surrounding the electron with higher E_T, simply as a result of increased electromagnetic shower size and bremsstrahlung. Similar behaviour is seen in both $t\bar{t}$ and Z events in regards to the mean value of E_T^{cone20} for isolated electrons. The RMS for these isolated electrons does show a difference, with the electrons from the $t\bar{t}$ sample having a larger RMS. This is likely caused by the different complexity of the events: $t\bar{t}$ events will in general have more jets in the event than $Z \to e^+e^-$ events and we have not included a cut on the minimum distance from a jet for W-electrons at this stage. The prior recommendation of the top-quark working group to cut at a constant $E_T^{cone20} < 6$ GeV can be seen via the dashed horizontal line in the figures. This cut can be seen to be particularly inadequate for higher energy electrons and will reduce substantially the selection efficiency for electrons with an E_T approaching or higher than about 100 GeV.

One other interesting observation that these simulations indicate is that the surrounding energy as measured by E_T^{cone20} does not tend to zero as $E_T \to 0$ GeV. The exact cause of this noise was never directly investigated, however it is known that the simulations include calorimeter noise of about 20-30 MeV per calorimeter cell, leading to about 350 MeV for a cone of $\Delta R = 0.2$ opening. It is also possible that there is an incorrect subtraction of the electrons E_T in the E_T^{cone20} definition. We believe that the dominant cause of this offset seems to be caused by calorimeter noise, Figure 5.2 indicates that the offset increases as a function of the isolation cone size. If the dominant factor was indeed an incomplete energy subtraction of the inner 2×2 cluster, changing the size of the outer isolation cone would not have an effect. We also calculated the E_T^{cone20} in regions of the calorimeter away from an isolated electron and found a value of $\approx$350 MeV being returned.

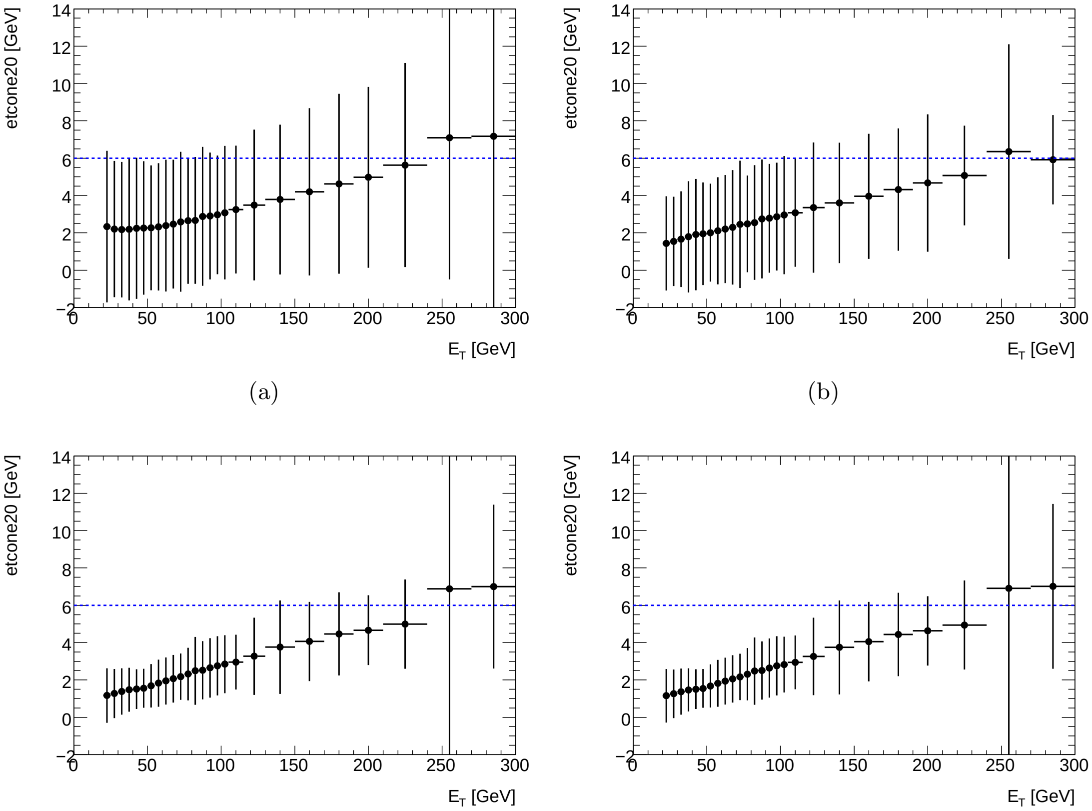

(a) (b)

(c) (d)

Figure 5.1: The mean value and RMS of the E_T^{cone20} distributions as a function of electron E_T, for: reconstructed W-electrons in top quark decay (a), reconstructed and matched to truth W-electrons in top quark decay (b), reconstructed electrons in $Z \rightarrow e^+e^-$ decay (c) and reconstructed and matched to truth electrons in $Z \rightarrow e^+e^-$ decay (d).

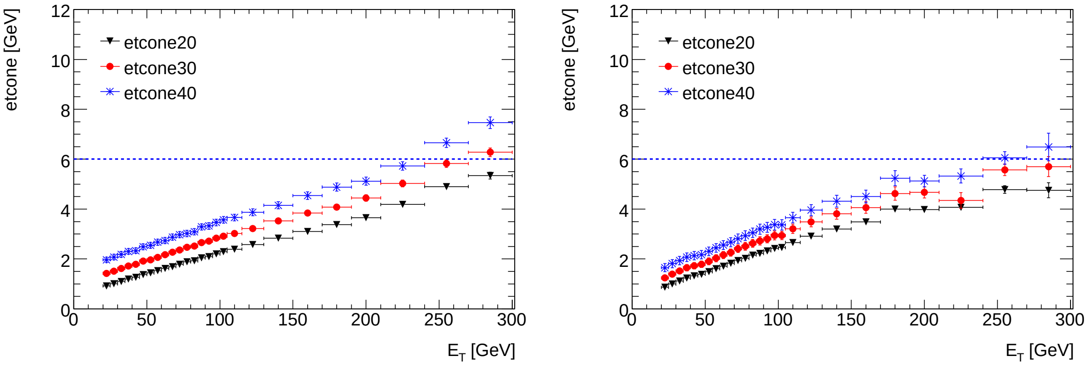

(a)

(b)

Figure 5.2: The profile of E_T^{cone20}, E_T^{cone30}, E_T^{cone40} distributions vs E_T for W-electrons from $t\bar{t}$ (a) and $Z \to e^+e^-$ (b).

An example of the E_T^{cone20} distribution for the selected, truth matched, W-electrons and $Z \to e^+e^-$ electrons can be seen in Figures 5.3a, 5.3b respectively. The two distributions show similar bodies, returning a mean value with a difference of 270 MeV, but the $t\bar{t}$ distribution has a longer tail, most likely caused by nearby jet activity to the electron.

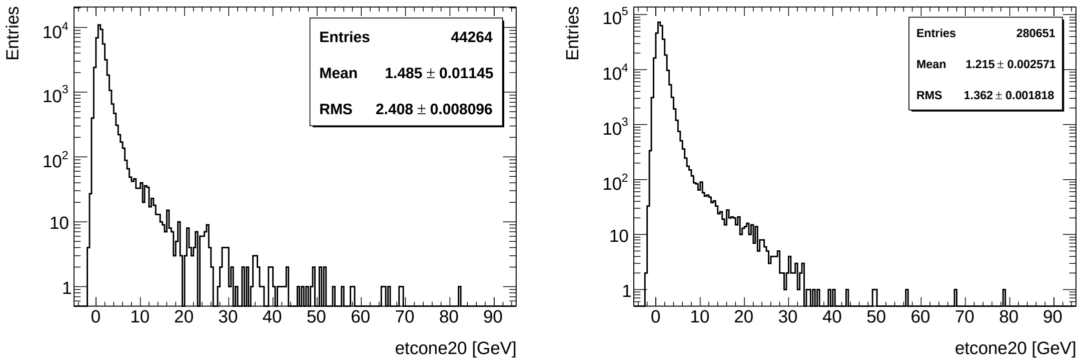

(a)

(b)

Figure 5.3: The E_T^{cone20} distributions for W-electrons from $t\bar{t}$ (a) and $Z \to e^+e^-$ (b), both truth matched and in the E_T range of 20-25 GeV.

The efficiency of the $E_T^{cone20} < 6 GeV$ cut as a function of electron E_T is shown in Figures 5.4a, 5.4b for W-electrons from top quark events and Figures 5.4c, 5.4d show the efficiency for electrons in $Z \to e^+e^-$ decays. From an initial efficiency of about 98% for $E_T = 20 - 30$ GeV the efficiency drops down to only ≈55% for electrons with an $E_T \simeq 250$ GeV. This drop in efficiency is a result of the E_T^{cone20} distributions seen earlier in Figure 5.1.

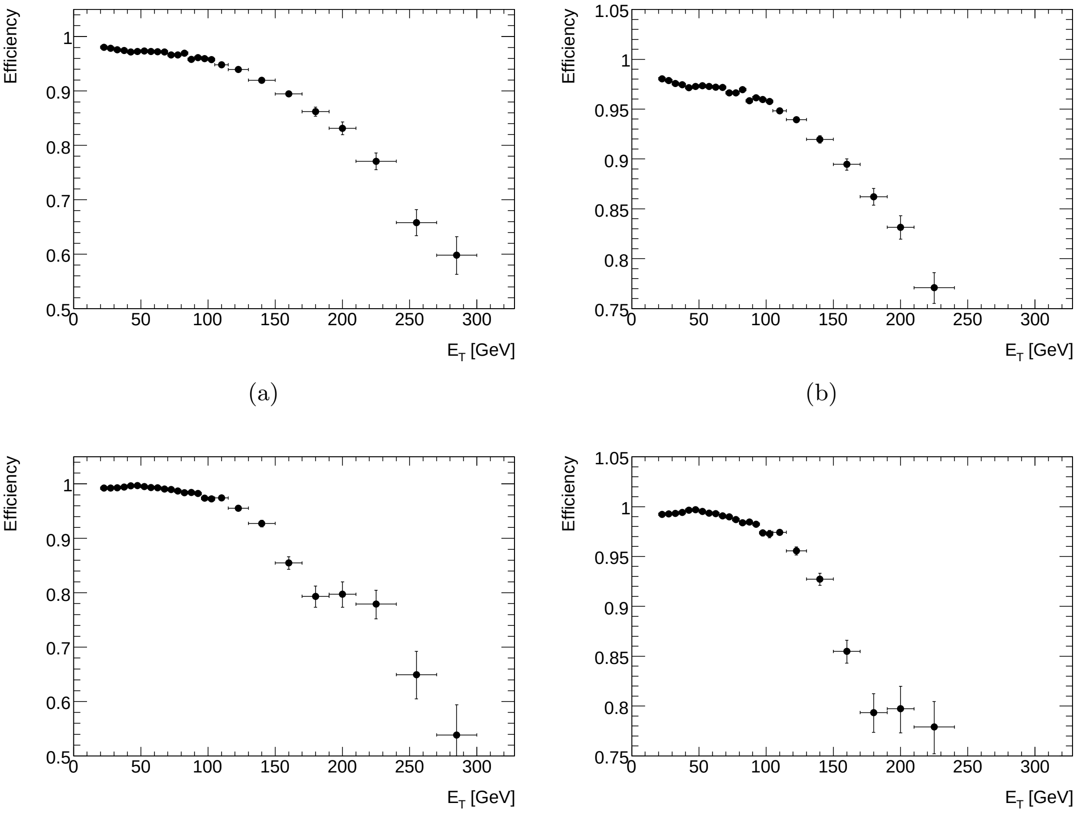

(a) (b) (c) (d)

Figure 5.4: The efficiency of the $E_T^{cone20} < 6$ GeV cut for: W-electrons matched to truth (a) and with a zoomed-in range (b), and $Z \to e^+e^-$ decay electrons matched to truth (c) and with a zoomed-in range (d).

5.4 Isolation ratio I_R

In an effort to account for the increased electromagnetic shower with higher electron E_T, dividing through by the electron E_T gives a useful quantity known as the isolation ratio, I_R:

$$I_R = \frac{E_T^{cone20}}{E_T} \tag{5.1}$$

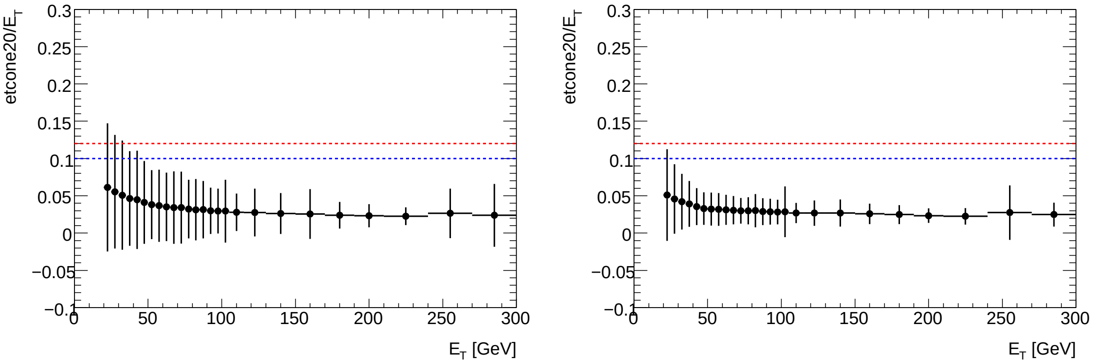

(a) (b)

Figure 5.5: The mean value and RMS of the $I_R = E_T^{cone20}/E_T$ distributions as a function of electron E_T, for: reconstructed and truth matched W-electrons in top quark decay (a) and reconstructed and truth matched electrons in $Z \to e^+e^-$ decay.

The mean value and RMS of I_R as a function of electron E_T can be seen in Figure 5.5 for both W-electrons from top quark decay and electrons in Z decay. The dependence on E_T is noticeably reduced compared to E_T^{cone20} alone and a suitably chosen requirement of I_R, such as I_R <0.1 or 0.12 would recover electrons at high E_T as well as maintaining a good efficiency in the lower E_T range. The efficiency of cutting on I_R <0.1 or 0.12 is shown in Figure 5.6 as a function of electron E_T. At low $E_T < 30$ GeV there is a small efficiency loss that could be recovered by considering calorimeter noise, as seen in the next section, however the aim to recover the efficiency at higher E_T is achieved. Yet one must also consider the E_T distribution of the W-electrons in top quark decays and the electrons in Z decays, also shown in Figure 5.6. The peak in these distributions, Figures 5.6c, 5.6d, occur in the region where the I_R based cuts are not at their most efficient, nevertheless we can calculate and compare the overall efficiency of the different isolation requirements. The total integrated efficiency over the whole energy range for the various isolation cuts is shown in Table 5.2. It indicates that cutting on I_R maintains a slightly lower overall efficiency for both $t\bar{t}$ and Z events for selected electrons $E_T > 20$ GeV whilst recovering high-E_T electrons, compared to cutting purely on $E_T^{cone20} < 6$ GeV.

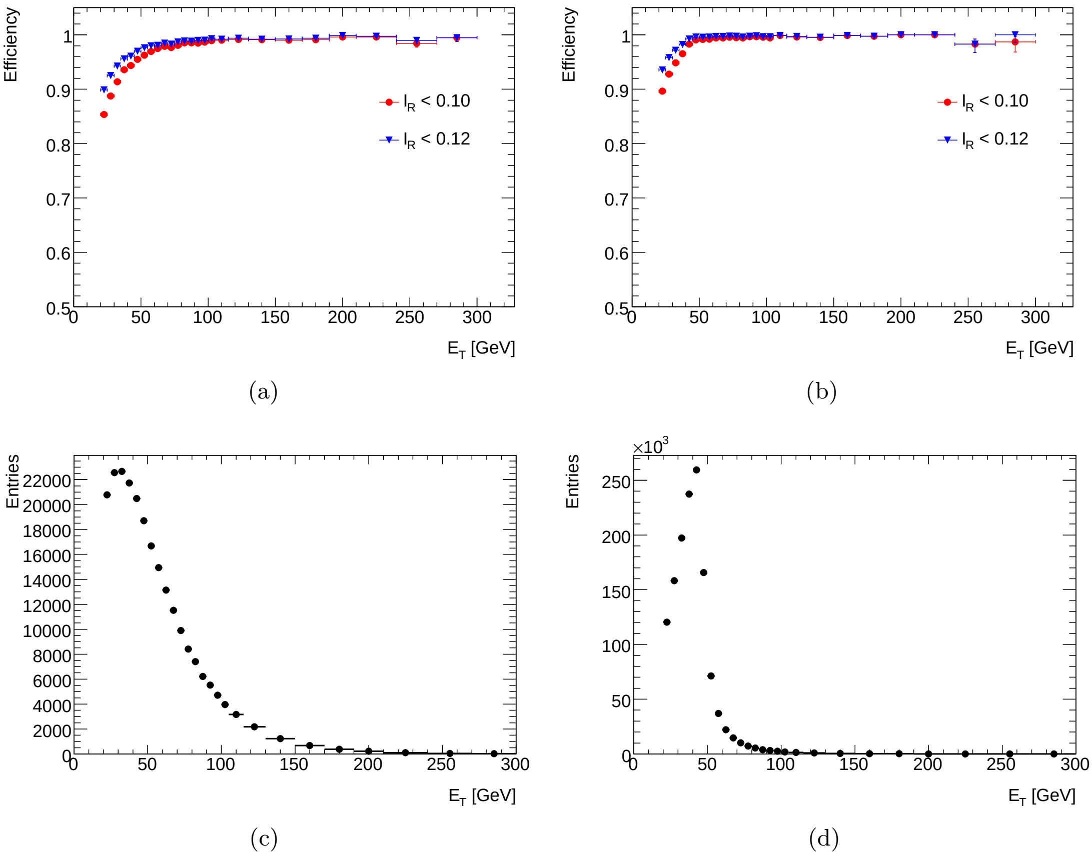

(a)

(b)

(c)

(d)

Figure 5.6: The efficiency of the $I_R < 0.1$ and $I_R < 0.12$ requirement for: W-electrons in top quark decay matched to truth (a) and $Z \rightarrow e^+e^-$ decay electrons matched to truth (b). Figures (c) and (d) show the total electron E_T distributions for $t\bar{t}$ and $Z \rightarrow e^+e^-$ events respectively.

Efficiency of different isolation cuts [%]

	$t\bar{t}$	$Z \rightarrow e^+e^-$
$E_T^{cone20} < 6$ GeV	96.6	99.4
$I_R < 0.10$ GeV	94.7	96.3
$I_R < 0.12$ GeV	96.4	97.9
$E_T^{cone20} < 4 + 0.023 \cdot E_T$ GeV	96.4	99.4

Table 5.2: The integrated efficiency of the various electron isolation cuts applied to a sample of $t\bar{t}$ and $Z \rightarrow e^+e^-$ events.

5.5 Sliding isolation cut

Figure 5.7 shows lines corresponding to the $I_R = 0.1$ and $I_R = 0.12$, overlaid onto the same plot shown in Figure 5.1a. Since we have shown that E_T^{cone20} does not approach zero as $E_T \rightarrow 0$, this implies that while a selection based on I_R recovers high-E_T electrons it is at the cost of efficiency in the 20-50 GeV region. A better solution would be to use a cut shown by the continuous line in Figure 5.7 that includes a constant term and scales as a function of electron E_T. This cut runs parallel to the mean E_T^{cone20} $t\bar{t}$ distribution at a distance of approximately two standard deviations, which is shown simply as the form:

$$E_T^{cone20} < C_1 + C_2 \cdot E_T[\text{GeV}] \tag{5.2}$$

Such a cut is designed to guarantee a constant efficiency across the entire E_T range, whilst being tighter than the existing $E_T^{cone20} < 6$ GeV cut at lower energies, such as $E_T < 100$ GeV, where it is expected QCD multi-jet production will be at its highest. For example, by using $C_1 = 4.0$ GeV and $C_2 = 0.023$ (which corresponds to the line placed 2.2σ from the mean value in $t\bar{t}$ events) one can achieve efficiency close to 100% (see Figure 5.8) over a range of E_T between 20 and 300 GeV.

The actual choice of constants depends on three main factors;

- The increase in energy surrounding an electron with the electron E_T is due to increased electromagnet shower size and this phenomena is normally well modelled in Monte Carlo simulations. Therefore C_2 can be reliably taken from simulations and its impact is measured in terms of efficiency directly from data.
- The constant C_1 term in the E_T^{cone20} plots is likely due to calorimeter noise and can therefore be set to a chosen value and measured directly on data in $Z \rightarrow e^+e^-$ data by plotting E_T^{cone20} vs E_T as shown in Figure 5.1a. However, in practice

once the cause of the constant term has been established in data, one could simply choose a value that is not too restrictive and measure the efficiency of the selection in data using the Tag and Probe method [55] on $Z \rightarrow e^+e^-$ events and adjust accordingly [56].

- Studies have also shown [56] that using a cut of the form Eq.(5.2) can significantly improve the rejection of non-isolated and fake electrons in light- and heavy-flavour jets over the rejection that is achieved using the previous standard $E_T^{cone20} < 6$ GeV requirement, since the latter is un-necessarily loose at low E_T.

5.6 E_T^{cone20} dependence on η

A check on the dependence of the value of the electrons' E_T^{cone20} as a function of electron η was performed. Figure 5.9 shows the mean and RMS of E_T^{cone20} versus η, for W-electrons from top quark decays in two ranges of E_T between 20 and 30 GeV (Figure 5.9a) and E_T between 150 and 200 GeV (Figure 5.9b). It can be seen that there is a mild dependence of E_T^{cone20} on η for the selected electrons in the forward regions, of order 1 RMS, which can easily be taken into account when choosing an isolation requirement. An interesting point to take from these plots is how the requirement of $E_T^{cone20} < 6$ GeV would have started to affect the more forward ($|\eta| \geq 1$) electrons first.

5.7 Multijet background rejection

A full study of the dijet and multijet background rejection by the isolation requirement was not undertaken at the time of this study, not least because this study was done before jet data was available. Moreover we were not interested in optimizing the electron isolation requirement, which would be dependent on specific analyses. However it was instructive to see how the jet background may populate the isolation versus E_T profile plots.

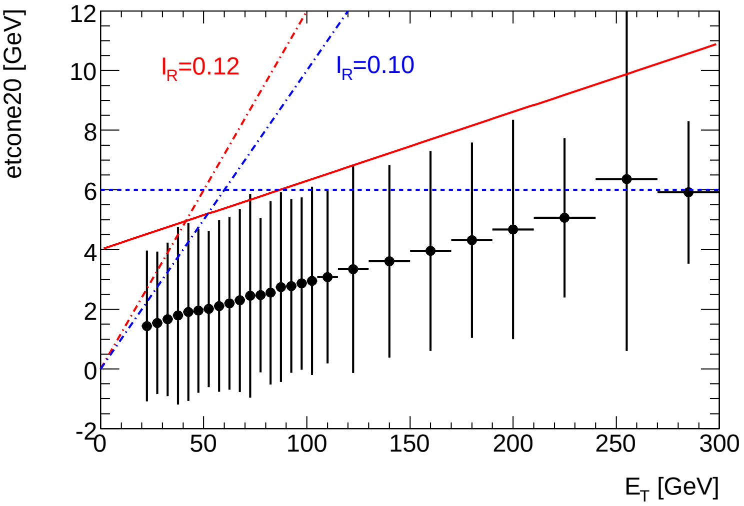

(a)

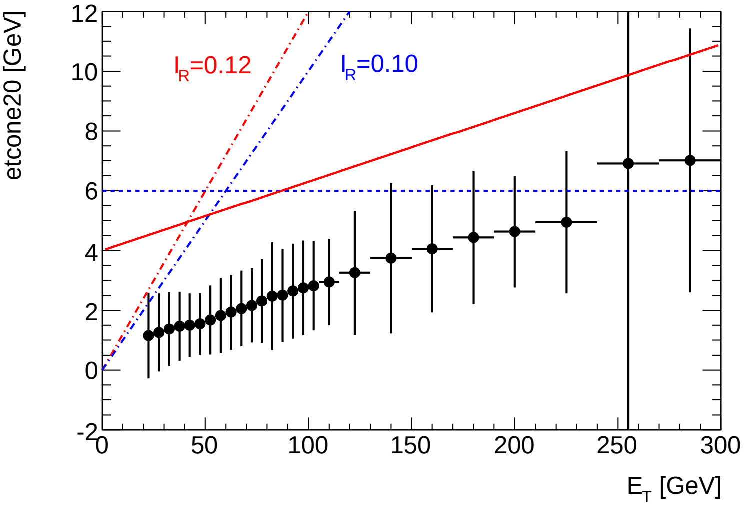

(b)

Figure 5.7: The mean value and RMS of the E_T^{cone20} distributions as a function of electron E_T for W-electrons in $t\bar{t}$ (a) and electrons in $Z \to e^+e^-$ (b), overlaid with possible selection requirements. Selections considered are $E_T^{cone20} < 6$ GeV, $E_T^{cone20}/E_T < 0.1$ and $E_T^{cone20}/E_T < 0.12$, and $E_T^{cone20} < 4.0 + 0.023 \cdot E_T$ GeV (continuous red line).

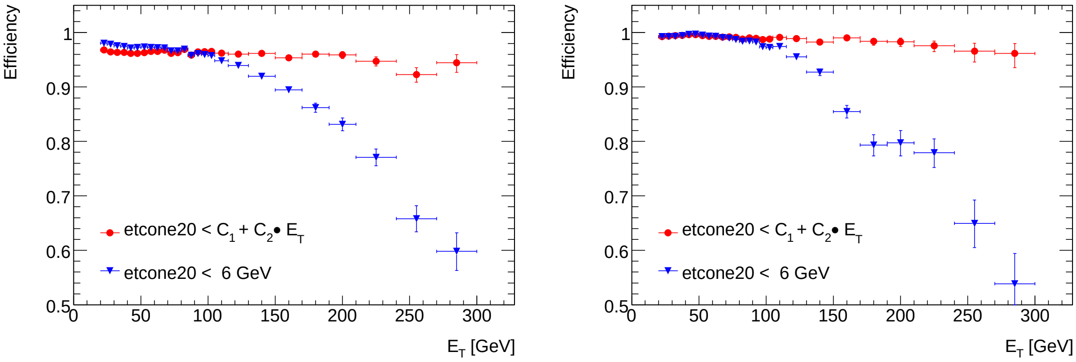

(a) (b)

Figure 5.8: The efficiency as a function of E_T with a cut of the form: $E_T^{cone20} < C_1 + C_2 \cdot E_T$, with $C_1 = 4$ GeV and $C_2 = 0.023$, compared to the standard $E_T^{cone20} < 6$ GeV requirement, for W-electrons in top quark decay (a) and $Z \to e^+e^-$ electrons (b), both matched to truth.

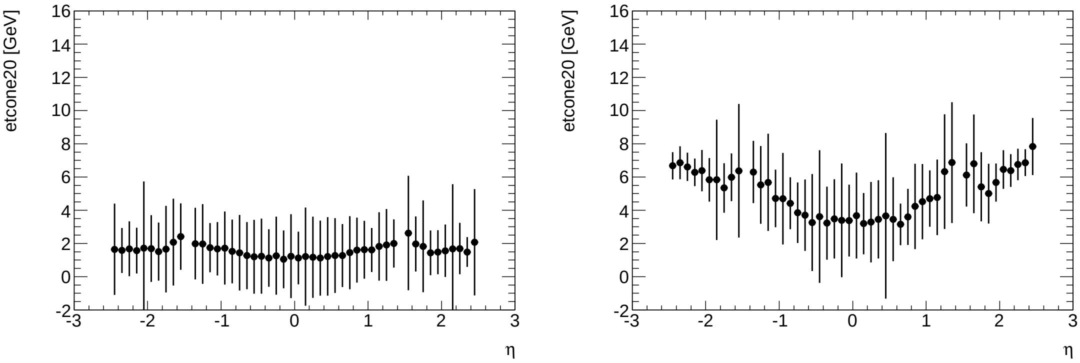

(a) (b)

Figure 5.9: The mean and RMS of E_T^{cone20} versus η for W-electrons from top quark decay matched to truth, in E_T ranges of E_T between 20 and 30 GeV (a) and E_T between 150 and 200 GeV (b).

The multijet QCD background is an important consideration when looking for electron signatures as they form the majority of fake electron detections. With the combination of charged tracks in the hadronic jets and with photon production via neutral pion decay, these two separate processes can align, a charged hadron track leading to a photon deposit, to give the signature of an electron. Figure 5.10 shows the average E_T^{cone20} distributions vs. E_T for all candidate electrons, in simulated di-jet events (with different Monte Carlo jet energy thresholds at generator level), that pass all the standard electron reconstruction cuts. The Monte Carlo sample consisted of three different Alpgen-produced di-jet samples, with the p_T cut of the jets placed at 70, 140 and 280 GeV, this was required to understand the jet E_T^{cone20} profile in di-jet events across the energy range this study was undertaken in.

The horizontal line indicates the $E_T^{cone20} < 6$ GeV requirement, while the diagonal line indicates the sliding E_T^{cone20} cut. It can be seen that the average E_T^{cone20} for the softer jets is closer to the $E_T^{cone20} < 6$ GeV requirement and a tighter cut on isolation is beneficial in this region of the phase space. At higher energies, the looser sliding E_T^{cone20} cut should not affect the rejection significantly, since the average E_T^{cone20} for hard jets is much higher than the cone energy of real isolated electrons.

Monte Carlo studies of the expected electron reconstruction and identification performance of the ATLAS detector have calculated the efficiency of detecting an electron using the "medium" definition with an isolation requirement that is optimised for different p_T and η regions. Using an isolation requirement with 95% efficiency on a $Z \rightarrow ee$ sample gives a total jet rejection, including hadron fakes and background electrons from photon conversions and Dalitz decays, of 20000 ± 350 [57]. Monte Carlo studies for the top-quark working group have shown the QCD rejection power of the sliding E_T^{cone20} cut to be better than a static track based isolation cone cut [56]. Both of these studies highlight the large cross section of QCD di-jet and multijet events and the need to use electron isolation cuts that balance efficiency against background rejection and the need to study electron fake rates in LHC data.

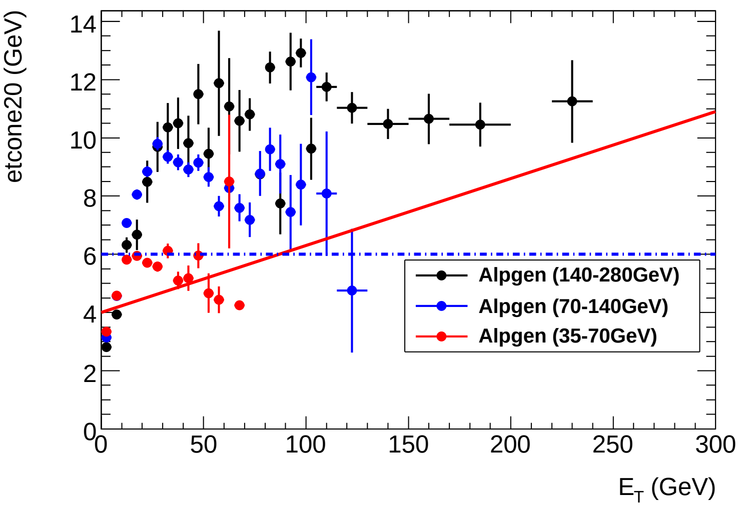

Figure 5.10: Average E_T^{cone20} distribution versus E_T for electrons that pass all standard ID requirements, in simulated di-jet events (with different jet transverse momentum thresholds).

5.8 Summary

The features of the calorimeter isolation variable E_T^{cone20} for W-electrons in top quark events and for electrons in $Z \to e^+e^-$ decays has been studied. It was found that due to increased electromagnetic shower size, following the previous recommended selection of $E_T^{cone20} < 6$ GeV would affect dramatically the efficiency of selecting high-E_T electrons. We investigated recovering the efficiency at high-E_T via the use of a cut based on the isolation ratio $I_R = E_T^{cone20}/E_T < 0.1, 0.12$ which is a significant improvement. However accounting for the calorimeter noise present in the detector via a cut of the form E_T^{cone20} <C$_1$+C$_2$ $\cdot$ E_T gives the optimal performance as it follows the natural E_T^{cone20} distribution versus E_T. This maximises the isolated electron efficiency against background rejection. The constant C_2 is due to electromagnetic shower size and can be easily determined in Monte Carlo simulations and its effect measured in the efficiency from $Z \to e^+e^-$ data. The constant term $C_1 \simeq 3.5 - 4.0$ GeV, as it appears in current simulations, presumably comes from calorimeter noise and its value can be set a-priori and then optimised using E_T^{cone20} profile plots versus E_T from $Z \to e^+e^-$ data.

As a result of this study and presentations to the top-quark working group within ATLAS, the cut of the form $E_T^{cone20} <\mathrm{C}_1+\mathrm{C}_2 \cdot E_T$ was made a standard cut on all top quark analyses selecting isolated electrons as of February 2010. Also the first measurement of the $t\bar{t}$ production cross section at $\sqrt{s} = 7$ TeV [58] utilised this cut for selecting isolated electrons.

Chapter 6

Soft Muon Tagging Efficiency in J/ψ Events

6.1 Introduction

The narrow resonance of the J/ψ production and its decay $J/\psi \rightarrow \mu\mu$ is an ideal sample for performance studies of the muon system within ATLAS. Understanding the muon reconstruction efficiencies is of particular importance for this analysis in regards to identifying soft muons from b-quark decay, and the J/ψ production of low p_T muons is an ideal channel to study this. This analysis focuses on the muons from the J/ψ decay within the ATLAS detector from the first months of operation, with the aim to calculate initial combined muon reconstruction efficiency and data vs. Monte Carlo scale factors. The quantity detailed in Section 4.4.3, χ^2_{match}, is studied in this analysis and an initial efficiency and scale factor calculated from data. The efficiency measurement of χ^2_{match} and scale factor information calculated in this section will then be used in Section 7 as part of the top-quark pair production cross section measurement.

The mechanisms by which the production of prompt charmonium states occur will not be covered in this analysis, nor will there be investigations of the production cross section and other areas of J/ψ study, such as polarisation. The various experiments that have investigated heavy quark production in high energy hadronic collisions and their findings are detailed in [59] and offer an insight into the variety of potential measurements within ATLAS.

6.2 Soft Muon Tagging

The ATLAS soft muon tagging (SMT) algorithm [45] can be applied to a sample of jets to significantly enhance the heavy flavour content of that sample. It relies on the branching fraction of b-hadron decays via $b \to \mu\nu X$ or $b \to cX \to \mu\nu X$ resulting in 20% of b decays producing a muon. X denotes a hadronic system of one or more mesons. The standard SMT algorithm within ATLAS looks for reconstructed muons within $\Delta R < 0.5$ of a jet and because of the high purity of the muon reconstruction at ATLAS a relatively large light-jet rejection rate can be achieved, details in Table 6.1. Light-jets refer to light-quark (u and d) or gluon jets.

The performance of the SMT algorithm can be further enhanced by making use of the muon-jet p_T^{rel}: the muon momentum in the plane orthogonal to the jet axis (axis of the cone encompassing the jet), after the jet axis has been corrected for the presence of the muon. The jet axis is recalculated by adding the muon momentum to it. Real muons that are the result of the decay of the heavier b-hadrons will tend to have a larger p_T^{rel} than those resulting from pion/kaon decays or fakes. The current SMT algorithm includes the use of a cut on the 1-D likelihood ratio built from simulated Monte Carlo p_T^{rel} distributions of light-jets and b-jets. It was demonstrated in [59], that a light jet rejection (LJR) factor of 380 could be achieved for a b-jet tagging efficiency (ϵ_b) of 10% using p_T^{rel} based likelihood tagging which included the semi-leptonic branching ratios, the detector acceptance, muon reconstruction efficiency and jet-muon association efficiency.

An alternative variable that can be used to enhance the light-jet rejection is detailed in

Section 4.4.3 and is defined as the χ^2_{match} of the match between the Muon Spectrometer and Inner Detector tracks of a combined muon. Studies detailed in [60] and summarised in Table 6.1 show that cutting directly on this variable with a value of $\chi^2_{match} < 3.2$ can achieve a performance in $t\bar{t}$ simulated events that is at least as good as using p_T^{rel} but with the following advantages:

- The χ^2_{match} variable is part of the combined muon reconstruction algorithm and as such does not require the presence of a jet. Therefore, assuming no dependence from surrounding particles, the efficiency can be determined using $J/\psi \to \mu\mu$, $\Upsilon \to \mu\mu$ and $Z \to \mu\mu$ "tag and probe" techniques [61], of which the $J/\psi \to \mu\mu$ channel will be studied here.
- The ability of the p_T^{rel} variable to discriminate between reconstructed muons in b-jets and reconstructed muons in light-jets diminishes at high jet E_T, whereas the χ^2_{match} variable is not affected in the same way [60].

In Section 6.4, the efficiency of the $\chi^2_{match} < 3.2$ requirement will be investigated using the ATLAS $J/\psi \to \mu\mu$ data.

	p_T^{rel}-tagger		χ^2_{match}-tagger	
ϵ_b	p_T^{rel}-weight > X	LJR	χ^2_{match} <X	LJR
8%	3.7	790 ± 19	1.8	740 ± 17
9%	3.4	585 ± 12	2.3	595 ± 12
10%	3.14	430 ± 8	3.2	470 ± 9
11%	2.93	310 ± 5	6.0	330 ± 5

Table 6.1: Comparison of light jet rejections factors for several b-tagging efficiency operating points of the χ^2_{match}-tagger and p_T^{rel}-tagger using the purified light jet sample (as defined in the text) [60].

The light jet rejection factors quoted in Table 6.1 were calculated excluding light jets in the vicinity of which a b-jet, c-jet, or tau lepton was found (within a cone of size $\Delta R = 0.8$). The light jet sample obtained after this additional selection is referred to here as the *purified* light jet sample.

6.3 Data and Monte Carlo samples

6.3.1 Data sample

The collision data at a centre-of-mass energy of 7 TeV, taken between June 24th and August 29th 2010 is included in this analysis and covers Atlas data periods "D" through to "F". Only the luminosity blocks that have been declared good are used in this analysis following the guidelines set out by the Atlas muon group. The criteria for a good luminosity block covers the state of all the relevant Atlas detector elements and that the LHC beam is also stable.

For this analysis the MS, ID and magnet system are required to be fully functional so that the data is of sufficiently high quality to be suitable for physics analysis. Taking into account the luminosity block selection, the total integrated luminosity for the sample is calculated to be 3.1±0.3 pb^{-1}. The details of each run period are shown in Table 6.2.

Period and Atlas Run Numbers	Integrated Luminosity (nb^{-1})
D:158045-159224	311.83
E:160387-161948	893.29
F:162347-162882	1856.81
Total	3061.92

Table 6.2: The recorded luminosity for the runs in periods D and F, after removing the luminosity blocks that are flagged as unsuitable for physics analysis.

6.3.2 Monte Carlo sample

Monte Carlo comparisons were made using signal samples generated with the PYTHIA 6 [32] program, tuned using the Atlas MC09 tune [62] and MRST LO* [63] parton distribution functions. The signal J/ψ event samples rely on the Pythia implementation of prompt J/ψ production sub-processes that have been tuned to describe Tevatron results [64]. The prompt J/ψ production includes direct production from the hard interaction, as well as radiative feed-down from $\chi_c \rightarrow J/\psi\gamma$ decays. Included at the generator level there is a $p_T > 4$GeV and $|\eta| < 2.5$ cut on the muons.

6.4 Event and candidate selection

As detailed earlier in Section 2, the ATLAS detector covers almost the full solid angle around the collision point with many differing detectors, calorimeters and muon chambers. For this analysis, the trigger system, inner detector and muon spectrometer are of particular importance for the detection of low-p_T muons.

The data used in this analysis was taken during periods where elements of the ATLAS detector were still being commissioned and the instantaneous luminosity was rising from run to run. For this analysis we have relied on the use of the Minimum Bias Trigger Scintillators (MBTS) at the final event filter level (EF). The MBTS is based on scintillators mounted at each end of the detector in front of the LAr calorimeter cryostats at $z = \pm 3.56$ m, segmented into eight sectors in azimuth and two rings in pseudo-rapidity ($2.09 < |\eta| < 2.82$ and $2.82 < |\eta| < 3.84$). The MBTS trigger is configured so that it requires two hits above threshold from either side of the detector from which a dedicated muon trigger at the EF level is used to confirm the candidate events.

A particle in a solenoidal field follows a helical trajectory that can be parametrised with five track parameters as shown in Figure 6.1; two of those parameters, which are particularly relevant for this analysis are:

- The transverse impact parameter $d0$, which is the distance of the closest approach of the track projected into the $x-y$ plane relative to the nominal interaction point.
- The longitudinal impact parameter z_0, which is the z value of the point of closest approach determined as above.

There also exists the ability to distinguish between prompt and non-prompt J/ψ within

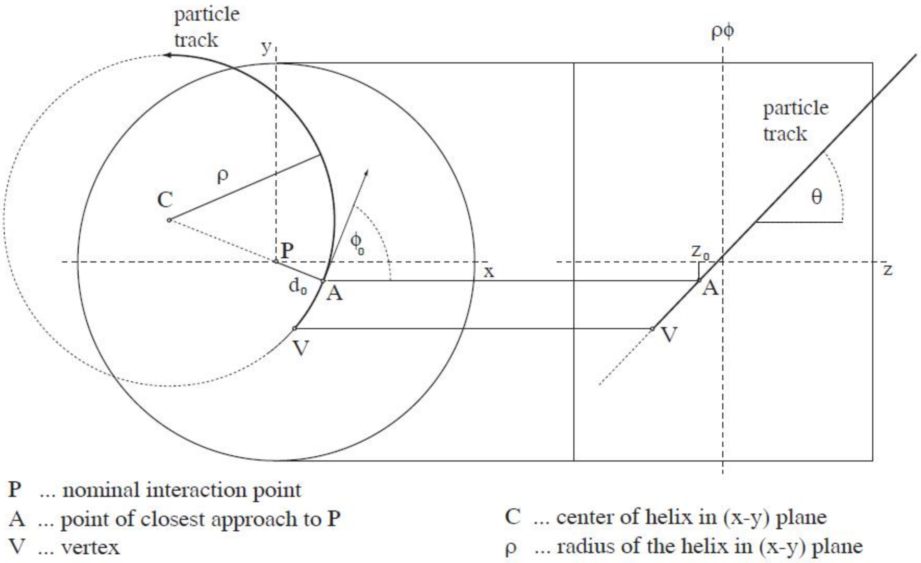

Figure 6.1: The five track parameters, split into three transverse values ($x - y$ plane) and two longitudinal values ($r - z$ view) for a helix track in a cylindrical detector geometry [65].

data by using the radial displacement, L_{xy}, of the two-track vertex from the beamline to calculate the pseudo-proper time t_0, as defined by:

$$t_0 = \frac{L_{xy} \cdot M_{J/\psi}}{p_T(J/\psi) \cdot c} \tag{6.1}$$

where $M_{J/\psi}$ and $p_T(J/\psi)$ represent the J/ψ invariant mass and transverse momentum, c is the speed of light in vacuum. Prompt J/ψ decays will have a zero pseudo-proper time whereas non-prompt J/ψ primarily come from B-hadron decays with an exponentially decaying pseudo-proper time distribution due to the lifetime of the parent B-hadrons. It has been shown that a pseudo-proper time cut of less than $0.2ps$ will allow to retain prompt J/ψ with an efficiency of 90% and a purity of 97% [66].

6.4.1 Tag and Probe Method

The tag and probe method [55] requires muon pairs that are selected by having one well reconstructed muon, the “tag”, and an inner detector track, the “probe”, with an invariant mass that is consistent with coming from a $J/\psi \to \mu^+\mu^-$ decay. This method allows for the “probes” to be selected independently of the Atlas muon spectrometer and can be used to measure the efficiency for reconstructing a muon based on the muon spectrometer, a combined muon.

After selecting an inner detector track and muon pair that are within the J/ψ invariant mass window, which is defined in Section 6.6.1, the efficiency of the combined muon reconstruction algorithm can then be determined from Equation 6.2.

$$\epsilon = \frac{J/\psi \text{ candidates reconstructed with a muon probe}}{J/\psi \text{ candidates reconstructed with an inner detector probe}} \tag{6.2}$$

The muon probe collection is a sub-set of all the inner detector probes that have been reconstructed using the combined muon reconstruction algorithm discussed in Section 4.4.3.

We also measure the efficiency of a cut of type $\chi^2_{match} < X$ on the reconstructed combined muon, this is simply defined as:

$$\epsilon = \frac{J/\psi \text{ candidates reconstructed with a muon probe and } \chi^2_{match} < 3.2}{J/\psi \text{ candidates reconstructed with a muon probe}} \tag{6.3}$$

6.4.2 Tag Selection Criteria

The requirements on the Tag muon candidates are:

- The track should be a combined muon.
- The combined muon should be within the geometrical acceptance of the Inner

Detector, $|\eta| < 2.5$.

- The p_T of the combined muon must be $p_T > 4.0$ GeV.
- Reconstructed tracks should have at least 1 hit in the Pixel and at least 6 hits in the SCT system.
- Tracks that fall within the acceptance of the TRT ($|\eta| < 2.0$) are required to have 10 TRT hits.
- The impact parameter (d_0) and distance in the z-direction (z_0) of the track with respect to the Primary Vertex should be $d_0 < 1.0$ mm and $z_0 < 5.0$ mm and the corresponding significances should be less than 2.5.
- The tag is also required to match to at least one of the muon triggers requested in the event selection; the matching with the L1_ MU0 trigger item is satisfied if the tag is in the region of interest where the L1 trigger was produced.

6.4.3 Probe Selection Criteria

The probe candidates are picked from the reconstructed inner detector track pool according to the following criteria:

- The same hit quality cuts on the reconstructed track as those for the Tag.
- The probe track should not match the electron IsEM "medium" flag, which would imply that the muon is likely an electron candidate.
- The probe must be of opposite charge to the tag.

The muon probe candidates are all combined muon tracks matching the same criteria as the inner detector probe tracks, with the addition of being reconstructed as combined muons. To calculate the efficiency of the χ^2_{match} muon variable detailed in Section 4.4.3 a further probe collection is created, satisfying the requirement $\chi^2_{match} < 3.2$; this selection is a further sub-set of the muon probe collection.

6.4.4 J/ψ Selection Criteria

The tag and probe criteria used to select possible J/ψ candidates and remove potential backgrounds follows that laid out in [61] and is:

- Tag and Probe candidates are required to have emerged from a common vertex.
- The χ^2 of the fit to the vertex should be below 6.
- The pseudo-proper time of the reconstructed J/ψ should be less than $< 0.2ps$ in order to help reject the dominant $b\bar{b} \to \mu X$ and $c\bar{c} \to \mu X$ backgrounds. As a result most indirect J/ψ's will be sacrificed by applying this cut.
- The separation in ΔR between the tag and probe should be $0.1 < \Delta R < 0.7$ to help eliminate non-prompt J/ψ. The separation angle ΔR provides a background rejection of more than a factor of 5 for the two dominant background modes: $b\bar{b} \to \mu\chi$ and $c\bar{c} \to \mu\chi$, and more than a factor of 1.5 for the combinatorial background of both prompt and indirect J/ψ.
- At least one of the muons in each pair is required to be a combined muon.

6.5 Fit of J/ψ mass distributions

The invariant mass of all J/ψ candidates passing the required criteria with an inner detector probe is shown in Figure 6.2a and for all J/ψ candidates with a muon probe is shown in Figure 6.2b from data. The fit to the invariant mass was done by modelling the background with a one dimensional polynomial and the signal region with a Gaussian. The combined function of the one dimensional polynomial and the Gaussian is then minimized through ROOT (a data analysis framework [67]) using MINUIT [68] to produce the fit and parameters shown.

The signal region is defined by the range $\pm 3\sigma$ from the reference mass of the J/ψ of 3.071 GeV. The reference mass is used instead of the returned value of the mass from

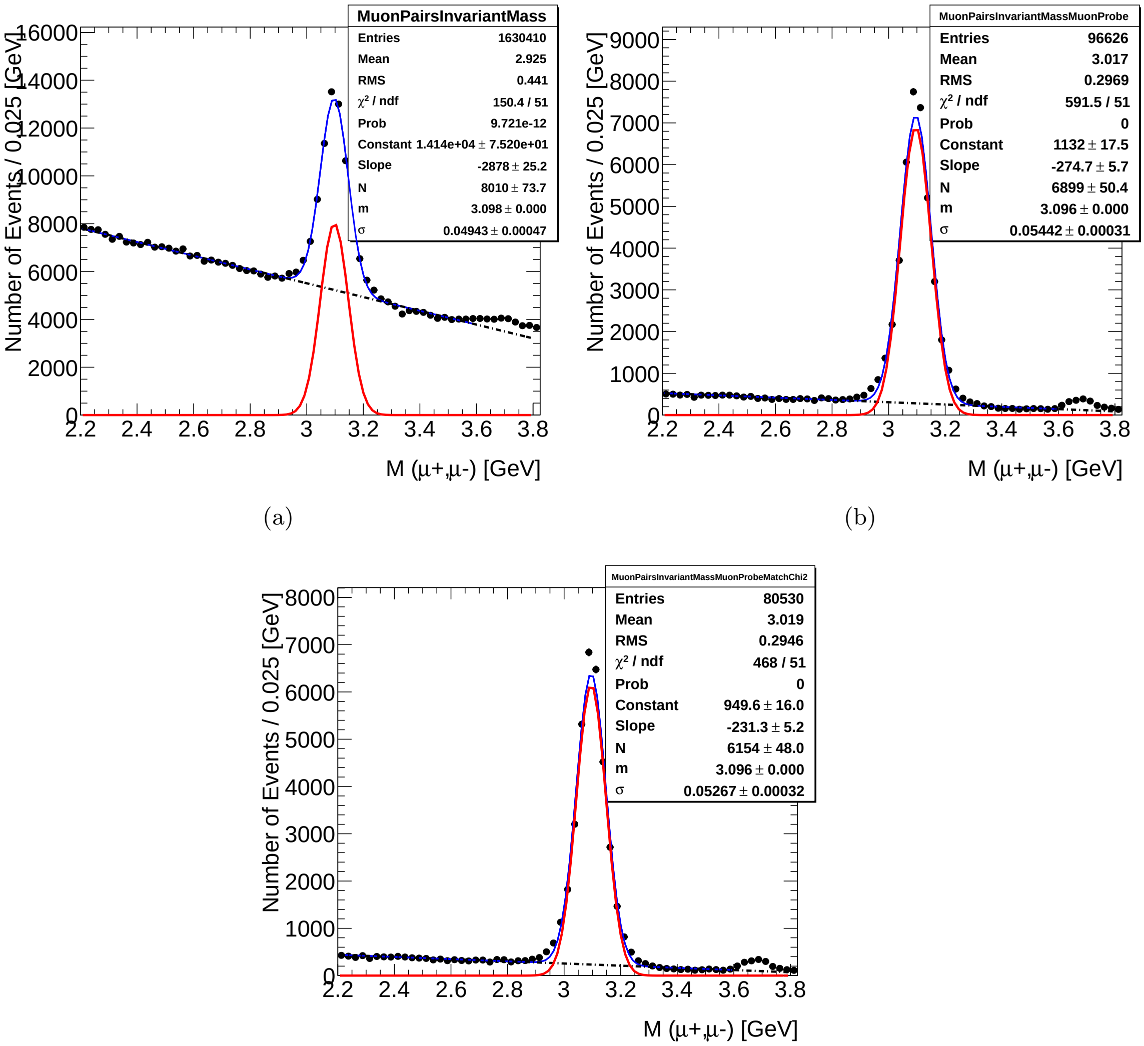

(a)

(b)

(c)

Figure 6.2: The invariant mass of all muon pair candidates reconstructed with an inner detector probe (a), reconstructed with a muon probe (b) and that have passed the χ^2_{match} requirement (c), all from data.

the fit as we are not concerned with a measurement of the J/ψ but to keep a consistent signal region for measuring muon reconstruction efficiency. The signal region is defined from the inner detector probe plot for calculating the combined muon reconstruction efficiency and from the muon probe plot for calculating the efficiency of the $\chi^2_{match} < 3.2$ requirement.

The signal is calculated by removing the area under the background fit from the total integral in the defined 3σ regions. The ratio between the calculated signal in the numerator and denominator plots is then used as a measure of the efficiency for the relevant reconstruction algorithm.

The small peak in the invariant mass distribution at ≈ 3.7 GeV is caused by the ψ', which has a mass of 3686 MeV and is an excited $c\bar{c}$ hadron. It will decay very quickly into a variety of states, but sometimes into two pions and a J/ψ. When fitting the background, the region around 3.7 GeV is excluded from the fit.

The results of the efficiency calculations are shown in Section 6.8.

For Monte Carlo simulations, the same procedure is used to calculate the signal but as the simulations include only signal there is no background subtraction in the defined regions.

6.6 Systematic studies

This section will discuss the systematic uncertainties present within this analysis and to what level they affect the accuracy of the muon and χ^2_{match} reconstruction measurement. We will investigate the systematic effects due to:

- Signal fit procedure
- Background shape used in the fit

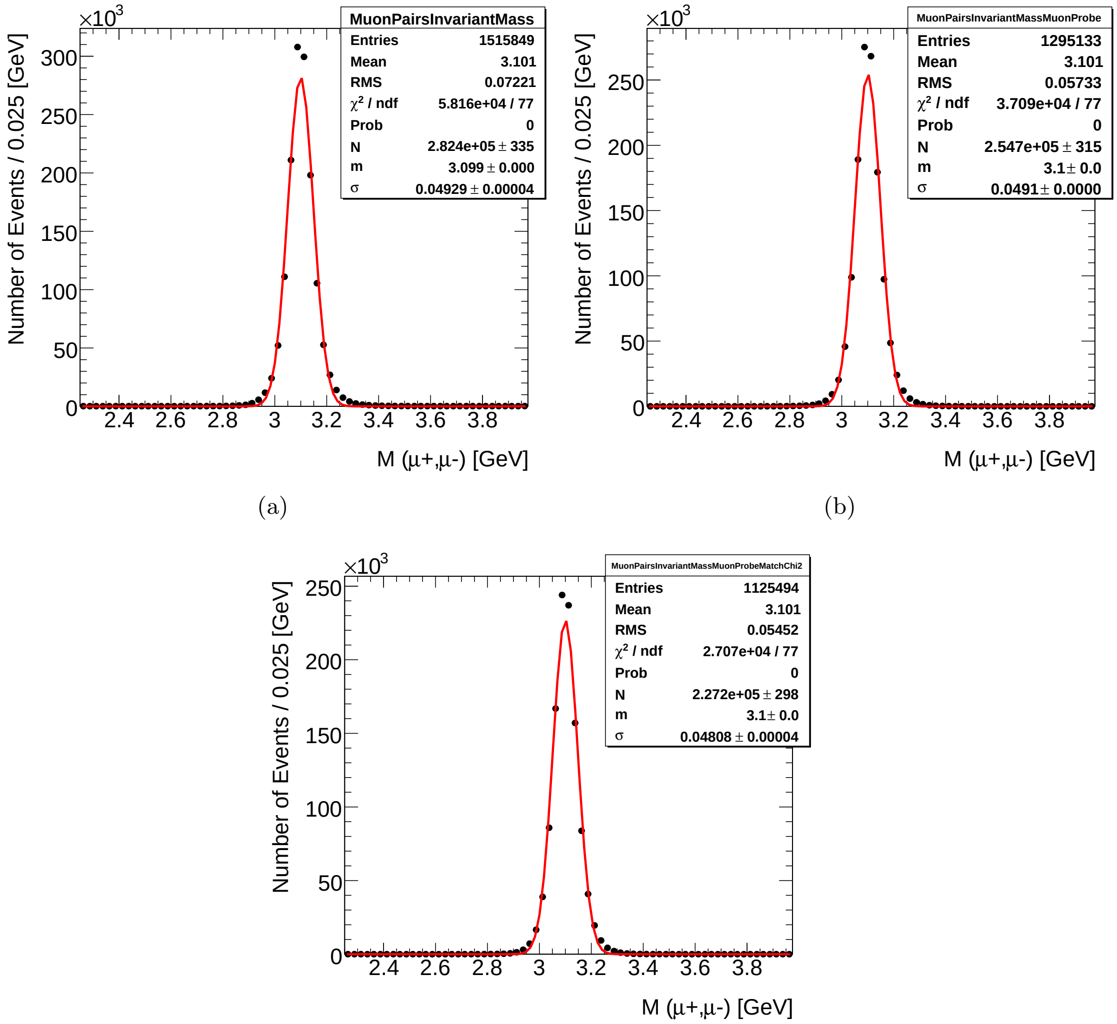

(a)

(b)

(c)

Figure 6.3: The invariant mass of all muon pair candidates reconstructed with an inner detector probe, (a), reconstructed with a muon probe (b) and that have passed the χ^2_{match} requirement (c), all from Monte Carlo.

6.6.1 Signal fit

The systematic uncertainty from fitting the J/ψ signal was calculated by measuring the difference in efficiency by changing the signal region between 3σ and 5σ from the world-average J/ψ mass. Increasing the signal window from 3σ to 5σ should not affect the result, but does help account for bremsstrahlung from the muon that would lower the average mass of the J/ψ and any tracking errors that could result in an incorrect reconstruction of a muon track p_T. An example resulting systematic uncertainty for the combined muon reconstruction efficiency is shown in Appendix B

6.6.2 Background shape

The background systematic was estimated by looking at what effect increasing and decreasing the size of the sideband regions has on the calculated efficiencies. A range of possible efficiencies was also determined by varying the parametrized background slope and constant within their uncertainties. In Figure 6.4 the red and blue dashed lines represents the background with the slope increased and the constant decreased and the blue dashed line the opposite.

The background shape was also examined by looking at same-sign (SS) muon pairs as a possible way to model the background. Figure 6.5 shows that although the shape of the same-sign muon pair background is similar to that of the fitted opposite-sign (OS) signal background, the slope of the same sign background is not “compatible” as a means to model the opposite sign background.

6.7 Statistical uncertainty

The statistical uncertainty was computed using the binomial approximation shown in Equation 6.4, where m is the number of signal probes that pass the required criteria

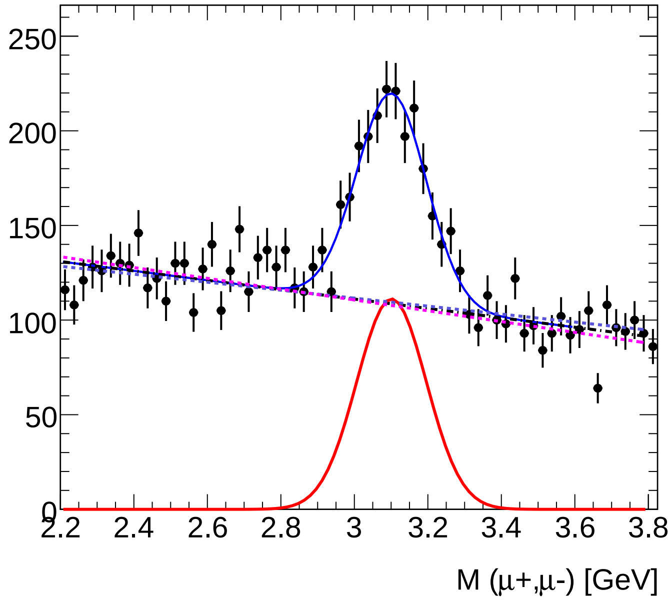

Figure 6.4: The invariant mass plot for a low statistics η region showing the change in the background fits (dashed lines) when the slope and constant are varied according to the returned fit uncertainties. (See text for more details)

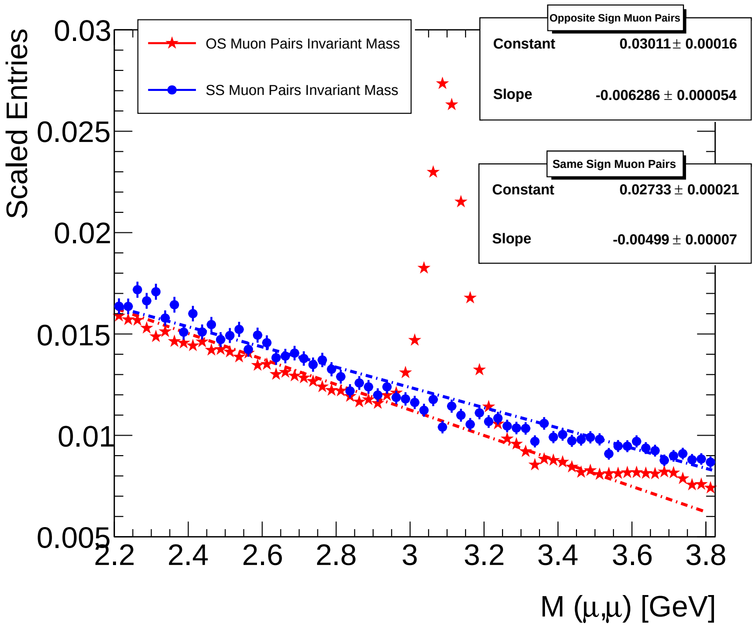

Figure 6.5: The invariant mass of the background of same sign muon pairs overlaid with the J/ψ background fit, for inner detector probes, with the fit parameters shown for each distribution.

set out in Section 6.4.3 and N is the total number of probes before selection. This approximation is valid in all but cases where $\epsilon = 1$ or 0, which is valid for this analysis.

$$\delta\epsilon = \frac{\sqrt{m(1 - m/N)}}{N} \tag{6.4}$$

6.8 Efficiency and Scale Factor measurements

6.8.1 Combined Muon Reconstruction Efficiencies and Scale Factors

The efficiency of the combined muon reconstruction algorithm using 3 pb^{-1} of LHC data at $\sqrt{s} = 7$ TeV is shown in this section. The binning for the plots shown is coarse because of the still limited statistics available but gives a good indication of the initial performance of the muon reconstruction compared to Monte Carlo simulation.

The combined muon reconstruction as a function of probe p_T is shown in Figure 6.6; there is good agreement between Monte Carlo predictions and data in the $p_T = 4 - 8$ GeV range, with a scale factor almost exactly 1. However in the $p_T \geq 8$ GeV range, the efficiency of the combined muon reconstruction diverges from that predicted by Monte Carlo, showing a reduced efficiency. The result of the reduced efficiency measured in this range results in a scale factor for the two higher p_T bins of ≈ 0.85. The reason for this drop has not been completely understood yet. The full efficiencies and scale factors as a function of p_T are given in Table 6.3.

p_T bin [GeV]	Data Efficiency [%]	MC Efficiency [%]	Scale Factor
4–6	86.6 ± 0.3	86.7 ± 0.1	1.00 ± 0.01
6–8	96.2 ± 1.1	94.9 ± 0.4	1.01 ± 0.01
8–10	83.2 ± 1.0	94.9 ± 0.5	0.88 ± 0.01
10+	80.9 ± 1.5	94.0 ± 0.3	0.86 ± 0.02
Total	90.6 ± 0.5	89.6 ± 0.2	1.01 ± 0.01

Table 6.3: The combined muon reconstruction efficiency as a function of p_T.

Figure 6.7 shows the efficiency as a function of η. The "U" shape of this plot can

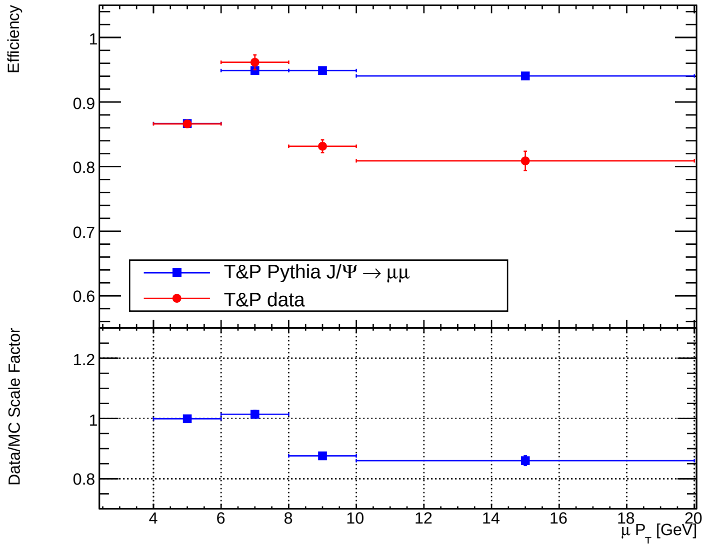

Figure 6.6: The measured efficiency of the combined muon reconstruction algorithm as a function p_T with the scale factor as a function of p_T shown below.

be explained by the gaps in the muon system coverage. Namely the central gap at $\eta = 0$ and the barrel to endcap transition region at $\eta = \pm 1.2$, reduce the average efficiency in the central region. This is modelled well in Monte Carlo, has been studied previously [45] and can be seen in Figure 6.8. The current measurements in η show agreement between data and Monte Carlo for all but one data point within the measured uncertainties. The scale factors vary across the η range but are consistently below 1 except the $\eta \geq 2$ bin. The measured efficiencies and scale factors as a function of η are given in Table 6.4.

η bin	Data Efficiency [%]	MC Efficiency [%]	Scale Factor
(-3)–(-2)	96.8 ± 9.4	100.6 ± 1.0	0.96 ± 0.09
(-2)–(-1)	83.3 ± 7.6	91.2 ± 0.1	0.91 ± 0.08
(-1)–0	83.3 ± 7.7	85.3 ± 0.1	0.98 ± 0.09
0–1	86.2 ± 3.9	86.9 ± 0.1	0.99 ± 0.05
1–2	86.1 ± 2.1	91.4 ± 0.1	0.94 ± 0.02
2–3	101.7 ± 4.8	100.5 ± 1.0	1.01 ± 0.05

Table 6.4: The combined muon reconstruction efficiency as a function of η.

The geometrical effect of the detector feet on the muon reconstruction efficiency in ϕ, shown to occur in [45] (see also Figure 6.10), is not visible in Figure 6.9 because of the

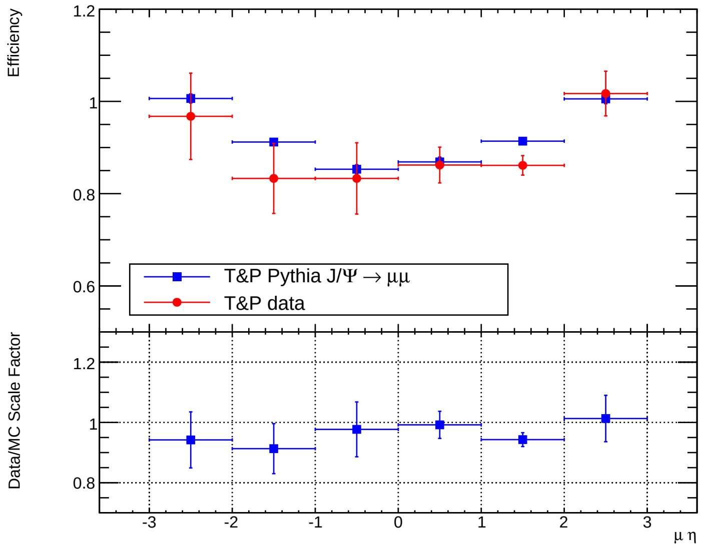

Figure 6.7: The measured efficiency of the combined muon reconstruction algorithm as a function of η, with the scale factor as a function of η shown below.

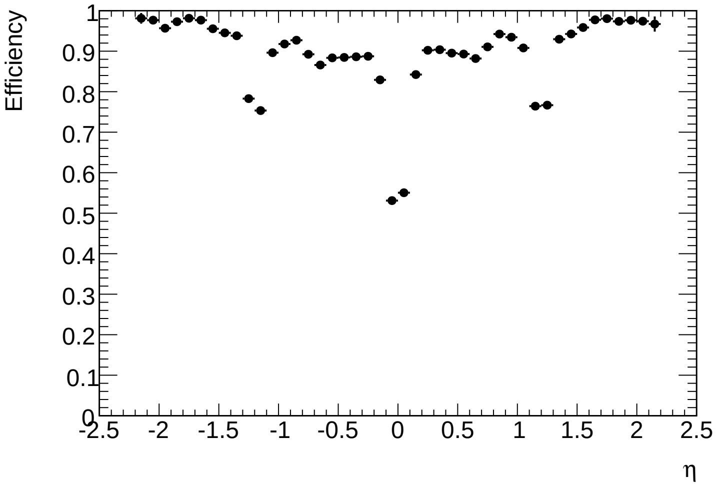

Figure 6.8: The efficiency of the combined muon reconstruction algorithm as a function of η from Monte Carlo, showing the dips in efficiency caused by gaps in the muon system at $\eta = 0$ and the barrel to endcap transition at $\eta = \pm 1.2$.

coarse binning used due to low statistics currently from data. There is also a distinct difference in efficiency as a function of ϕ between Monte Carlo simulations and data measurements, with all the data measurements showing a reduced efficiency compared to Monte Carlo predictions. This results in scale factors all below 1 as a function of ϕ. Table 6.5 details the efficiencies and scale factors as a function of ϕ.

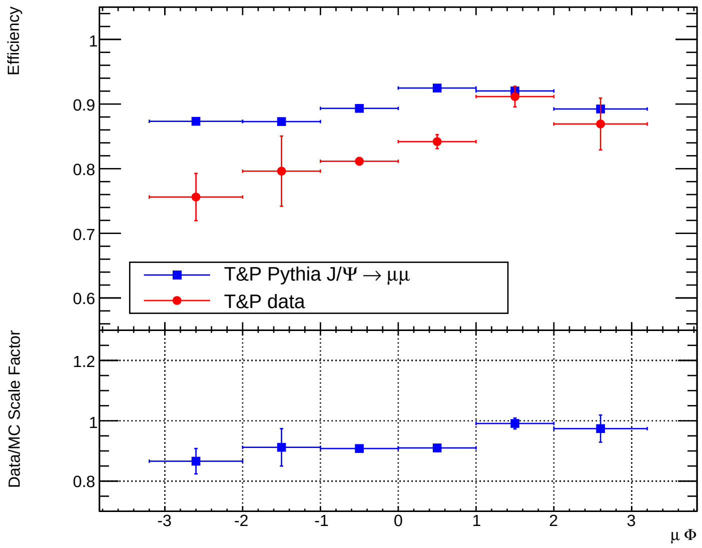

Figure 6.9: The measured efficiency of the combined muon reconstruction algorithm as a function of ϕ, with the scale factor as a function of ϕ shown below.

ϕ bin	Data Efficiency [%]	MC Efficiency [%]	Scale Factor
(-3.2)–(-2)	75.6 ± 3.7	87.3 ± 0.2	0.87 ± 0.04
(-2)–(-1)	79.6 ± 5.4	87.3 ± 0.1	0.91 ± 0.06
(-1)–0	81.2 ± 0.6	89.3 ± 0.2	0.91 ± 0.01
0–1	84.2 ± 1.1	92.5 ± 0.3	0.91 ± 0.01
1–2	91.2 ± 1.6	92.0 ± 0.3	0.99 ± 0.02
2–3.2	86.9 ± 4.0	89.2 ± 0.2	0.97 ± 0.05

Table 6.5: The combined muon reconstruction efficiency as a function of ϕ.

6.8.2 χ^2_{match} Efficiencies

All muon probe candidates that passed the combined muon reconstruction algorithm will have a χ^2_{match} value associated to them that determines the quality of the muon-track matching. Requiring $\chi^2_{match} < 3.2$ as explained in Section 6.2, the same cut that

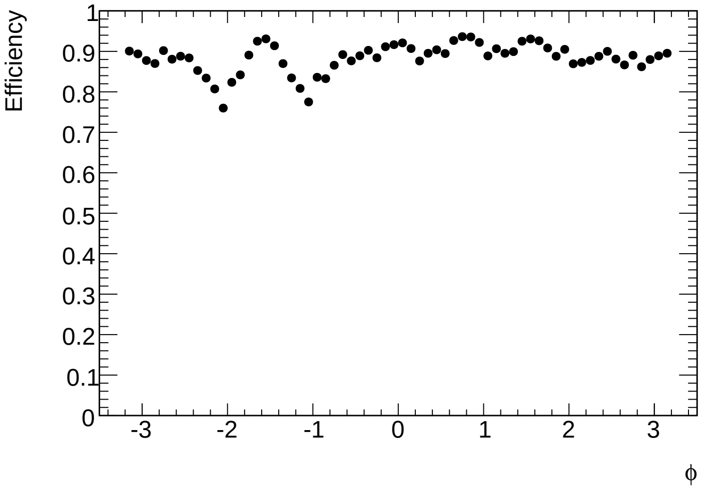

Figure 6.10: The efficiency of the combined muon reconstruction algorithm as a function of ϕ from Monte Carlo, showing the dips in efficiency caused by the detector feet.

will be preformed in the top quark cross-section analysis 7, allows us to look at the efficiency of that cut on soft muons from J/ψ decay. Figure 6.11 shows the χ^2_{match} of all probe candidates that have been reconstructed with the combined muon algorithm.

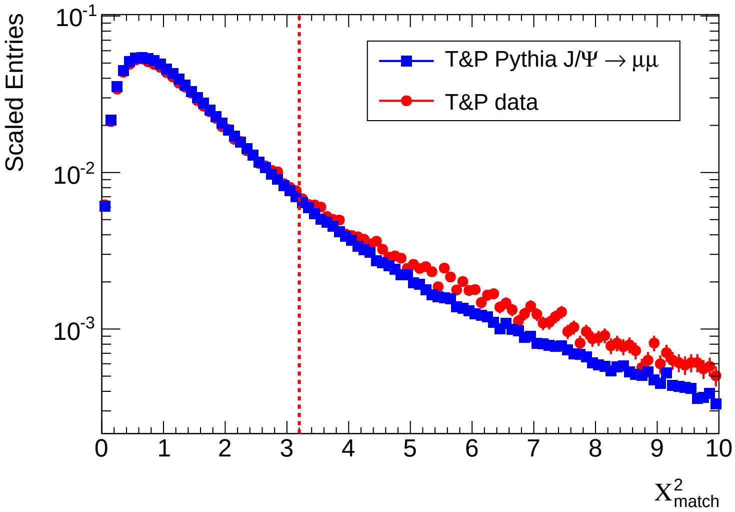

Figure 6.11: The measured χ^2_{match} of all muon probes having passed the combined muon requirement in data and $J/\psi \to \mu\mu$ Monte Carlo simulations.

Figure 6.12 shows the efficiency of the χ^2_{match} cut as a function of p_T after all probes have passed the combined muon requirement. The efficiency of the χ^2_{match} cut is seen to be very well modelled in Monte Carlo, with all scale factors very close to 1. Table 6.6 shows the efficiencies and scale factors as a function of p_T.

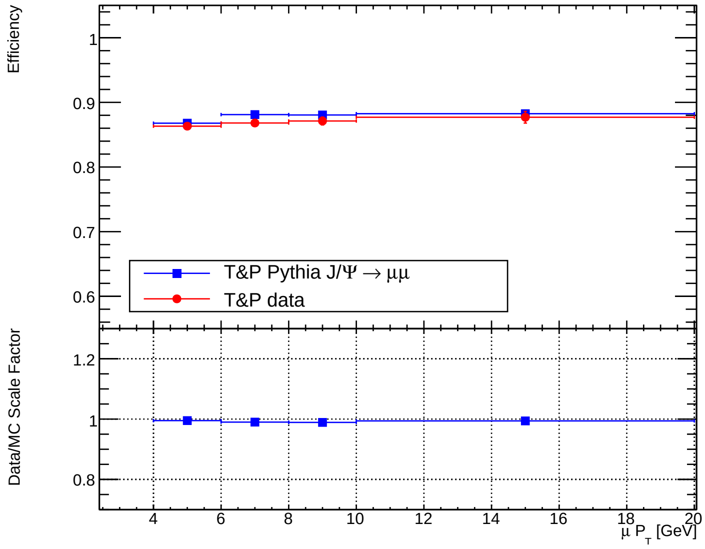

Figure 6.12: The measured efficiency of the $\chi^2_{match} < 3.2$ cut as a function of p_T with the scale factor as a function of p_T shown below.

p_T bin [GeV]	Data Efficiency [%]	MC Efficiency [%]	Scale Factor
4-6	85.7 ± 0.4	86.8 ± 0.3	1.00 ± 0.01
6-8	87.1 ± 0.5	88.1 ± 0.4	0.97 ± 0.01
8-10	87.7 ± 0.6	88.1 ± 0.5	0.99 ± 0.01
10+	86.7 ± 0.9	88.3 ± 0.4	0.99 ± 0.01
Total	86.3 ± 0.3	87.3 ± 0.3	0.99 ± 0.01

Table 6.6: The $\chi^2_{match} < 3.2$ cut efficiency in several p_T bins for all combined muon probe candidates.

The efficiency of the $\chi^2_{match} < 3.2$ as a function of η is shown in Figure 6.13, which indicates that there are some differences between Monte Carlo modelling and the measured values; this is especially the case in the η range between -2 and -1, where the measured efficiency in data is of the order $\approx 10\%$ less than Monte Carlo. This bin includes the barrel-endcap transition region in the detector and it could be possible that certain material aspects of the detector are not fully modelled. A finer binning in this region would help investigate the potential cause of this loss in efficiency but requires more statistics than the 3.1pb^{-1} available for this analysis. In other η bins there are small variations in data from Monte Carlo, but no further large discrepancies, Table 6.7 shows the complete efficiencies and scale factors as a function of η.

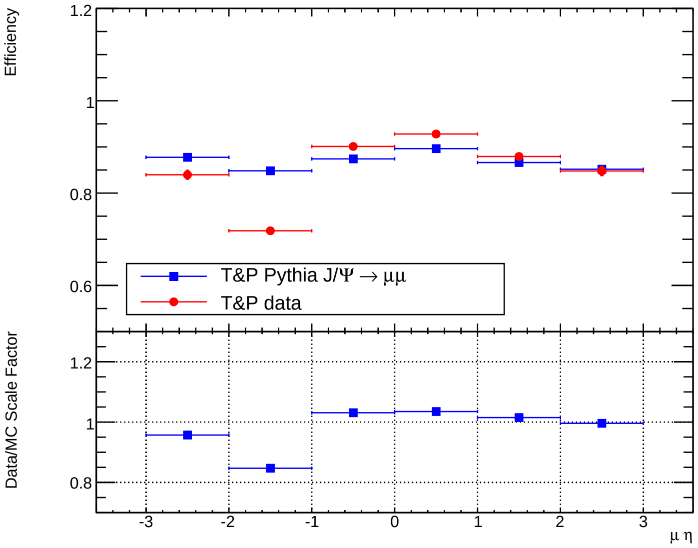

Figure 6.13: The measured efficiency of the $\chi^2_{match} < 3.2$ cut as a function of η with the scale factor as a function of η shown below.

η bin	Data Efficiency [%]	MC Efficiency [%]	Scale Factor
(-3)-(-2)	84.0 ± 1.0	87.8 ± 0.5	0.957 ± 0.012
(-2)-(-1)	71.8 ± 0.7	84.8 ± 0.3	0.847 ± 0.008
(-1)-0	90.1 ± 0.4	87.4 ± 0.1	1.031 ± 0.005
0-1	92.8 ± 0.3	89.6 ± 0.1	1.035 ± 0.003
1-2	87.9 ± 0.4	86.6 ± 0.4	1.015 ± 0.006
2-3	84.8 ± 1.0	85.2 ± 0.5	0.996 ± 0.013

Table 6.7: The $\chi^2_{match} < 3.2$ cut efficiency in several η bins for all combined muon probe candidates.

The dependence of the $\chi^2_{match} < 3.2$ cut as a function of ϕ is shown in Figure 6.14, it shows very good agreement between Monte Carlo and data, with all scale factors very close to 1. There are no bins showing large differences between data and Monte Carlo. Full details of the efficiencies and scale factors are shown in Table 6.8.

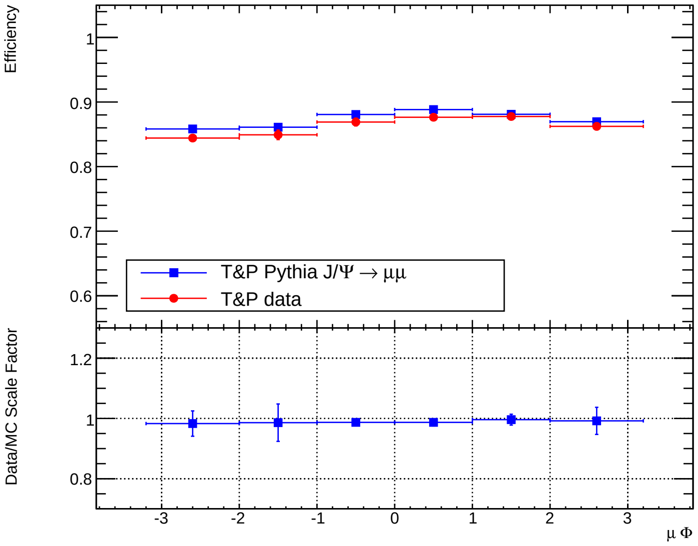

Figure 6.14: The measured efficiency of the $\chi^2_{match} < 3.2$ cut as a function of ϕ with the scale factor as a function of ϕ shown below.

ϕ bin	Data Efficiency [%]	MC Efficiency [%]	Scale Factor
(-3.2)-(-2)	84.4 ± 0.5	85.8 ± 0.4	0.983 ± 0.007
(-2)-(-1)	84.9 ± 0.7	86.1 ± 0.4	0.986 ± 0.010
(-1)-0	86.9 ± 0.6	88.1 ± 0.4	0.987 ± 0.008
0-1	87.6 ± 0.5	88.8 ± 0.3	0.987 ± 0.006
1-2	87.8 ± 0.5	88.1 ± 0.3	0.996 ± 0.006
2-3.2	86.2 ± 0.5	87.0 ± 0.3	0.992 ± 0.007

Table 6.8: The $\chi^2_{match} < 3.2$ cut efficiency as a function of ϕ for all combined muon probe candidates.

6.8.3 χ^2_{match} Efficiency as a function of isolation

The purpose of investigating the efficiency of the $\chi^2_{match} < 3.2$ cut in J/ψ data is to understand the behaviour of soft muons within data, and then extrapolating this knowledge for use in soft muon tagging in b-jets within $t\bar{t}$ events. One of the major factors that could affect the efficiency of reconstructing muons within b-jets is localised jet activity around the muon, producing other charged tracks and particles that could interfere in the detection of muons from the decay of the b quark.

It is therefore important to try to understand the χ^2_{match} efficiency as a function of isolation.

Muon probe isolation was studied using three different isolation variables;

- Calorimetric isolation, E_T^{cone}, which is described in detail in Section 4.4.5;
- Track based isolation, p_T^{cone}, the sum of the p_T of all tracks with a $p_T > 1$ GeV within a given cone size, minus the object track p_T;
- Number of tracks within a give cone size, known as nu^{cone}.

Figure 6.15 shows the $\chi^2_{match} < 3.2$ cut efficiency as a function of E_T^{cone30}. There is very good agreement between Monte Carlo simulations and data, with all scale factors being very close to 1. Importantly as well the efficiency of the $\chi^2_{match} < 3.2$ cut is shown to be flat over the range of isolation studied. Negative values of E_T^{cone30} are possible due to noise fluctuations in the calorimeter [69].

Figure 6.16 shows the $\chi^2_{match} < 3.2$ cut efficiency as a function of p_T^{cone30}. There is very good agreement with Monte Carlo predictions. Again all scale factors are close to 1 and the efficiency of the $\chi^2_{match} < 3.2$ is shown to be flat over the range of isolation studied.

The efficiency of the $\chi^2_{match} < 3.2$ cut as a function of nu^{cone30} is shown in Figure 6.17, nu^{cone30} shows similar properties to the other isolation variables: good agreement with

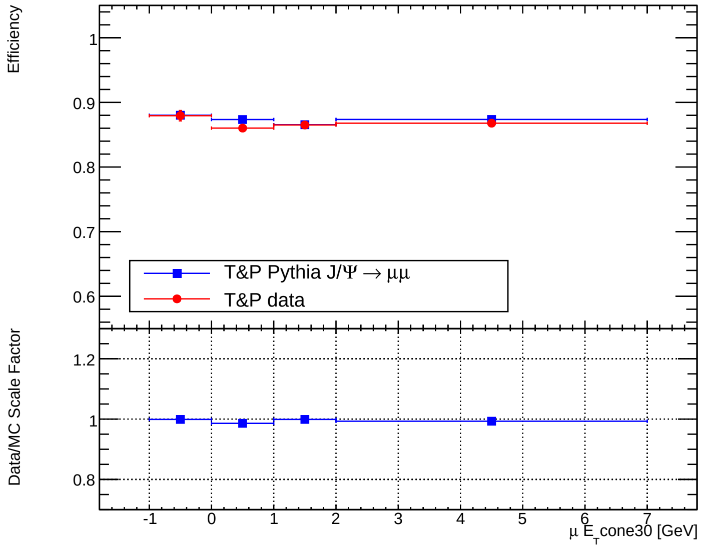

Figure 6.15: The measured efficiency of the $\chi^2_{match} < 3.2$ cut as a function of E_T^{cone30} with the scale factor as a function of E_T^{cone30} shown below.

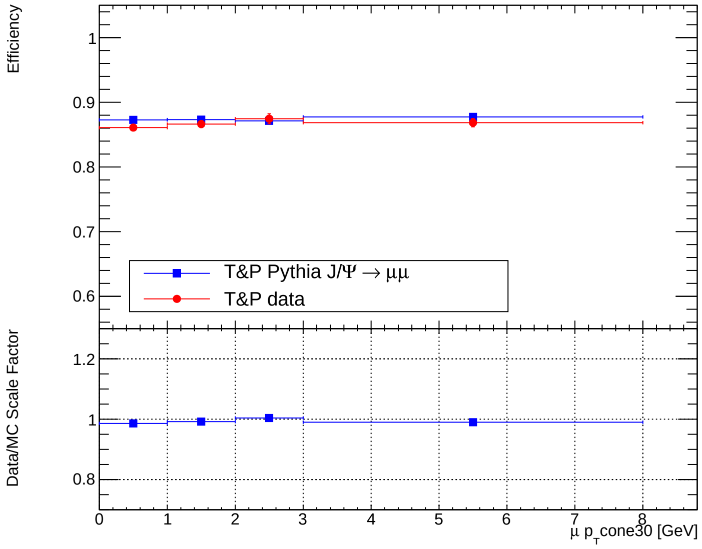

Figure 6.16: The measured efficiency of the $\chi^2_{match} < 3.2$ cut as a function of p_T^{cone30} with the scale factor as a function of p_T^{cone30} shown below.

Monte Carlo predictions and scale factors all close to 1. The efficiency as a function of nu^{cone30} is shown to be flat across the range of isolation studied.

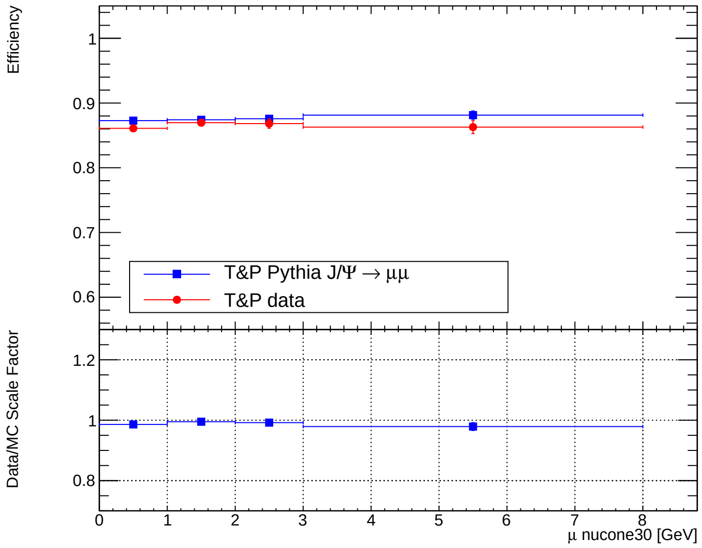

Figure 6.17: The measured efficiency of the $\chi^2_{match} < 3.2$ cut as a function of nu^{cone30} with the scale factor as a function of nu^{cone30} shown below.

The isolation environment within J/ψ events quite evidently will be different to that of $t\bar{t}$ events. Figure 6.18a shows that muon probes within data have a much higher energy density around them than is modelled in direct $J/\psi \to \mu\mu$ Monte Carlo and a much longer tail in the distribution. Even with the differences in Monte Carlo and data, there is good agreement in the highest isolation bins studied and the efficiencies remain flat, indicating that the $\chi^2_{match} < 3.2$ is robust against isolation.

However Figure 6.18b is a reminder that the isolation environment in $t\bar{t}$ events can extend a lot further than in $J/\psi \to \mu\mu$ Monte Carlo. In muon probes from J/ψ data, the mean E_T^{cone30} in J/ψ data is 1.65 GeV, yet in $J/\psi \to \mu\mu$ Monte Carlo the mean is 0.50 GeV and in $t\bar{t}$ Monte Carlo the mean is 24.3 GeV.

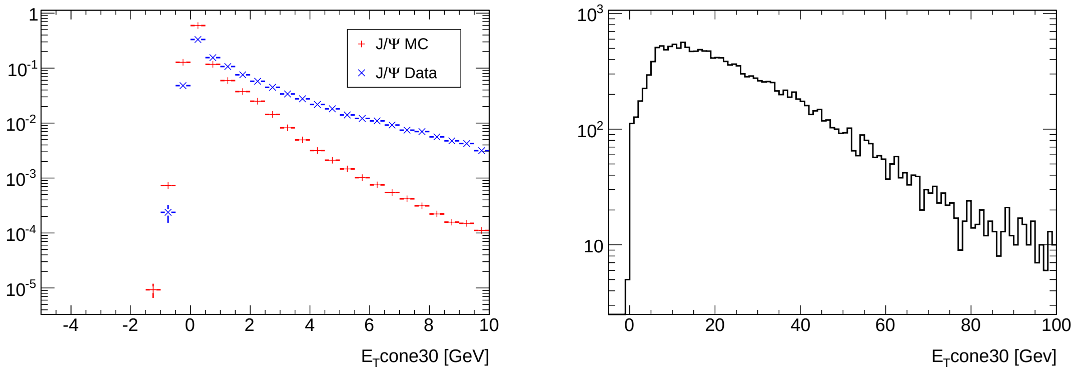

(a) (b)

Figure 6.18: Comparison between the distributions of E_T^{cone30} of muon probes that pass $\chi^2_{match} < 3.2$ in data and $J/\psi \rightarrow \mu\mu$ Monte Carlo simulation shown in Figure (a). Figure (b) shows the distribution of E_T^{cone30} for soft muon candidates that pass $\chi^2_{match} < 3.2$ in $t\bar{t}$ Monte Carlo simulation.

6.9 Summary and conclusions

The efficiency of the combined muon reconstruction algorithm in J/ψ production from LHC first data collisions has been studied and scale factors calculated as a function of p_T, η and ϕ. Also the efficiency of cutting on the χ^2_{match} of combined muons at a value of 3.2 has been studied and scale factors calculated as a function of p_T, η, ϕ and selected isolation variables.

For the muon reconstruction efficiency, there exist notable divergences between Monte Carlo predictions and data measurements for $p_T > 8$ GeV. The effect of the lower than predicted efficiency in this region is not understood and should be studied further with more LHC data.

In the ϕ bins measured there is a reduced efficiency in data in every bin when compared against Monte Carlo. The reason for this divergence was not investigated, but explanations could involve non-perfect alignment of the detector elements or more “dead” material in the detector than simulated, reducing the chance a low-p_T muon will reach the muon chambers and for a combined muon track to be reconstructed. Within the uncertainties calculated there is agreement between Monte Carlo predictions and data for the reconstruction efficiency of the combined muon algorithm within the η ranges measured.

The efficiency of cutting on the χ^2_{match} of combined muons at a value of $\chi^2_{match} < 3.2$ shows good agreement with Monte Carlo in all but one bin of η, with most scale factors close to 1.0. The reason for reduced efficiency in the $\eta = (-2) - (-1)$ bin is not understood, but this is a transition point between the barrel and endcap areas of the detector where there exists are large fraction of "dead" material. Further investigation of this reduced efficiency should be undertaken but fell out of time constraints for this analysis.

The efficiency of the $\chi^2_{match} < 3.2$ cut as a function of different isolation variables shows good agreement with Monte Carlo and is flat across the isolation ranges studied. However it has been noted that the isolation environment in J/ψ events differs greatly from that in $t\bar{t}$ events, for which the efficiency of the $\chi^2_{match} < 3.2$ has been measured for. Therefore any exploration of efficiencies and scale factors to higher isolation events should be done with care.

Future measurements of the efficiency of the χ^2_{match} cut as a function of isolation could aim to include J/ψ production in events with high jet activity as a means of increasing localised jet activity around the muon probes. At the time of writing this was not feasible with the statistics available but should be possible with more collision data.

Chapter 7

Top-Quark Pair Production Cross Section with Soft Muon Tagging

7.1 Introduction

The goal of observing top quark pair production is regarded as one of the key milestones for the early LHC physics program. Measuring the top quark pair production cross section is interesting for several reasons;

- A large $t\bar{t}$ sample is expected to be collected in the first year of data taking, which can be exploited to investigate many aspects of detector performance;
- $t\bar{t}$ production is an important background for several searches for physics beyond the SM;
- New physics at $\sqrt{s} = 7$ TeV could give rise to additional $t\bar{t}$ production mechanisms, not previously seen.

The Standard Model prediction for the $t\bar{t}$ cross-section in pp collisions at a centre of mass energy of $\sqrt{s} = 7$ TeV is calculated to be $\sigma_{t\bar{t}} = 164.6^{+11.4}_{-15.7}$ pb at approximate NNLO [70, 71].

As stated in Section 3.2 the top quark almost always decays in the mode $t \rightarrow Wb$, and the decays of the W bosons dictate the final topologies of the events. The semileptonic decay mode ($t\bar{t} \rightarrow bl\nu bjj$) is studied in this analysis and provides a good balance between the branching ratio[1] of 43.8% (which includes both e and μ channels) and the relatively low background [58]. The semileptonic channel will give rise to final event states with one lepton, missing transverse energy and jets, two of which will be b-flavoured.

This section aims to give an early measurement of the $t\bar{t}$ production cross-section with the ATLAS detector in the semileptonic channel, utilising soft muon tagging via χ^2_{match} to identify b flavour jets. Using soft muons to tag b-jets creates a complementary sample of $t\bar{t}$ events to that using displaced vertex tagging. The data sample using soft muon tagging is $\approx 20\%$ of that via displaced vertex tagging as a result of the branching fraction of b-hadron decay.

7.2 Data and Monte Carlo samples

7.2.1 Data samples

The collision data at a centre-of-mass energy of 7 TeV, collected between June 24th and August 29th 2010 are included in this analysis and cover ATLAS data taking periods "D" through to "F". Only the luminosity blocks that have been declared good are used in this analysis following the guidelines set out by the ATLAS top-quark working group; the criteria for a good luminosity block cover the state of the relevant ATLAS detector elements and that the LHC beam is stable.

---

[1] The quoted branching ratios also include small contributions from leptonically decaying taus.

The analysis code was run on a data sample provided by the ATLAS top-quark working group, this data sample is derived from the full data set and is required to pass a set of loose object selection cuts. The dataset is split into two separate channels defined by primary lepton used to trigger the event, this analysis used the "ElectronEvent" and "MuonEvent" channels (details of certain criteria listed in these definitions are described in Section 4.4.2 and Section 4.4.3).

ElectronEvent

Events containing at least one electron with

- Calorimeter cluster $E_T > 15$ GeV
- Author = 1 or 3
- "IsEM" = loose

or at least one electron with

- Calorimeter cluster $E_T > 15$ GeV
- $E_T^{cone20} < 4$ GeV

MuonEvent

Events containing at least one muon reconstructed with the STACO [47] or MuID [48] algorithm

- $p_T > 15$ GeV

Using the list of runs approved by the top-quark working group within ATLAS, that excludes any luminosity block that contains a prescaled trigger used in this analysis, gives a combined integrated luminosity of 2869.44 nb^{-1}, the details of which are shown in Table 7.1

7.2.2 Monte Carlo samples

This analysis method was developed with the help of simulated $t\bar{t}$ samples which were also used to calculate the acceptance of $t\bar{t}$ events in the ATLAS detector. The generation of $t\bar{t}$ signal events was done with the next-to-leading order (NLO) generator MC@NLO [38], with an assumed top-quark mass of 172.5 GeV.

Using approximate NNLO calculations [70, 71], the cross-section of the $t\bar{t}$ production is normalised to 164.6 pb. All hadronisation is performed using the HERWIG [34] and Jimmy [37] programs. All samples have been reconstructed using the standard ATLAS detector and trigger simulation [72] and are subject to the same reconstruction and analysis algorithms used in data.

7.3 Object selection

Reconstructing $t\bar{t}$ events makes use of all of the different parts of the ATLAS detector, in that electrons, muons, jets and the missing transverse energy E_T^{miss} (which is sensitive to the presence of neutrinos) are all reconstructed. For this analysis the following selection criteria are used, as required by the top-quark working group for comparison of results:

Electron

- $p_T > 20$ GeV

Period and ATLAS Run Numbers	Integrated Luminosity (nb^{-1})
D:158045-159224	278.46
E:160387-161948	1002.32
F:162347-162882	1588.66
Total	2869.44

Table 7.1: The recorded luminosity for the runs in periods D and F after removing the luminosity blocks that are flagged not usable for top quark physics analysis.

- “Egamma” Author = 1 or 3
- $|\eta| \leq 2.47$ except barrel/end-caps region $1.37 < |\eta| < 1.52$
- “IsEM” = RobusterTight
- Require at least 1 hit in the *b*-layer to suppress background from photon conversions
- E_T^{cone20} <C$_1$+C$_2 \cdot E_T$ [GeV], with C$_1$ = 4 GeV and C$_2$ = 0.023
- Additionally, all electron candidates are required to pass cuts that check the condition of the detector in the region the candidate is found in.

Muon

- $p_T > 20$ GeV
- $|\eta| < 2.5$
- Muon has a combined muon track.
- $p_T^{cone30} < 4$ GeV
- $E_T^{cone30} < 4$ GeV

The isolation criteria (E_T^{cone}) for both electrons and muons are described in Section 4.4.5, it uses cone sizes defined in Equation 2.2 to help reduce the background due to leptons from the decays of hadrons (including heavy flavours) produced within jets. The additional isolation requirement of p_T^{cone} is defined as the scalar sum of track transverse momenta in a cone minus the track momenta of the muon object itself.

As the instantaneous luminosity delivered by the LHC increased during the different run periods the trigger chains for electrons and muons evolved to ensure that at no point were pre-scaled triggers in use,

Egamma Trigger

- Data Period D - L1_EM10

- Data Period E - EF_g17_etcut
- Data Period F - EF_e10_medium

Muon Trigger

- Data Period A-E3 - L1_MU10
- Data Period E4-F - EF_mu10_MSonly

The electron trigger in use for period D, L1_EM10, is based solely on requiring an electromagnetic object passing a certain energy threshold in the EM calorimeter. From period E onwards the HLT uses calorimeter clusters that are seeded from L1 regions of interest and associated with tracks. The HLT uses the full granularity of the calorimeter and the fast calorimeter and track reconstruction algorithms.

The muon trigger for periods A-E3 relies on just the L1 trigger. The L1 muon triggers for this are the resistive plate chambers in the barrel region and thin-gap chambers in the end-cap and forward regions of ATLAS. The muon p_T cut is placed at 10 GeV. For the later periods the muon trigger evolved to using the EF level trigger, seeded by a L1_MU0 region of interest.

7.3.1 Jet Reconstruction

As described in more detail in Section 4.4.4 jets are reconstructed using the anti-k_t algorithm [73] with a cone size chosen as $\Delta R = 0.4$ from topological clusters [74] in the calorimeters. The jets are calibrated at the electromagnetic scale appropriate for the energy deposited by electrons or photons. The jets are further calibrated to the hadronic energy scale, using a correction factor obtained from simulation [74] which depends upon p_T and η. Finally jets are required to have $p_T > 25$ GeV.

7.3.2 Electron-Jet Overlap

An overlap removal between jets and electrons is necessary, if the closest object to an electron candidate that has passed all the selection criteria is a jet. This is because electrons can also be reconstructed as jets by the jet algorithms. If the separation between the electron candidate and the closest jet is $\Delta R < 0.2$, the jet is removed in order to avoid double-counting of electrons as jets. It is also possible that a real jet is found near the electron, in which case the jet algorithm merges the jet cluster with the electron cluster. The effect of double counting the electron energy in nearby jets can be seen in Figure 7.1b, which shows the average E_T of jets as a function of ΔR from W-electrons. When the jet and electron from the decay of the top quark are heavily boosted, the jet reconstruction algorithm includes both the jet energy and electron energy in one object.

With a jet cone size of 0.4 there still exists the possibility of including nearby electron energy in the jet reconstruction. Figure 7.1a shows a number of jets with axis close to a true electron from W decay, but this effect in top quark events is estimated to affect only about 1% of the events.

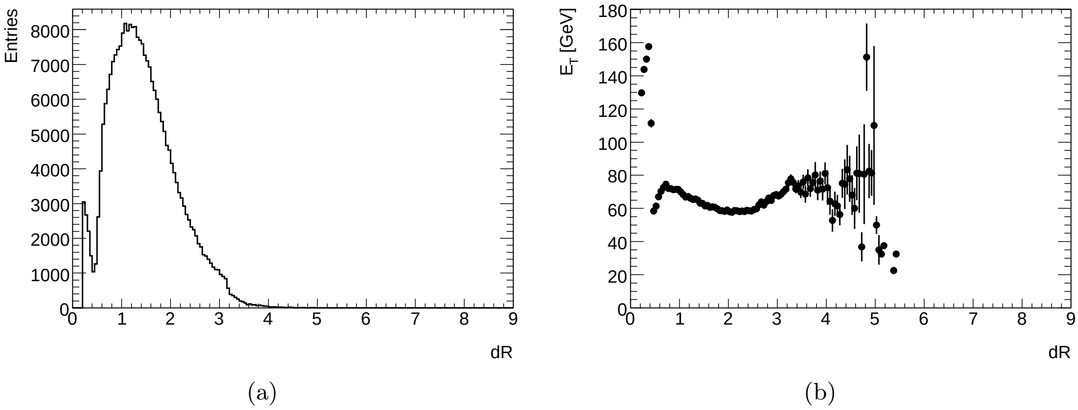

(a) (b)

Figure 7.1: Distance in ΔR space between W-electrons matched to truth and the closest nearby jet (a) and the average E_T of these jets as a function of ΔR space (b).

7.3.3 *b*-Jet Tagging

The tagging of *b*-jets is done via the χ^2_{match} variable associated to muons that are within $\Delta R < 0.5$ of a jet. The χ^2_{match} variable is described in Section 4.4.3 and has been shown to have an average efficiency $\approx 86.\%$ in tagging muons in J/ψ data (Section 6.8.3) when selecting muons with $\chi^2_{match} < 3.2$.

7.3.4 Missing transverse energy

Missing transverse energy is constructed from the vector sum of all calorimeter cells contained within the topological clusters in an object-based approach. Calorimeter cells are associated to a parent object in the chosen order of electron, jets, muons such that no cell is counted twice [75]. Energy corrections are calibrated for the cells in respect to which object they were associated to: electron objects are calibrated at the electron energy scale and cells associated to jets are calibrated at the corrected energy scale for jets. Lastly the contribution from muons is included after adjusting for the muon contribution to calorimeter energy deposits.

7.4 Event selection

The semileptonic $t\bar{t}$ final state is characterised by an isolated lepton with relatively high p_T and missing energy corresponding to the neutrino from the leptonic decay of the W boson, along with two b quark jets and two light jets from the hadronic decay of the W.

Following the requirements set out in Section 7.3 on the reconstructed objects the semileptonic analysis also requires selection criteria on the event topology as set out below:

- The firing of the single-electron or single-muon trigger for the appropriate data period;

- The event contains exactly one and only one reconstructed lepton passing the quality criteria set out in Section 7.3;
- $E_T^{miss} > 20$ GeV, (rejects a significant fraction of the QCD background);
- $E_T^{miss} + m_T(W) > 60$ GeV ([2]). Further rejection of QCD events is achieved by applying a cut in the $(E_T^{miss}, m_T(W))$ plane: true $W \to \ell\nu$ decays have a large E_T^{miss} and also a large $m_T(W)$. QCD events can also occur with a large E_T^{miss} but typically small $m_T(W)$. The above two requirements discriminate between the two cases.
- 1 $\geq$Njets$\geq$4 jets with $p_T > 25$ GeV and with $|\eta| < 2.5$.

The events are labelled depending on the number of jets and whether or not at least one jet passes the *b*-tagging requirement. The Njet $\geq$ 4 sample with at least one *b*-jet tag is used as the signal region and the other samples are used for the determination of backgrounds.

As seen in Tables 7.2, 7.4 for electron and muon channels respectively, the pre-tag background is dominated by W+jets events, which have the same signature as $t\bar{t}$ signal events at this point in the event selection. There is also a large contribution from multijet events produced by strong interactions that do not contain either isolated leptons nor E_T^{miss}, however they are present in the selected samples due to the imperfect reconstruction of these objects in the detector.

Tables 7.3, 7.5 show the event selection after the *b*-tagging requirement for the electron and muon channels respectively. The background in the muon channel is still dominated by W+jets events but in the electron channel the background from multijet events is similar in number to that from W+jets events.

---

[2] The W transverse mass $m_T(W)$ is defined as $\sqrt{2p_T^\ell p_T^\nu[1 - cos(\phi^\ell - \phi^\nu)]}$ where the measured E_T^{miss} vector provides the neutrino information.

e+jets channel				
	1-jet pre-tag	2-jet pre-tag	3-jet pre-tag	$\geq$4-jet pre-tag
QCD (DD)	464 ± 81	157 ± 36	55 ± 21	22 ± 11
W+jets (DD)	1592 ± 93	252 ± 42	54 ± 24	15 ± 5
Total (non-$t\bar{t}$)	2056 ± 124	409 ± 55	109 ± 32	37 ± 12
$t\bar{t}$ (MC)	1.6 ± 0.3	5.9 ± 1.2	9.5 ± 1.9	13.7 ± 2.7
Total expected	−−	−−	119 ± 32	51 ± 12
Observed	2058	415	119	57

Table 7.2: Number of events before b-tagging with different jet multiplicities in the single-electron channel. The observed number of events are shown, together with the Monte Carlo simulations estimates for $t\bar{t}$ signal events, normalised to the data integrated luminosity of 2.9 pb^{-1}. The data-driven estimates (DD) for QCD multijet and W+jets backgrounds are also shown. The uncertainties on QCD data-driven background estimates include the statistical and all systematic uncertainties, the W+jets only include systematics on the 4-jet column. The 1-jet and 2-jet bins are normalised to the number of observed events and used in extrapolating backgrounds in the 3 and 4 jet bins, therefore there is no expectation in the 1-jet and 2-jet bins.

e+jets channel				
	1-jet tagged	2-jet tagged	3-jet tagged	$\geq$4-jet tagged
QCD (DD)	4.2 ± 1.2	1.5 ± 0.4	1.4 ± 0.8	1.4 ± 1.0
W+jets (DD)	5.3 ± 6.5	1.7 ± 2.1	0.5 ± 1.1	0.2 ± 0.3
Total (non-$t\bar{t}$)	9.5 ± 6.6	3.2 ± 2.1	1.9 ± 1.4	1.6 ± 1.0
$t\bar{t}$ (MC)	0.2 ± 0.04	0.9 ± 0.2	1.6 ± 0.3	2.6 ± 0.5
Total expected	10 ± 7	−−	4 ± 1	4 ± 1
Observed	10	4	2	5

Table 7.3: Number of tagged events with different jet multiplicities in the single-electron channel. The observed number of events are shown, together with the Monte Carlo simulations estimates for $t\bar{t}$ signal events, normalised to the data integrated luminosity of 2.9 pb^{-1}. The data-driven estimates (DD) for QCD multijet and W+jets backgrounds are also shown. The uncertainties on QCD data-driven background estimates include the statistical and all systematic uncertainties, the W+jets only include systematics on the 4-jet column. The 2-jet bin is normalised to the number of observed events and used in extrapolating backgrounds, therefore there is no expectation in the 2-jet bin.

μ+jets channel				
	1-jet pre-tag	2-jet pre-tag	3-jet pre-tag	$\geq$4-jet pre-tag
QCD (DD)	412 ± 44	100 ± 20	33 ± 15	6 ± 3
W+jets (DD)	1223 ± 56	261 ± 25	55 ± 17	15 ± 3
Total (non-$t\bar{t}$)	1635 ± 72	361 ± 32	89 ± 23	21 ± 4
$t\bar{t}$ (MC)	1.5 ± 0.3	6.2 ± 1.2	11.5 ± 2.3	18.2 ± 3.7
Total expected	−−	−−	100 ± 23	40 ± 6
Observed	1637	367	97	51

Table 7.4: Number of events before b-tagging with different jet multiplicities in the single-muon channel. The observed number of events are shown, together with the Monte Carlo simulations estimates for $t\bar{t}$ signal events, normalised to the data integrated luminosity of 2.9 pb^{-1}. The data-driven estimates (DD) for QCD multijet and W+jets backgrounds are also shown. The uncertainties on QCD data-driven background estimates include the statistical and all systematic uncertainties, the W+jets only include systematics on the 4-jet column. The 1-jet and 2-jet bins are normalised to the number of observed events and used in extrapolating backgrounds in the 3 and 4 jet bins, therefore there is no expectation in the 1-jet and 2-jet bins.

μ+jets channel				
	1-jet tagged	2-jet tagged	3-jet tagged	$\geq$4-jet tagged
QCD (DD)	9.2 ± 3.6	3.3 ± 0.8	2.2 ± 0.9	0.4 ± 0.2
W+jets (DD)	20.7 ± 7.5	8.8 ± 2.9	2.6 ± 1.0	1.0 ± 0.5
Total (non-$t\bar{t}$)	29.8 ± 8.3	12.1 ± 3.0	4.8 ± 1.3	1.4 ± 0.5
$t\bar{t}$ (MC)	0.1 ± 0.02	0.9 ± 0.1	2.0 ± 0.1	3.7 ± 0.8
Total expected	30 ± 8	−−	7 ± 1	5 ± 1
Observed	16	13	5	8

Table 7.5: Number of tagged events with different jet multiplicities in the single-muon channel. The observed number of events are shown, together with the Monte Carlo simulations estimates for $t\bar{t}$ signal events, normalised to the data integrated luminosity of 2.9 pb^{-1}. The data-driven estimates (DD) for QCD multijet and W+jets backgrounds are also shown. The uncertainties on QCD data-driven background estimates include the statistical and all systematic uncertainties, the W+jets only include systematics on the 4-jet column. The 2-jet bin is normalised to the number of observed events and used in extrapolating backgrounds, therefore there is no expectation in the 2-jet bin.

7.5 QCD Background Determination

QCD multijet processes form a large fraction of the backgrounds to $t\bar{t}$ events and involve events that have some E_T^{miss} and an identified lepton which does not come from a real W decay. The lepton can be real, coming from light-flavour decays or from the semi-leptonic decay of a B hadron. The signal lepton can also be faked in numerous ways, such as:

- Decay-in-flight of a $\pi^{\pm}$ or K meson,
- Reconstruction of a π^0 as an electron,
- Reconstruction of an electron from a photon conversion.

QCD events do not in general have large E_T^{miss} in comparison to $t\bar{t}$ events, however when jets occur in the gaps in the detector or there are incorrect jet energy measurements a large E_T^{miss} can be formed for the event.

7.5.1 QCD background estimate in the μ+jets channel

To estimate the background in the μ+jet channel the "ABCD method" was used. This relies on the assumption that the QCD event distribution can be factorised in a (x, y) plane, where x and y are two uncorrelated variables. In this case we have chosen y to be lepton isolation in the form of E_T^{cone30} or p_T^{cone30}, and x to be E_T^{miss}. Figure 7.2 illustrates the different regions used in the ABCD method; they represent the following quadrants:

- **A**: non-isolated lepton, low E_T^{miss}
- **B**: isolated lepton, low E_T^{miss}
- **C**: non-isolated lepton, high E_T^{miss}
- **D**: isolated lepton, high E_T^{miss} (signal region)

Assuming we can neglect the signal contribution in regions A and B, and assuming that E_T^{cone30} and E_T^{miss} are uncorrelated, the number of QCD events in the signal region, D, can be evaluated as $N_D = N_B \times \frac{N_C}{N_A}$ and its relative statistical error as:

$$\frac{\Delta N_D}{N_D} = \sqrt{\left(\frac{N_C}{N_A}\Delta N_B\right)^2 + \left(\frac{N_B}{N_A}\Delta N_C\right)^2 + \left(\frac{N_B N_C}{N_A^2}\Delta N_A\right)^2} \tag{7.1}$$

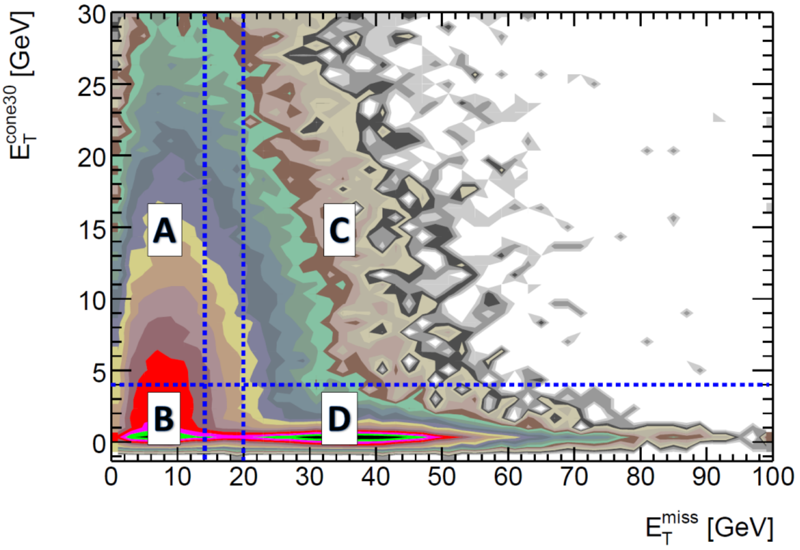

Figure 7.2: Separation of the isolation (E_T^{cone30}) vs E_T^{miss} plane into signal region (D), control region (B) and the background dominated regions (A,C) from data.

where ΔN are the statistical uncertainties.

Figures 7.3a, 7.3b show the E_T^{cone30} vs E_T^{miss} plane in the 2-jet bin before and after b-tagging respectively. Figures 7.3c, 7.3d show the E_T^{cone30} vs E_T^{miss} plane in the 4-jet signal bin, before and after b-tagging respectively.

The systematics using the ABCD method were investigated by looking at the difference in the predicted background contributions between using E_T^{cone30} and p_T^{cone30} as the isolation variables.

The final predictions of the QCD background in the μ+jets channel uses the average value returned between using E_T^{cone30} and p_T^{cone30} as the isolation variable in the ABCD

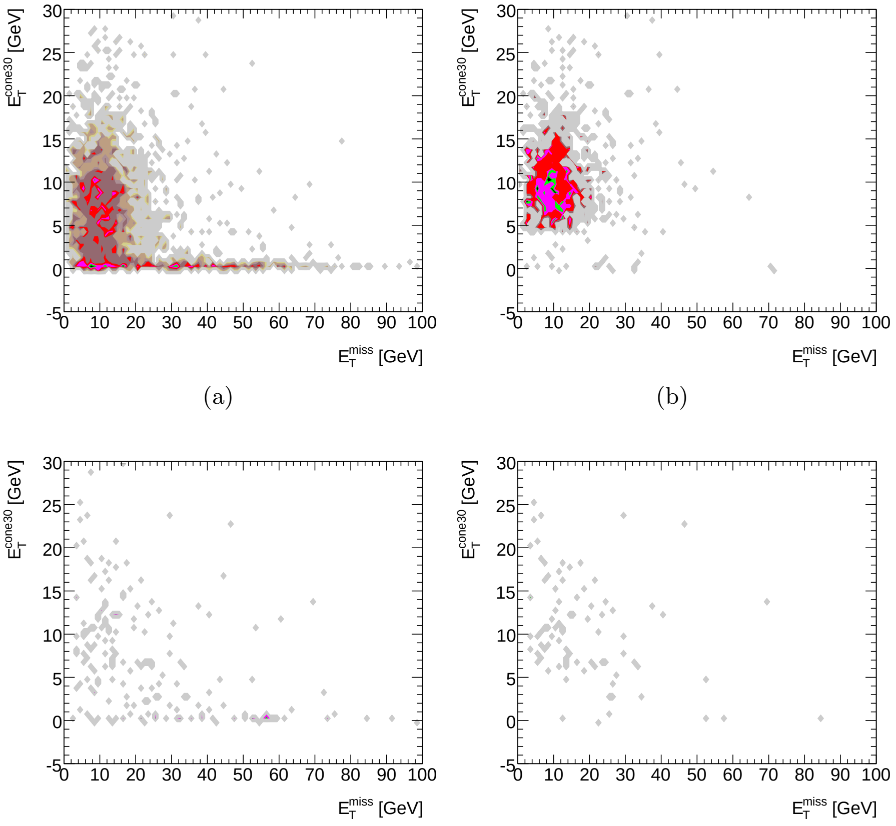

(a)

(b)

(c)

(d)

Figure 7.3: E_T^{cone30} vs E_T^{miss} plane used in the ABCD method for the muon channel, for the 2-jet sample: pre-tag (a) and *b*-tagged (b). Signal region for the 4-jet sample is shown in: pre-tag (c) and tagged (d) from data.

method. This gives a systematic uncertainty ranging from 11% through to 68% depending on jet multiplicity after b-tagging has been applied. Table 7.6 shows the predictions on QCD events in the μ+jets channel.

Number of jets	1	2	3	≥4
pre-tag (E_T^{cone30})	431.9 ± 32.1	91.3 ± 8.2	26.6 ± 4.5	7.5 ± 2.4
pre-tag (p_T^{cone30})	392.7 ± 24.9	109.1 ± 13.6	40.2 ± 10.0	5.0 ± 2.4
Tagged (E_T^{cone30})	10.7 ± 2.1	3.6 ± 0.8	2.1 ± 0.8	0.5 ± 0.5
Tagged (p_T^{cone30})	7.6 ± 3.0	3.1 ± 1.2	2.3 ± 1.5	0.3 ± 0.4

Table 7.6: Number of predicted QCD events in 2.9 pb^{-1} of data for a given number of jets, using either the muon E_T^{cone30} or p_T^{cone30} in the ABCD method, μ+jets channel. Only statistical uncertainties on the quadrant calculations are shown.

7.5.2 QCD background estimate in the e+jets channel

In the e+jets channel we did investigate the use of the ABCD method but found that the IsEM cut definition produced a jump in the isolation variable, as shown in Figure 7.4. This meant that the use of the ABCD method, as used in the μ+jets channel, would not be appropriate in estimating the QCD background in the e+jets channel. Time constraints meant that the we were unable to fully investigate a solution to this jump in isolation energy at $\approx$ 5 GeV, but the cause was likely to be related to the electron-jet overlap removal. In cases where the candidate electron has passed all cuts except the isolation requirement, the overlap removal of nearby jets, defined in Section 7.3.2, is not performed on these non-isolated electrons. There are in general many more 2-jet than 3-jet events and due to the electron-jet overlap not being performed on non-isolated electron candidates, they are then counted as jets. Therefore a 2-jet event will become a 3-jet event along with a migration of energy at the isolation cut point.

Therefore to estimate the QCD background in the e+jets channel we used a different, but just as suitable method involving the use of an “anti-electron” sample. This method is based around extrapolating the QCD contribution from low to high E_T^{miss} region, with the QCD contribution being modelled using an “anti-electron” sample.

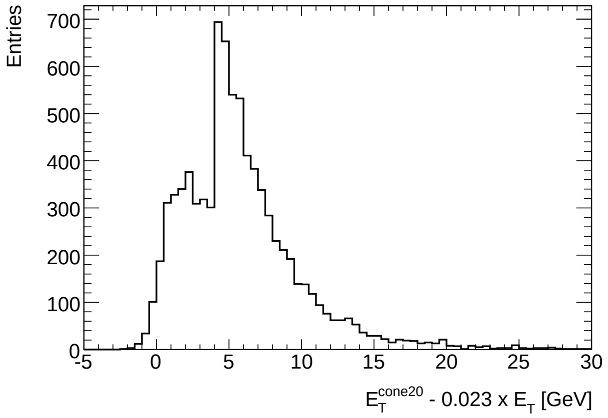

Figure 7.4: The distribution of the isolation variable $E_T^{cone20} - 0.023 \cdot E_T$ [GeV] for candidates passing the IsEM = RobusterTight definition.

The standard electron selection defined in Section 7.3 is followed apart from the IsEM = RobusterTight definition. Objects that fail the IsEM definition are defined as "anti-electrons" and all those that pass are defined as good electrons. Both the "anti-electron" sample and good-electron sample are required to pass all other selection criteria.

The anti-electron sample will mostly consist of the QCD background to the signal $t\bar{t}$ e+jets sample with the E_T^{miss} shape being used to model the QCD background in the signal region. Figure 7.5 shows the low E_T^{miss} region in which the anti-electron sample is scaled to the good-electron sample. The scale factor is then used to extrapolate into the QCD events into $E_T^{miss} > 20$ GeV signal region and will give the expected number of QCD background events; this process is done in all jet bins up to Njet ≥ 4. Table 7.7 details the number of predicted QCD events using the anti-electron model before and after b-tagging has been applied.

Number of jets	1	2	3	≥4
pre-tag anti-electron	464.1 ± 11.3	156.6 ± 7.1	55.3 ± 5.0	22.5 ± 2.0
Tagged anti-electron	4.2 ± 1.0	1.5 ± 0.3	1.4 ± 0.3	1.4 ± 0.4

Table 7.7: Number of predicted QCD events in 2.9 pb^{-1} of data for a given number of jets for the anti-electron model in the e+jets channel. Only statistical uncertainties on the calculations are shown.

Systematics using this method were not investigated, but the anti-electron method has

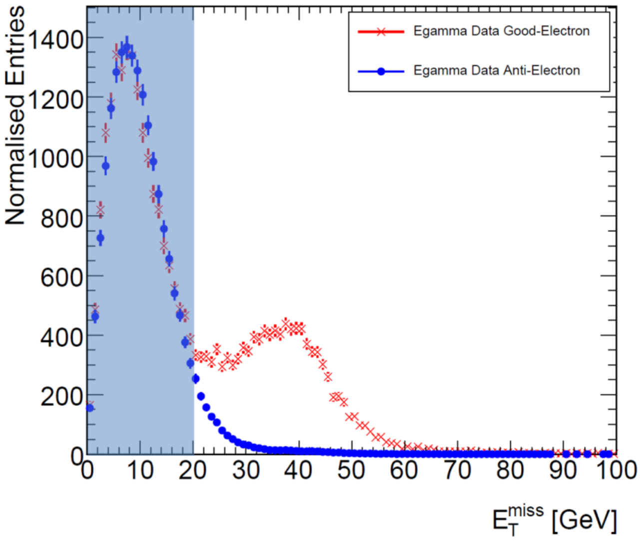

Figure 7.5: The anti-electron method, the low-E_T^{miss} region is scaled to the lepton+jets data using the E_T^{miss} shape from the anti-electron sample.

been studied in detail in [76] for the same data periods used in this analysis and the systematic uncertainties of this method, ranging from 16% to 66% depending on jet multiplicity and b-tagging requirement, are included here. Systematics were determined by using two different fake lepton samples, one being the anti-electron definition used in this analysis and the other an anti-jet sample. The anti-jet sample follows the standard jet selection criteria defined in Section 7.3 but requires that the jet has an electromagnetic energy fraction of between 0.8 and 0.95 and at least four associated tracks.

7.6 W+jets Background Determination

This section details the techniques used to determine the W+jets background in the $t\bar{t}$ channel measured in this analysis. A series of measurements are made on a control sample of W events with low jet multiplicity to determine the background into the top quark signal region where there is higher jet multiplicity. The production of W-bosons in association with jets is one of dominant sources of background to top-quark pair production in the single lepton plus jets channel.

7.6.1 W+jets Background Determination in the pretag sample

The ratio of $W + n + 1$ jets to $W + n$ jets production is expected to be approximately constant as a function of n, via the so-called Berends-Giele scaling, [77, 78] and therefore the number of W events with at least 4 selected jets, before b-jet tagging, can be obtained as:

$$W^{\geq 4jets} = W^{2jets} \cdot \sum_{i=2}^{\infty} (W^{2jets}/W^{1jet})^i \tag{7.2}$$

Equation 7.2 thus gives the rate of W production with at least 4 jets before the b-tagging requirement has been made. This method is applied to both the electron and muon channels.

The $W + 1, 2$ jet event candidates are selected from data using the same event criteria as the full $t\bar{t}$ signal selection, (Section 7.4). This includes:

- Single lepton trigger,
- Exactly one reconstructed lepton,
- $E_T^{miss} > 20$ GeV,
- $E_T^{miss} + m_T(W) > 60$ GeV,
- One or two jets with $p_T > 25$ GeV and $|\eta| < 2.5$.

The data samples are split into 1 or 2 jet bins. We first remove from the number of events the data driven estimates of QCD and the expected $t\bar{t}$ from Monte Carlo, as shown in Table 7.8. The uncertainty on the W+jet rates encompass the uncertainties derived from the data-driven QCD estimates and the contribution from $t\bar{t}$ Monte Carlo.

The ratio between the 2-jet and 1-jet events is found to be 0.21 ± 0.014 (stat.) ±

0.018 (syst.) for the muon channel and 0.16 ± 0.014 (stat.) ± 0.024 (syst.) for the electron channel, where the first uncertainty is statistical and the second derived from systematics on background predictions. The larger fraction of QCD events in the electron channel (due to QCD jets faking an isolated electron signature) makes the measurement in this channel of poorer precision in relation to that of the muon channel. Since it is expected that the ratio between the 2 jet and 1 jet rates is independent of W decay mode, the muon channel estimate can also be used for the electron channel. Therefore the number of W events with at least 4 selected jets before b-tagging in the electron channel is obtained as:

$$We\nu^{\geq 4jets} = We\nu^{2jets} \cdot \sum_{i=2}^{\infty} (W\mu\nu^{2jets}/W\mu\nu^{1jet})^i \tag{7.3}$$

In the electron channel the number of predicted events in the 4 jet pre-tag sample is 51 ± 12 and we observe 57 data. Using the data driven methods to estimate the QCD multijet and W+jet in the 1-and 2-jet bins and extrapolating to the 4-jet bin shows good agreement. In the muon channel the predicted number of events in the 4-jet pre-tag sample is 40 ± 6 with the number of observed in data as 51. This shows a slight discrepancy beyond the uncertainties calculated for the QCD multijet, W+jet and $t\bar{t}$ Monte Carlo.

The number of W events in the 3-jet bin is defined in Equation 7.4, using the ratio between the 2-jet and 1-jet rates in the muon channel for extrapolation in both channels.

Process	$W \to e\nu$+1jet	$W \to e\nu$+2jet	$W \to \mu\nu$+1jet	$W \to \mu\nu$+2jet
Candidates	2058	415	1637	367
QCD	464 ± 81	157 ± 36	412 ± 44	100 ± 20
$t\bar{t}$	1.6 ± 0.3	5.9 ± 1.2	1.5 ± 0.3	6.2 ± 1.2
Observed $W(l\nu)$	1592 ± 93	253 ± 42	1223 ± 56	261 ± 25

Table 7.8: Number of selected data events in $W \to l\nu + 1$ jet and $W \to l\nu + 2$ jets sample from data.

$$We\nu^{3jets} = We\nu^{2jets} \cdot (W\mu\nu^{2jets}/W\mu\nu^{1jet}) \tag{7.4}$$

In the electron channel the prediction in the 3-jet channel of 119 ± 32 and the observed in data of 119 are in perfect agreement, notwithstanding the 27% uncertainty on the prediction. In the muon channel the pre-tag prediction of 100 ± 23 and the observed of 97 in data are in agreement within the uncertainties. Full details for the electron and muon channels can be seen in Tables 7.2, 7.4 respectively.

7.6.2 W+jets Background Determination in the tagged sample

The W+jets background estimate after b-tagging has been preformed is constructed in the following way,

$$W^{tagged-\geq 4jets} = W^{pretag-\geq 4jets} \cdot f^{\geq 4jets}_{tagged} \tag{7.5}$$

The value of $W^{pretag-\geq 4jets}$ is the extrapolation described in the previous section and $f^{\geq 4jets}_{tagged}$ is the fraction of these events that will be tagged with a b-jet, calculated as,

$$f^{\geq 4jets}_{tagged} = f^{2jets}_{tagged} \cdot f^{corr}_{2\to\geq 4} \tag{7.6}$$

The value of f^{2jets}_{tagged} is a measurement taken in the 2-jet channel of the fraction of jets tagged as being a b-jet, which is calculated to be $(0.7 \pm 0.8)\%$ in the electron channel and $(3.4 \pm 1.1)\%$ in the muon channel. Tables 7.9 and 7.10 show the number of W+jet events before and after b-tagging was applied for the electron and muon channels that go into calculation of f^{2jets}_{tagged}. The correction factor, $f^{corr}_{2\to\geq 4}$ accounts for the different event tagging probability between the 2-jet and 4-jet samples [75].

The value of $f^{corr}_{2\to\geq 4}$ is naively taken to be 2.0±0.8, purely from the scaling of the number of jets. The value of $f^{corr}_{2\rightarrow\geq4}$ has been calculated with b-tagging using a secondary vertex-based tagging algorithm to be 2.8 ± 0.8, the details of which can be found in [79]. This is a different tagging algorithm to the one used in this analysis (χ^2_{match}) and it is very likely background for the secondary vertex tagger will scale with factorial of the number tracks, whereas the χ^2_{match} is more likely to be linear. Unfortunately there was not enough time to investigate this via Monte Carlo simulations and we take the linear scaling value of 2.0 ± 0.8 with the uncertainty taken from the secondary vertex algorithm.

For the 1-jet and 3-jet samples there does not exist a correction factor that can be referenced, but to first order effects it can be estimated simply from knowing f^{2jets}_{tagged} and that it represents the probability to tag at least one of the two jets. This equates to the 1-jet tag rate being $\approx 0.5 \cdot f^{2jets}_{tagged}$ and the 3-jet tag rate being $\approx 1.5 \cdot f^{2jets}_{tagged}$. These rates are based on the tagging probability per event and not per jet. Table 7.9 details the expected W+jet contributions in data for both the electron and muon channels.

Number of jets	1	2	3	≥4
W+jets pre-tag ($\mu\nu$)	1223.0 ± 56.3	260.6 ± 25.1	55.5 ± 17.1	15.0 ± 3.2
W+jets pre-tag ($e\nu$)	1592.3 ± 93.4	252.5 ± 42.1	53.8 ± 24.2	14.6 ± 5.2

Table 7.9: Number of W+jet events in 2.9 pb^{-1} of data for a given number of jets for e+jets and μ+jets channels before b-tagging has been applied. The 1 and 2 jet bins are derived from data, the 3 and ≥4 jet bins are extrapolations of the 1 and 2 jet bins.

Number of jets	1	2	3	≥4
W+jets tagged ($\mu\nu$)	20.7 ± 7.5	8.8 ± 2.6	1.0 ± 1.0	1.0 ± 0.5
W+jets tagged ($e\nu$)	5.3 ± 6.5	1.7 ± 2.1	0.5 ± 1.1	0.2 ± 0.3

Table 7.10: Number of W+jet events in 2.9 pb^{-1} of data for a given number of jets for e+jets and μ+jets channels after b-tagging has been applied. The 1, 3 and ≥4 jet bins are predictions based off the observed 2 jet events.

In the electron channel the prediction in the 3-jet tagged bin is 4 ± 1 with 2 observed in data. In the 4-jet tagged bin the predicted number of event is 4 ± 1 and we observe

5 events in data. With these low statistics and a 25% uncertainty on the prediction it is hard to come to any firm conclusions, however there does not appear to be any large discrepancies with the limited events available.

In the muon channel the prediction in the 3-jet tagged bin is 7 ± 1 with 5 observed in data. In the 4-jet tagged bin the predicted number of events is 6 ± 1 and we observe 8 events in data. As with the electron channel, the number of events is low after b-tagging has been applied in the muon channel and therefore there does not appear to be any large discrepancies beyond the predicted number of events.

One area that should be further investigated is the contribution from other background processes, such as Z+jets, single top-quark and diboson processes. However in both pre-tagged and tagged samples QCD and W+jets are expected to account for $\approx$ 95% of all backgrounds for $t\bar{t}$ [75] and the already large statistical uncertainties the remaining 5% was not investigated for this analysis.

7.7 Determination of the cross-section

The cross-section for semileptonic $t\bar{t}$ production can be determined by counting all the events that pass the final selection (N_{obs}) and subtracting the number of estimated background events (N_{bkg}), and is given by the equation:

$$\sigma_{t\bar{t}} = \frac{N_{obs} - N_{bkg}}{\varepsilon \times \mathcal{L} \times \mathcal{BR}}, \tag{7.7}$$

where $\mathcal{L}$ is the integrated luminosity of the data sample, (2.9 pb^{-1}), and $\mathcal{BR}$ is the branching ratio of the selected semi-leptonic decays in the e/μ final state, derived from Monte Carlo simulation as 43.8% [58]. The efficiency ε includes the geometrical acceptance, trigger efficiency and the event selection efficiency and is calculated from $t\bar{t}$ Monte Carlo, giving a value of 3.2% for the combined $(e+\mu)$+jets channel. Included in the selection efficiency is the χ^2_{match} data over Monte Carlo scale factor (98.9% ± 1%) calculated from data in Section 6.2.

The measured values for the total $t\bar{t}$ cross-section derived from the electron and muon channels, including all statistical and systematic uncertainties are shown in Table 7.11.

Channel	Cross Section [pb]	Statistical Uncertainty [pb]	Systematic Uncertainty [pb]	Luminosity Uncertainty [pb]
e+jets	186	± 125	± 74	± 24
μ+jets	293	± 127	± 88	± 38
e or μ +jets	245	± 90	± 60	± 32

Table 7.11: Estimated total $t\bar{t}$ cross section using the counting method, showing separately the results derived from the e+jets, μ+jets and the combined channels separately.

The jet multiplicity distributions for the electron channel before and after b-tagging are shown in Figures 7.6a and 7.6b respectively and shows agreement within measured uncertainties to the predicted number of events in each jet bin.

The muon channel jet multiplicity distributions before and after b-tagging are shown in Figures 7.6c and 7.6d respectively. There is a deficiency is the number of observed events compared to the prediction in the 1-jet bin, but in all other bins there is agreement within the uncertainties.

The combination of the electron and muon channel jet multiplicity distributions is shown in Figures 7.6e and 7.6f. Figure 7.6e shows the distribution before b-tagging and Figure 7.6f shows the distribution after b-tagging. There is agreement in all jet multiplicity bins within the measured uncertainties between the number of observed and predicted events.

The data distributions were compared to the sum of all the expected contributions from Monte Carlo simulations ($t\bar{t}$) and background estimations using data-driven techniques for the selected lepton (e or μ) p_T, E_T^{miss} and the tagged soft muon p_T from b-hadron decay.

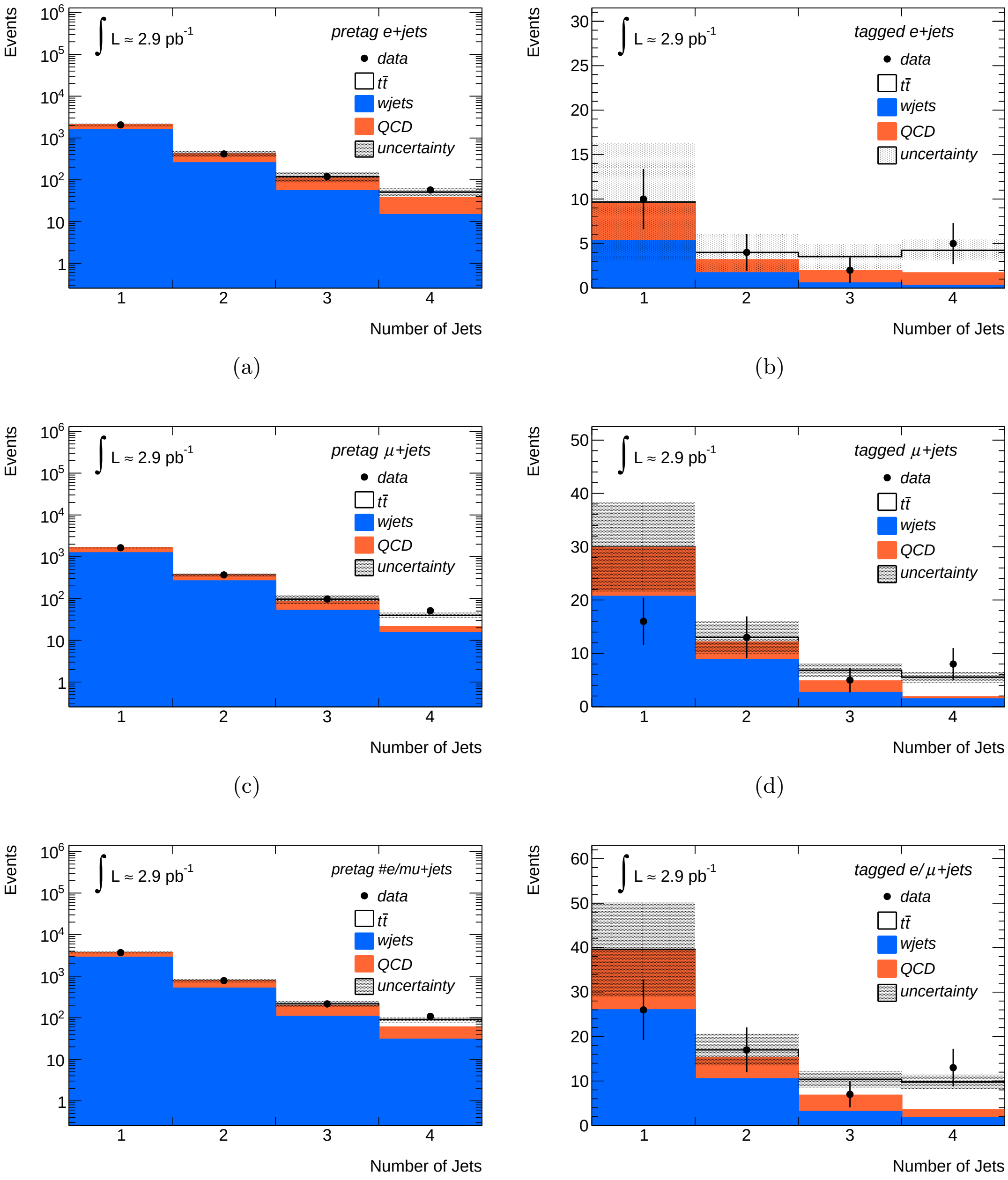

(a) (b)

(c) (d)

(e) (f)

Figure 7.6: Jet multiplicity distributions for pre-tag samples: electron channel (a), muon channel (c) and e/μ combined channel (e). Tagged sample distributions for: electron channel (b), muon channel (d) and e/μ combined channel (f).

The QCD and W+jets distributions were extrapolated from the tagged, W+1jet distributions and normalised to the data-driven estimates in the $\geq$ 4-jet bin from Tables 7.3 and 7.5. The W+1jet distributions are made up almost entirely of QCD multijet and W+jet contributions as shown in Tables 7.3 and 7.5.

Figures 7.7a and 7.7b show the lepton (e and μ respectively) p_T for all tagged events with four or more jets with the contributions from $t\bar{t}$ Monte Carlo and data-driven estimates on the QCD multijet and W+jets backgrounds. Figure 7.7c shows the combined e and μ p_T for all tagged events with four or more jets.

Figures 7.8a and 7.8b show the E_T^{miss} for the electron and muon channels for all tagged events with four or more jets with the contributions from $t\bar{t}$ Monte Carlo and data-driven estimates on the QCD multijet and W+jets background. Figure 7.8c shows the combined E_T^{miss} for all tagged events with four or more jets.

The soft muon p_T from the decay of the b-hadron decay is shown in Figure 7.9a for the electron channel and in Figure 7.9b for the muon channel. Figure 7.9b shows the combination of the electron and muon channel soft muon p_T.

7.8 Additional systematic uncertainties

The uncertainties that arise from the Monte Carlo simulation modelling of the lepton trigger, reconstruction and selection efficiencies have been calculated using tag and probe techniques on $Z \to ee$ and $Z \to \mu\mu$ events selected from the same data sample as used for the $t\bar{t}$ analysis [80]. The electron trigger, reconstruction and identification efficiencies in simulation were found to be in agreement with data to within the $\pm 2.3\%$ statistical uncertainties. For the muon reconstruction and identification, the efficiencies measured in data are consistent with simulation within the $\pm 1.2\%$ statistical uncertainty. However there is still a few percent discrepancy in the trigger efficiency that is accounted for by using efficiency scale factors in simulation.

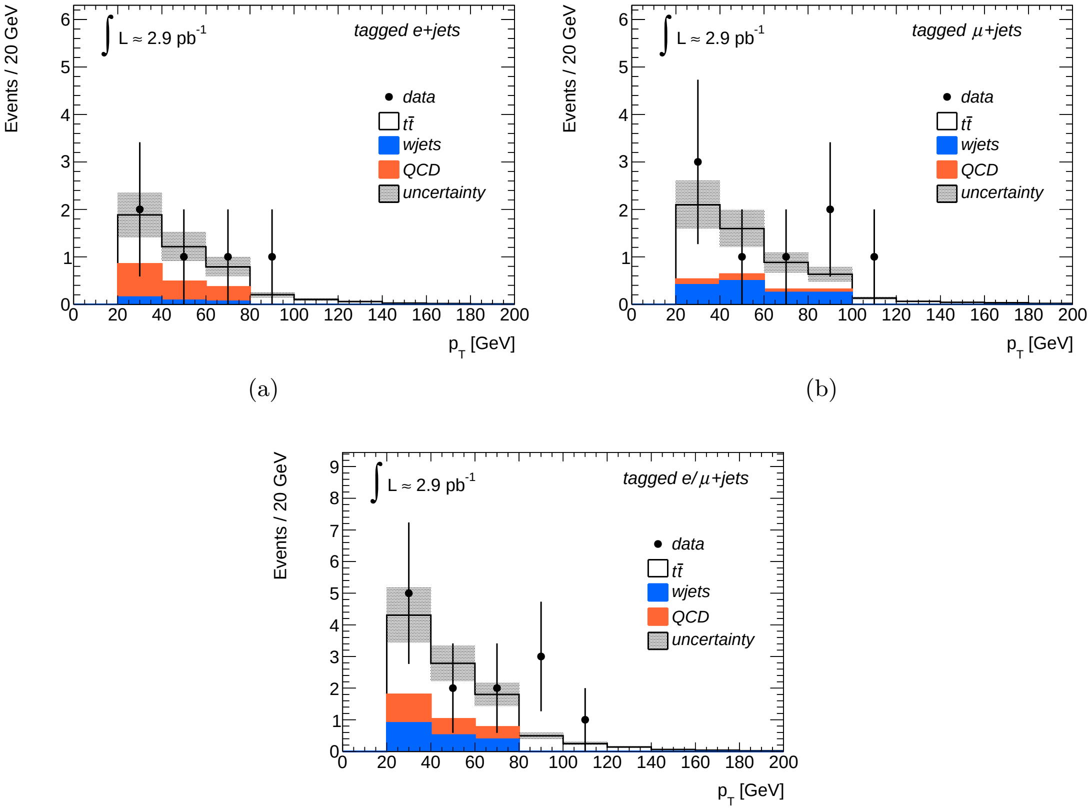

(a)

(b)

(c)

Figure 7.7: Distributions showing the lepton (e or μ) p_T after full selection criteria, including b-jet tagging, in the electron (a), muon (b) and combining the two channels (c) for events with four or more jets. The data are shown by the points with error bars, compared to the sum of all expected contributions, taken from simulations ($t\bar{t}$) or estimated using a data-driven technique (QCD multijet and W+jets). The hatched area shows the uncertainty on the total expectation due to the uncertainty on the expected contributions.

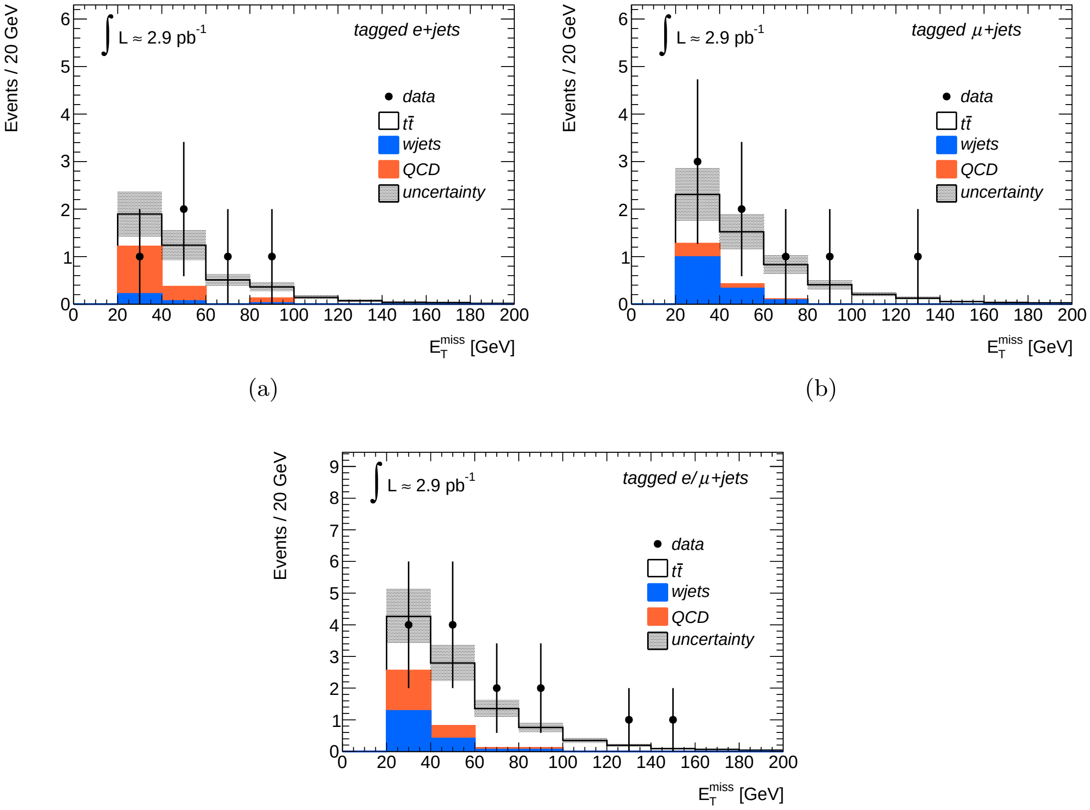

(a) (b)

(c)

Figure 7.8: Distributions showing E_T^{miss} after full selection criteria, including b-jet tagging, in the electron (a), muon (b) and combining the two channels (c) for events with four or more jets. The data are shown by the points with error bars, compared to the sum of all expected contributions, taken from simulations ($t\bar{t}$) or estimated using a data-driven technique (QCD multijet and W+jets). The hatched area shows the uncertainty on the total expectation due to the uncertainty on the expected contributions.

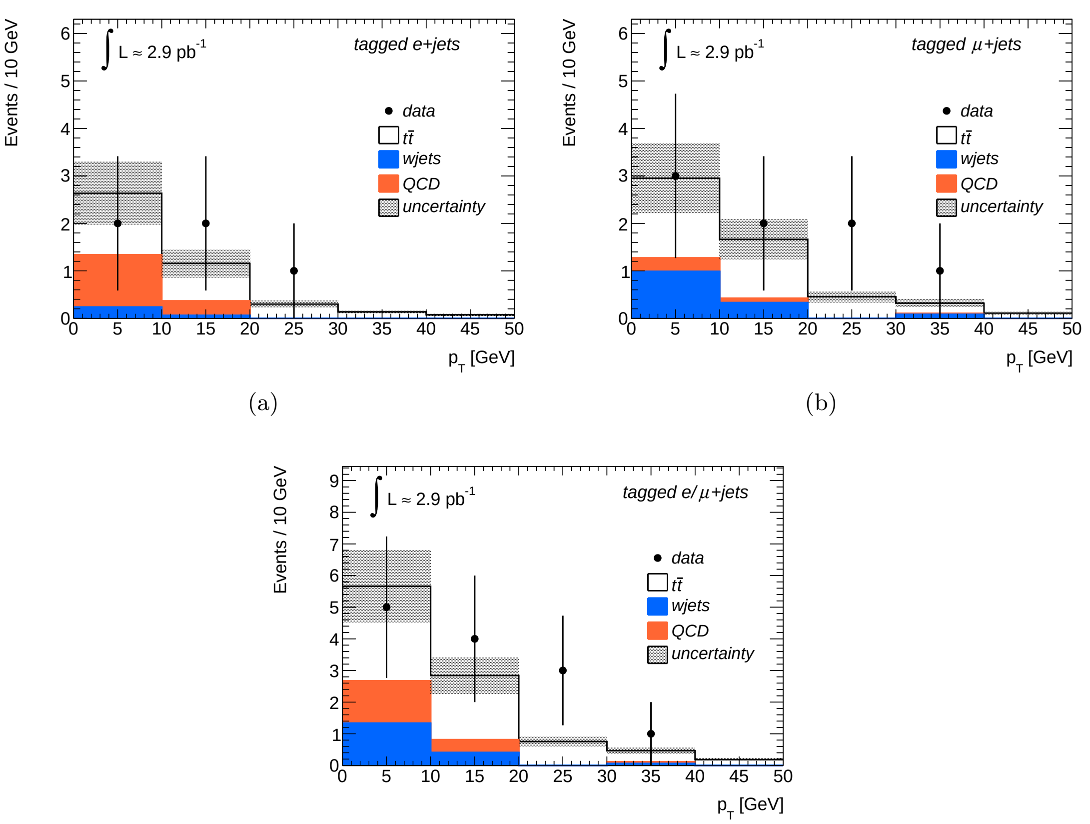

(a)

(b)

(c)

Figure 7.9: Distributions showing the soft muon p_T after full selection criteria, including b-jet tagging, in the electron (a), muon (b) and combining the two channels (c) for events with four or more jets. The data are shown by the points with error bars, compared to the sum of all expected contributions, taken from simulations ($t\bar{t}$) or estimated using a data-driven technique (QCD multijet and W+jets). The hatched area shows the uncertainty on the total expectation due to the uncertainty on the expected contributions.

The uncertainty on the lepton momentum scale and resolution in simulation was measured using the reconstructed distributions of the Z mass. It was found that the electron scale and resolution in simulation were consistent with data. The systematic uncertainty on the electron momentum scale has been estimated as 3% and the uncertainty on the momentum resolution as 50%. For muons, to correct for a few percent discrepancy in the $Z \rightarrow \mu\mu$ mass distributions between data and simulations, the simulated p_T of muons was smeared at the analysis level to reproduce the Z peak observed in data. The systematic uncertainty on this correction is at the 5%-9% percent level [80].

The uncertainty on the jet energy scale and its resolution have been derived by combining information from test-beam data, LHC collision data and simulation [74], and varies in the range 6-10% as a function of jet p_T and η for the jet energy scale and data and simulation agree to within 14% for jet resolution [81]. The use of $Z \rightarrow ee$ and $Z \rightarrow \mu\mu$ events for calculating the lepton trigger, reconstruction and selection efficiencies can be seen in Figure 5.6, the peak in the lepton p_T spectrum for $t\bar{t}$ and Z events is very similar. Care however should be taken when extrapolating these calculations to high p_T ($<$ 100 GeV) as the $t\bar{t}$ lepton p_T spectrum extends beyond the Z sample at this point.

During the data taking periods used in this analysis the LHC instantaneous luminosity varied by several orders of magnitude, reaching a peak of about $1 \times 10^{31} cm^{-2} s^{-1}$. At this luminosity on average two extra pp interactions are superimposed on each collision event, this “pileup” background will produce additional activity in the detector, affecting the isolation energy variables, jet reconstruction and more. Overall, taking into account the average number of additional interactions in the data sample, the impact of the “pileup” on the acceptance for $t\bar{t}$ events is at most 3.6% at the highest luminosity [58], this is not included in the overall systematics.

Table 7.12 lists in detail the sources of systematic uncertainty affecting the signal acceptance estimation. The total number of background events (N_{bkg}) is simply the sum of all the contributions from the QCD and W+jets background processes studied in the previous sections.

Relative uncertainty ($\Delta\sigma/\sigma$)[%]	e+jets	μ+jets
lepton trigger, reconstruction and selection	±3.1	+2.2/-2.3
jet energy scale	±10.4	+9/-9.7
jet energy resolution	±1	±1
jet reconstruction efficiency	+0/-2.6	+0/-2.5
electron energy scale	±1.8	±0.1
electron energy resolution	±0.1	±0.1
muon momentum scale	< 0	±0.3
muon momentum resolution	< 0	±0.1
NLO generator(MC@NLO *vs* POWHEG)	±4.2	±5.7
Parton Shower generator (HERWIG *vs* PYTHIA)	±1.1	±3.0
PDF's	±2.5	±2.4
QCD background	±22.3	±2.9
W+jets background	±2.2	±7.4
Neglected backgrounds	±12.5	±25
b-tag correction factor	±2	±8
Total	+28.4/-28.6	+29.8/-30.1

Table 7.12: Contributions to the uncertainty on the estimated $t\bar{t}$ signal acceptance ε, for electron and muon channels separately, expressed as a relative percentage uncertainty.

The b-tag correction factor uncertainty includes several assumptions regarding its associated uncertainties that are detailed in [58] and cover correlations between $W + bb$+jets, $W + cc$+jets and $W + c$+jets channels.

The systematic uncertainties for the electron and muon channels are considered not to be correlated when combining the two channels uncertainties in quadrature, time constraints meant that a study into potential correlations between the electron and muon channel systematic uncertainties was not possible.

7.9 Summary

A measurement of the cross-section for $t\bar{t}$ production with the ATLAS detector at the LHC with the first few months of pp collision data at $\sqrt{s} = 7$ TeV in the lepton plus jets channel has been carried out and presented. The first few months of data represent an integrated luminosity of 2.9 pb^{-1} in which we have found 13 events (5 in the electron channel and 8 in the muon channel) of which 3.5 ± 1.3 are estimated to have come from Standard Model background processes.

The $t\bar{t}$ production cross-section measurement using the combined electron and muon channels is:

$$\sigma_{t\bar{t}} = 245 \pm 90(\mathrm{stat}) \pm 60(\mathrm{syst}) \pm 32(\mathrm{lum})\mathrm{pb} \tag{7.8}$$

where the first uncertainty is statistical, the second systematic and the third comes from the uncertainty on the delivered integrated luminosity from the LHC.

7.10 Future Measurement

When this analysis was initially conceived in 2007 it was expected that the LHC would have delivered in excess of 100 pb^{-1} of integrated luminosity for analysis by the submission of this thesis. However due to mechanical malfunctions of the LHC and a reduction in LHC beam luminosity as a result, this has not been achieved. Currently the main source of uncertainty in this measurement is statistical and still large fractions of systematic uncertainties come from understanding a new detector in early operation.

Not only does this analysis not include the data collected in late 2010 (which amounts to ≈ 40 pb^{-1}) but also with a large LHC run period in operation for 2011 the integrated luminosity delivered by the LHC and recorded by the ATLAS detector will soon surpass that of the Tevatron. This will allow for the most accurate measurement yet of the $t\bar{t}$ production cross-section.

Chapter 8

Conclusion

A measurement of the top-quark pair production cross section with soft muon b-tagging at $\sqrt{s} = 7$ TeV with early data at the ATLAS detector has been carried out and presented in detail in this thesis.

The work on the electron isolation in $t\bar{t}$ events and the resultant recommendation shown in this thesis was adopted by the ATLAS top-quark working group for use in the first top-quark pair production publication by the ATLAS collaboration [58]. The procedure of correcting for electromagnetic energy around electrons in $t\bar{t}$ events has since been built into the ATLAS software code and a corrected electron isolation energy is now retrievable from data.

The χ^2_{match} efficiency measurement using muons from the decay of J/ψ in data has been used in the final measurement of the top-quark pair production cross section measurement. The monitoring of this efficiency in data will continue as more luminosity from the LHC is delivered.

The final measurement of the top-quark pair production cross section with soft muon b-tagging of 245±90(stat)±60(syst)±30(lum) pb is in agreement with the theoretical cross section of 164.6 pb at approximate NNLO calculations and with the ATLAS measurement using displaced vertex tagging. With more data being delivered by the LHC in 2011 the uncertainties on the cross section measurement will decrease significantly and it is expected by the end of the year that the ATLAS detector will have enough data to produce the most accurate measurement of the top-quark pair production cross section ever.

Bibliography

[1] G. Aad *et al.*, "The ATLAS Experiment at the CERN Large Hadron Collider," *J. Instrum.* **3** (2008) S08003. 437 p.

[2] S. Glashow, "Partial-symmetries of weak interactions," *Nucl. Phys.* **22** (1961) 579–588.

[3] P. W. Higgs, "Broken symmetries and the masses of gauge bosons," *Phys. Rev. Lett.* **13** (1964) 508–509.

[4] A. Salam, *in Elementary Particle Theory, p. 367.* Almqvist and Wiksell, Stockholm, 1968.

[5] S. Weinberg, "A Model of Leptons," *Phys. Rev. Lett.* **19** (1967) 1264–1266.

[6] M. Gell-Mann, "A Schematic Model of Baryons and Mesons," *Phys. Lett.* **8** (1964) 214–215.

[7] G. Zweig, "An SU_3 model for strong interaction symmetry and its breaking; Part II," Tech. Rep. CERN-TH-412, 1964.

[8] C. A. et al. (Particle Data Group), "The Review of Particle Physics," *Physics Letters* **B667** (2008) .

[9] G. Sterman and S. Weinberg, "Jets from Quantum Chromodynamics," *Phys. Rev. Lett.* **39** (1977) 1436–1439.

[10] H. D. Politzer, "Reliable Perturbative Results for Strong Interactions?," *Phys. Rev. Lett.* **30** (1973) 1346–1349.

[11] M. L. Coffman, "Correction to the Rydberg Constant for Finite Nuclear Mass," *American Journal of Physics* **33** (1965) 820–823.

[12] P. Kusch and H. M. Foley, "The Magnetic Moment of the Electron," *Phys. Rev.* **74** (1948) 250–263.

[13] E. Fermi, "Towards the theory of β rays," *Z. Phys* **88** (1934) .

[14] N. Cabibbo, "Unitary Symmetry and Leptonic Decays," *Phys. Rev. Lett.* **10** (1963) 531–533.

[15] M. Kobayashi and T. Maskawa, "CP-Violation in the Renormalizable Theory of Weak Interaction," *Progress of Theoretical Physics* **49** (1973) 652–657.

[16] Y. Fukuda *et al.*, "Evidence for Oscillation of Atmospheric Neutrinos," *Phys. Rev. Lett.* **81** (1998) 1562–1567.

[17] F. J. Hasert *et al.*, "Search for elastic muon-neutrino electron scattering," *Phys. Lett.* **46B** (1973) 121.

[18] F. J. Hasert *et al.*, "Observation of neutrino-like interactions without muon or electron in the Gargamelle neutrino experiment," *Phys. Lett.* **46B** (1973) 138.

[19] F. J. Hasert *et al.*, "Observation of neutrino-like interactions without muon or electron in the Gargamelle neutrino experiment," *Nucl. Lett.* **B73** (1974) 1.

[20] R. Barate *et al.*, "Search for the Standard Model Higgs boson at LEP," *Phys. Lett.* **B565** (2003) 61–75, `arXiv:hep-ex/0306033`.

[21] T. Aaltonen *et al.*, "Combined CDF and DØ Upper Limits on Standard Model Higgs Boson Production with up to 8.2 fb^{-1} of Data (2011)," `arXiv:1103.3233 [hep-ex]`.

[22] N. Jarosik, C. Bennett, J. Dunkley, B. Gold, M. Greason, *et al.*, "Seven-Year Wilkinson Microwave Anisotropy Probe (WMAP) Observations: Sky Maps, Systematic Errors, and Basic Results," *Astrophys.J.Suppl.* **192** (2011) 14, `arXiv:1001.4744 [astro-ph.CO]`.

[23] S. Dimopoulos, S. Raby, and F. Wilczek, "Supersymmetry and the scale of unification," *Phys. Rev. D* **24** (1981) 1681–1683.

[24] M. L. Perl *et al.*, "Evidence for Anomalous Lepton Production in $e^+ - e^-$ Annihilation," *Phys. Rev. Lett.* **35** (1975) 1489–1492.

[25] S. W. Herb *et al.*, "Observation of a Dimuon Resonance at 9.5 GeV in 400-GeV Proton-Nucleus Collisions," *Phys. Rev. Lett.* **39** (1977) 252–255.

[26] F. Abe *et al.*, "Observation of Top Quark Production in $p\bar{p}$ Collisions with the Collider Detector at Fermilab," *Phys. Rev. Lett.* **74** (1995) 2626–2631.

[27] S. Abachi *et al.*, "Search for High Mass Top Quark Production in $p\bar{p}$ Collisions at $\sqrt{s} = 1.8$ TeV," *Phys. Rev. Lett.* **74** (1995) 2422–2426.

[28] J. F. Arguin *et al.*, "Combination of CDF and D∅ Results on the Mass of the Top Quark," `arXiv:hep-ex/0507091 [hep-ex]`.

[29] U. Langenfeld, S. Moch, and P. Uwer, "Measuring the running top-quark mass," *Phys. Rev.* **D80** (2009) 054009, `arXiv:0906.5273 [hep-ph]`.

[30] M. A. Dobbs *et al.*, "Les Houches guidebook to Monte Carlo generators for hadron collider physics (2004)," `hep-ph/0403045`.

[31] B. Andersson, G. Gustafson, G. Ingelman, and T. Sjöstrand, "Parton fragmentation and string dynamics," *Physics Reports* **97** (1983) 31 – 145.

[32] T. Sjöstrand, S. Mrenna, and P. Z. Skands, "PYTHIA 6.4 Physics and Manual," *JHEP* **05** (2006) 026, `arXiv:hep-ph/0603175`.

[33] T. Gleisberg *et al.*, "Event generation with SHERPA 1.1," *JHEP* **02** (2009) 007, `arXiv:0811.4622 [hep-ph]`.

[34] G. Corcella *et al.*, "HERWIG 6.5: an event generator for Hadron Emission Reactions With Interfering Gluons (including supersymmetric processes)," *JHEP* **01** (2001) 010, `arXiv:hep-ph/0011363`.

[35] A. Schälicke, T. Gleisberg, S. Höche, S. Schumann, J. Winter, F. Krauss, and G. Soff, "An event generator for particle production in high-energy collisions," *Progress in Particle and Nuclear Physics* **53** (2004) 329 – 338.

[36] A. Shibata *et al.*, "Understanding Monte Carlo Generators for Top Physics," Tech. Rep. ATL-COM-PHYS-2009-334, CERN, Geneva, June, 2009.

[37] J. M. Butterworth, J. R. Forshaw, and M. H. Seymour, "Multiparton interactions in photoproduction at HERA," *Z. Phys.* **C72** (1996) 637–646, `arXiv:hep-ph/9601371`.

[38] S. Frixione and B. R. Webber, "Matching NLO QCD computations and parton shower simulations," *JHEP* **06** (2002) 029, `arXiv:hep-ph/0204244`.

[39] M. L. Mangano, M. Moretti, F. Piccinini, R. Pittau, and A. D. Polosa, "ALPGEN, a generator for hard multiparton processes in hadronic collisions," *JHEP* **07** (2003) 001, `arXiv:hep-ph/0206293`.

[40] J. Allison *et al.*, "Geant4 developments and applications.," *IEEE Transactions on Nuclear Science* **53(1)** (2006) 270–278.

[41] G. Agostinelli *et al.*, "Geant4 - A Simulation Toolkit," *CERN-LCGAPP* **A 506** (2003) 250–303.

[42] A. Ribon *et al.*, "Status of Geant4 hadronic physics for the simulation of LHC experiments at the start of LHC physics program," *CERN-LCGAPP-2010-002* .

[43] "Atlas computing: Technical Design Report," Tech. Rep. CERN-LHCC-2005-022, CERN, Geneva, 2005.

[44] T. Cornelissen *et al.*, "Concepts, Design and Implementation of the Atlas New Tracking (NEWT)," Tech. Rep. ATL-SOFT-PUB-2007-007. ATL-COM-SOFT-2007-002, CERN, Geneva, Mar., 2007.

[45] G. Aad *et al.*, "Expected Performance of the Atlas Experiment - Detector, Trigger and Physics," `arXiv:0901.0512 [hep-ex]`.

[46] Aharrouche. *et al.*, "Electron performance in the Atlas experiment," Tech. Rep. ATL-COM-PHYS-2010-208, Geneva, 2010.

[47] S. Hassini *et al.*, "Muon track reconstruction in the Atlas experiment," *NIM* **A572** (2007) 77–79.

[48] T. Lagouri *et al.*, "A muon identification and combined reconstruction procedure for the Atlas detector at the LHC at CERN," *IEEE Trans. Nucl. Sci.* **51** (2004) 3030–3033.

[49] D. Adams *et al.*, "Track reconstruction in the atlas muon spectrometer with moore," Tech. Rep. ATL-SOFT-2003-007, CERN, Geneva, May, 2003.

[50] B. Abbott *et al.*, "Study on reconstructed object definition and selection for top physics," Tech. Rep. ATL-COM-PHYS-2009-633, CERN, Geneva, Dec., 2009.

[51] S. D. Ellis and D. E. Soper, "Successive combination jet algorithm for hadron collisions," *Phys. Rev.* **D48** (1993) 3160–3166, `arXiv:hep-ph/9305266`.

[52] S. Catani, Y. L. Dokshitzer, and B. R. Webber, "The $k_\perp$-clustering algorithm for jets in deep inelastic scattering and hadron collisions," *Phys. Lett. B* **285** no. CERN-TH-6473-92. LU-TP-92-14, (Mar., 1992) 291–299. 13 p.

[53] J. Hartert and I. Ludwig, "Electron isolation in the Atlas experiment," Tech. Rep. ATL-COM-PHYS-2010-070, CERN, Geneva, Feb., 2010.

[54] B. Acharya *et al.*, "Prospects for measuring the Top Quark Pair Production Cross-section in the Single Lepton Channel at Atlas in 10 TeV p-p Collisions," Tech. Rep. ATL-COM-PHYS-2009-306, CERN, Geneva, 2009.

[55] K. Bachas *et al.*, "A measurement of the atlas muon reconstruction and trigger efficiency using j/ψ decays," Tech. Rep. ATLAS-CONF-2011-021, CERN, Geneva, Jan., 2011.

[56] N. Benekos *et al.*, "Lepton Trigger and Identification for the first *Top quark* observation," Tech. Rep. ATL-COM-PHYS-2010-826, CERN, Geneva, Oct, 2010.

[57] "Expected electron performance in the Atlas experiment," Tech. Rep. ATL-PHYS-PUB-2011-006, CERN, Geneva, Apr, 2011.

[58] T. W. group, "Observation of top quark pair production in the semileptonic decay channel at $\sqrt{s} = 7$ TeV with the Atlas detector," Tech. Rep. ATL-COM-PHYS-2010-855, CERN, Geneva, Oct, 2010.

[59] N. Brambilla *et al.*, "Heavy quarkonium physics," `arXiv:hep-ph/0412158`.

[60] V. Boisvert, L. Cerrito, B. Cooper, R. Goncalo, A. J. Poll, and M. Rose, "Extension of the Atlas Soft Muon Tagging Algorithm to use Muon Reconstruction Quality Criteria," Tech. Rep. ATL-COM-PHYS-2010-335, CERN, Geneva, June, 2010.

[61] S. Hassani, C. Petridou, D. Iliadis, and K. Bachas, "The Tag and Probe method with $J/\psi \to \mu^+\mu^-$ and $\Upsilon \to \mu^+\mu^-$ candidates in Atlas," Tech. Rep. ATL-COM-PHYS-2009-618, CERN, Geneva, Nov., 2010.

[62] "Atlas Monte Carlo tunes for MC09," Tech. Rep. ATL-PHYS-PUB-2010-002, CERN, Geneva, Mar, 2010.

[63] A. Sherstnev and R. S. Thorne, "Parton Distributions for LO Generators," *Eur. Phys. J.* **C55** (2008) 553–575, `arXiv:0711.2473 [hep-ph]`.

[64] P. Nason *et al.*, “Bottom production,” `arXiv:hep-ph/0003142`.

[65] A. Salzburger, *A Parametrization for Fast Simulation of Muon Tracks in the* ATLAS *Inner Detector and Muon System.* PhD thesis, Leopold-Franzens-Univ. Innsbruck, Innsbruck, 2003.

[66] S. Cheatham, “Quarkonia studies with early ATLAS data,” `arXiv:0906.0308 [hep-ex]`.

[67] *ROOT homepage [online].*
http://root.cern.ch/, 2011.

[68] F. James and M. Roos, “Minuit: A System for Function Minimization and Analysis of the Parameter Errors and Correlations,” *Comput. Phys. Commun.* **10** (1975) 343–367.

[69] B. Lenzi, R. Nicolaidou, and S. Hassani, “Trackincalotools: A package for measuring muon energy loss and calorimetric isolation in ATLAS,” *Journal of Physics: Conference Series* **219** (2010) 032049.
`http://stacks.iop.org/1742-6596/219/i=3/a=032049`.

[70] U. Langenfeld, S. Moch, and P. Uwer, “New results for $t\bar{t}$ production at hadron colliders,” `arXiv:0907.2527 [hep-ph]`.

[71] S. Moch and P. Uwer, “Theoretical status and prospects for top-quark pair production at hadron colliders,” *Phys. Rev.* **D78** (2008) 034003, `arXiv:0804.1476 [hep-ph]`.

[72] G. Aad *et al.*, “The ATLAS Simulation Infrastructure,” *European Physical Journal C* (2010) 823–874, `arXiv:1005.4568 [physics.ins-det]`.

[73] M. Cacciari, G. P. Salam, and G. Soyez, “The anti-k_t jet clustering algorithm,” *JHEP* **04** (2008) 063, `arXiv:0802.1189 [hep-ph]`.

[74] G. Aad *et al.*, "Measurement of inclusive jet and dijet cross sections in proton-proton collisions at 7 TeV centre-of-mass energy with the ATLAS detector," *Eur. Phys. J.* **C71** (2011) 1512, `arXiv:1009.5908 [hep-ex]`.

[75] A. Canepa *et al.*, "Missing Transverse Energy for Top Physics analyses with early ATLAS data at $\sqrt{s}$=7 TeV," Tech. Rep. ATL-COM-PHYS-2010-821, CERN, Geneva, Oct., 2010.

[76] B. Abi *et al.*, "Mis-identified lepton backgrounds to top quark pair production," Tech. Rep. ATL-COM-PHYS-2010-849, CERN, Geneva, Oct., 2010.

[77] F. A. Berends, H. Kuijf, B. Tausk, and W. T. Giele, "On the production of a W and jets at hadron colliders," *Nuclear Physics B* **357** (1991) 32 – 64.

[78] S. D. Ellis, R. Kleiss, and W. J. Stirling, "W's, Z's and jets," *Physics Letters B* **154** (1985) 435 – 440.

[79] B. Alvarez *et al.*, "B-tagging for top physics analyses with early ATLAS data at $\sqrt{s}$ = 7 TeV," Tech. Rep. ATL-COM-PHYS-2010-846, CERN, Geneva, Oct., 2010.

[80] B. G. da Costa *et al.*, "$W \to \mu\nu$ and $Z \to \mu\mu$ cross-sections measurements in proton-proton collisions at vs = 7 TeV with the ATLAS Detector," Tech. Rep. ATL-COM-PHYS-2010-685, CERN, Geneva, Aug., 2010.

[81] "Jet energy resolution and selection efficiency relative to track jets from in-situ techniques with the ATLAS Detector Using Proton-Proton Collisions at a Center of Mass Energy $\sqrt{s}$ = 7 TeV," Tech. Rep. ATLAS-CONF-2010-054, CERN, Geneva, July, 2010.

[82] D. Aitree *et al.*, "The Evaporative Cooling System for the ATLAS Inner Detector," Tech. Rep. ATL-INDET-PUB-2008-006. ATL-COM-INDET-2008-007, CERN, Geneva, Apr., 2008.

Appendix A

SCT SR1 Sectors and Shift Monitoring

A.1 Introduction

As mentioned in Section 2.2.4, the Semiconductor Tracker (SCT) is a sub-detector of the ATLAS Inner Detector. The SCT works in tandem with the other elements of the ID, such as the TRT and Pixel Tracker to provide a picture of particle collisions close to the event interaction point. The SCT design and the silicon microstrip technology used in its construction has seen use in major particle physics experiments over the past 8 years such as at LEP and within the detectors in operation at the Tevatron. Therefore there is a wealth of knowledge and experience in the operation of such devices, however the SCT within ATLAS will be exposed to 10-20 times the radiation fluences of those in the past and has an area 50 times larger.

Due to the size, radiation exposure and cooling requirements there are a number of challenges facing the day-to-day operation of the SCT within ATLAS. During my time spent working at CERN from October 2007 through to July 2009 I experienced first hand these and other issues. I took on the role of monitoring the SCT through shift work within the Atlas control room and helped in the construction of a “mini”-SCT, in the form of the SR1 Barrel and Endcap Sectors, that is used extensively in the training of new SCT shift persons.

A.2 SCT SR1 Sectors

A.2.1 Purpose

In the run up to the initial start up of the LHC in 2008 it was noted that there was a lack of required shift persons for the SCT and getting hands-on experience of the operation and monitoring for shifters was difficult while experts still required time and access to the detector for calibration. It was thus proposed early in 2008 that the spare modules from the barrel and endcap sectors of the SCT would be used to build a “mini”-SCT that would mirror the shift experience of the full SCT detector to give newly trained persons the experience and confidence to run the full detector by themselves.

A.2.2 Barrel and Endcap Sectors

The modules available to use consisted of 48 spare barrel modules and one quadrant of an end cap disk 2 (33 modules). The barrel sector can be seen in Figure A.1 before the cooling for the modules was attached and the sector closed off. The endcap sector seen in Figure A.2 came almost pre-assembled from its previous test location but with all power supply and signal fibre optic cables removed.

The planning and construction of the barrel sector began in mid-March 2008 and was completed by mid-July. Work on adding the endcap sector to the “mini”-SCT began in early November 2008 and was in operation by the end of December 2008. As a non-expert my work was limited to the connecting, mapping and testing of the power supply and fibre optic cables. Also as a fully trained up SCT shift person I helped test

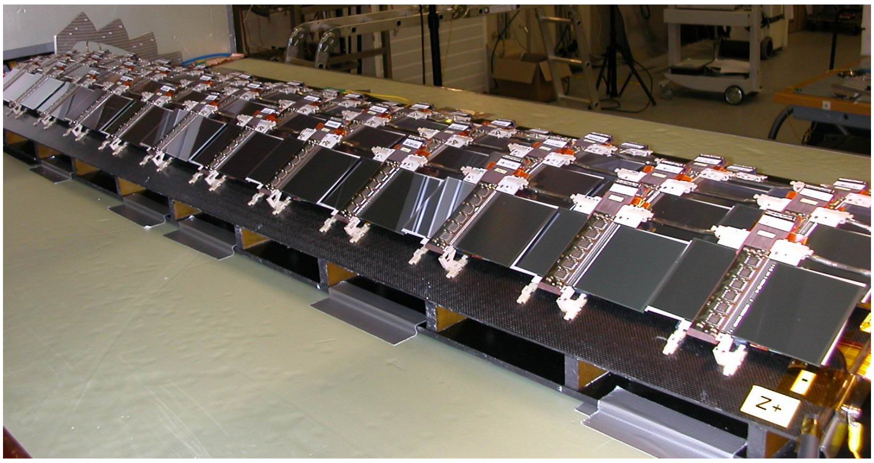

Figure A.1: The 48 barrel sector modules after being attached to the harness within the SR1 building.

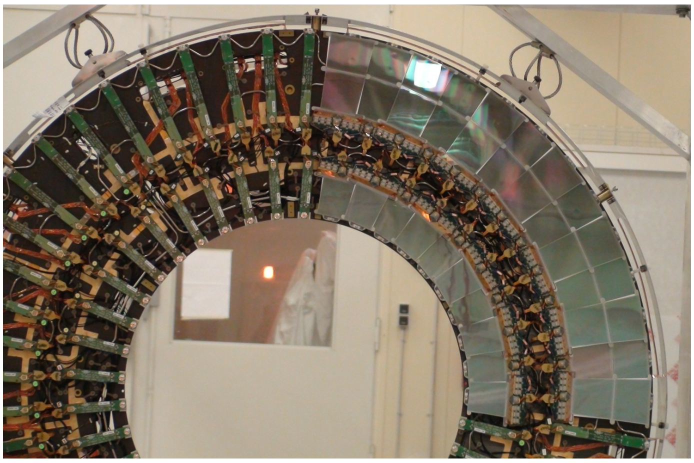

Figure A.2: The 33 end cap modules, (13 outer, 10 middle and 10 inner) attached to the disk quadrant.

the operation of the SR1 sector with experts and helped write the user guide for the operation of the sector from a non-expert point of view.

A.3 SCT Monitoring

As a SCT shift person I undertook approximately one month of shifts in the ATLAS control room and thus had an active role in identifying faults and problems with the SCT during the initial operation during cosmic runs. A typical shift on the SCT involved the monitoring of 4 different sub-systems, the Data Acquisition Software (DAQ), the Detector Control System (DCS), the Data Quality Monitor (DQM) and the Inner Detector Environmental Monitoring (IDE).

A.3.1 DCS and IDE monitoring

Shifts on the SCT involved being responsible for not only the monitoring of the environmental conditions for the SCT but also for the Pixel detector. The details of the evaporative cooling system used for the SCT and Pixel detectors can be found in [82]. In summary the system uses the fluorocarbon C_3F_8 to cool the detectors by transferring heat from the detectors to the C_3F_8 in a gaseous state and then the fluorocarbon is cooled back to a liquid outside the detector using a series of compressors and heat exchangers.

The main role while monitoring the cooling system was to take careful note of temperatures, pressures and fluid level of the C_3F_8 at critical points in its cycle, such as the inlet and outlet of the detectors and before and after the compressors. The monitoring of the cooling was done both through the IDE and DCS software and our control as a shifter was limited to turning the cooling loop on and off. Any further actions required expert assistance.

The DCS part of the SCT could involve a lot of monitoring and action during particular times, such as during LHC beam injection periods. During beam injection of the LHC, the SCT is put into a standby state where the chip voltages are lowered to a state where should accidental beam collisions occur during beam injection and alignment, the minimum amount of damage will be caused to the SCT. Once the LHC beam is declared stable the voltages applied to the SCT modules are raised to operating levels and in general during my time on shift on the SCT the behaviour of the detector was very stable during runs. A view of the DCS software with ATLAS ready for collisions is shown in Figure A.3.

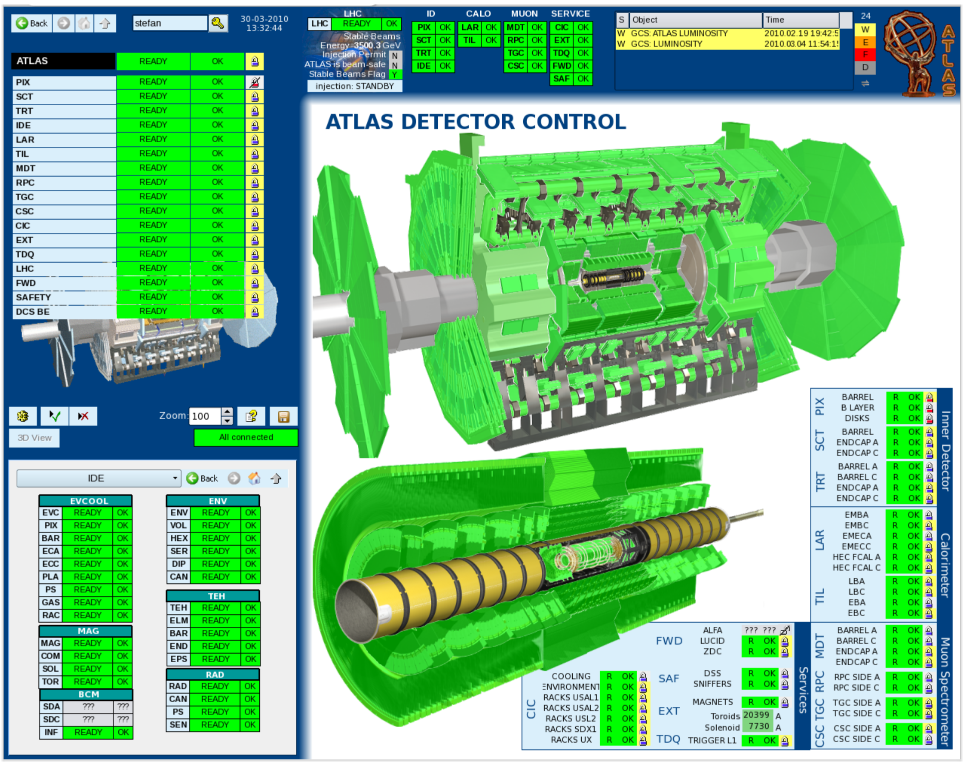

Figure A.3: Overview of the ATLAS detector monitoring control system, showing the full detector ready for collisions.

A.3.2 Data Acquisition Software

The DAQ software is responsible for the calibration, configuration and control of the SCT, although the vast majority of this functionality was not accessible for shifters.

The role of the DAQ software during a shift was to ensure the correct configuration of the SCT was loaded before a run. During run conditions the DAQ software was the only means to try to recover modules that went "busy" for any number of reasons.

However, when not in run conditions the shifter could run scans and calibrations on the SCT and I was at times asked by experts to preform certain scans to help diagnose problems and calibrate the detector. An example of one of these scans is shown in Figure A.4, which shows an overview of the DAQ software window on the left, with the results of a strode delay scan on one module show to the right.

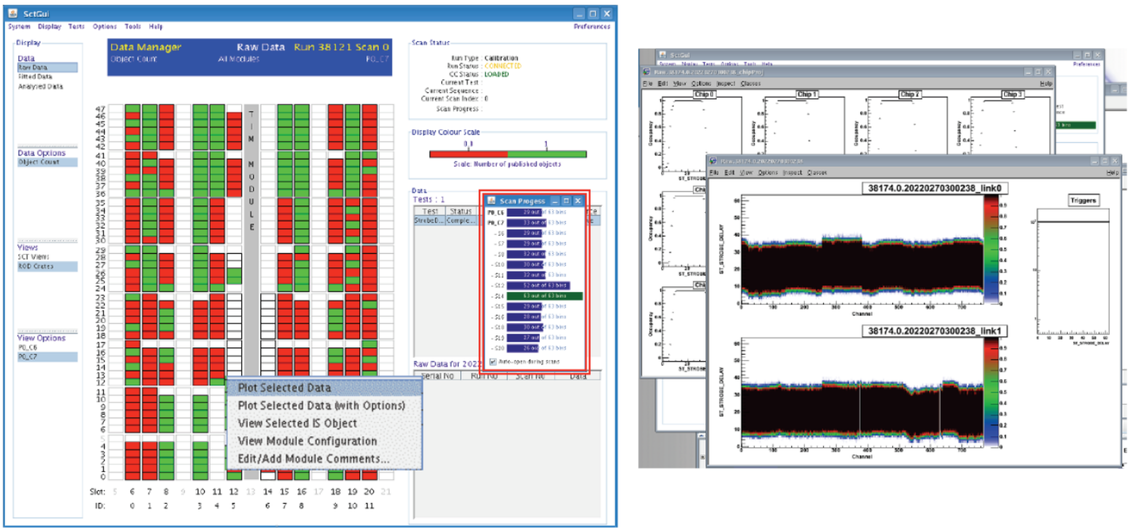

Figure A.4: View of the SCT Data Acquisition Software (DAQ), showing the results of a strode delay scan in progress.

A.3.3 Data Quality Monitor

The DQM software is used to look at the data coming out of the different sectors of the SCT during a run. As the reliability of the various SCT sub-systems improved during my time doing shifts, so did the importance of actively monitoring the quality of data the SCT was producing during a run, instead of through the offline tools a few days later. During my final few shifts I spent the vast majority of my time looking at the output of the DQM software.

The DQM allowed the monitoring of various aspects of the SCT such as:

- Module and layer noise occupancy;
- Module and layer error summary;
- Module and layer efficiency summary;
- SCT track residuals.

All of the above histograms were required to be checked on an hourly basis, with any modules showing particular faults noted for the experts to look into further. An example of a barrel layer residual is shown in Figure A.5. Although at the time there were not any reference histograms to compare the live output against, a collection of reference plots are now available for shifters to compare against.

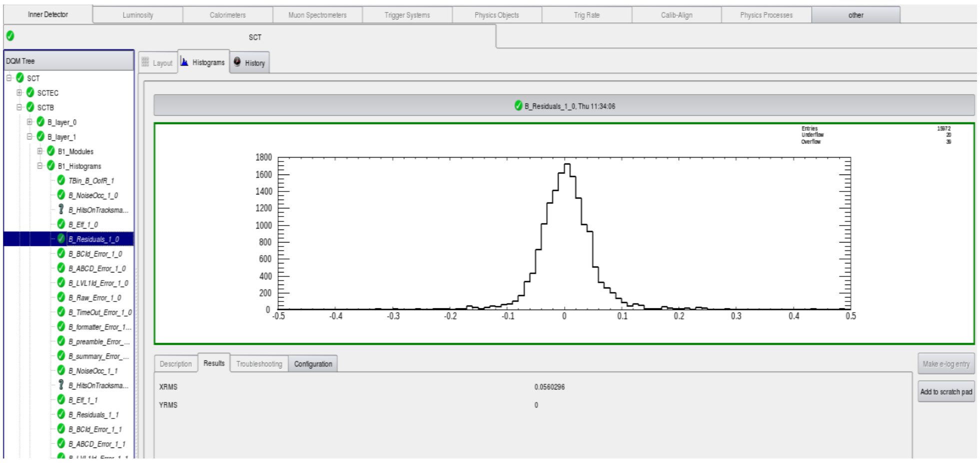

Entries 15972
Underflow 20
Overflow 39

XRMS 0.0560296
YRMS 0

Figure A.5: Screenshot of the SCT Data Quality Monitor (DQM) showing the barrel sector residuals during a run.

Appendix B

Soft Muon Efficiency Tables

The results quoted here correspond to those discussed in Section 6.8 and represent the numbers arising from the methods described in Sections 6.6.1, 6.6.2, 6.7. For data the signal value represents the area returned after background subtraction in a 3σ window centred on the world-average J/ψ mass. The minimum and maximum signal are calculated by varying the parametrized background slope and constant within their uncertainties, see Figure 6.4 and repeating the signal measurement with these new measurements. The signal returned by increasing the signal window to 5σ is shown alongside the 3σ in brackets. Statistical uncertainties are calculated using Equation 6.4.

For Monte Carlo there exists no background in the sample and therefore the only systematic studied is the change in calculated efficiency in varying the signal window width from 3σ to 5σ. The statistical uncertainty calculation remains the same as for data.

B.0.4 Combined Muon Reconstruction Efficiencies From Data

	Inner Detector Probe		
p_T bin [GeV]	Signal	Max Signal	Min Signal
4–6	25232.1 (25935.8)	25260.0 (25982.3)	25204.2 (25889.3)
6–8	9170.7 (9529.8)	9182.2 (9548.9)	9159.2 (9510.7)
8–10	4507.4 (4535.3)	4514.4 (4547.0)	4500.3 (4523.5)
10+	4568.1 (4535.2)	4568.1 (4557.0)	4555.0 (4513.4)
Total	41848.3 (43217.2)	41974.6 (43427.7)	41722.1 (43006.8)

Table B.1: Measured signal as a function of p_T for a signal region of 3σ (5σ) for inner detector probes in data.

	Muon Probe		
p_T bin [GeV]	Signal	Max Signal	Min Signal
4–6	21854.2 (22481.3)	21855.4 (22483.3)	21852.9 (22479.2)
6–8	8818.4 (9061.7)	8818.8 (9062.4)	8818.0 (9061.0)
8–10	3747.7 (3800.1)	3747.7 (3800.1)	3747.7 (3800.2)
10+	3694.9 (3716.6)	3695.8 (3718.1)	3694.1 (3715.1)
Total	37926.2 (39039.0)	37927.7 (39041.5)	37924.7 (39036.6)

Table B.2: Measured signal as a function of p_T for a signal region of 3σ (5σ) for muon probes in data.

p_T bin [GeV]	Data Efficiency [%]	Stat. Unc. [%]	Sys. Unc. [%]
4–6	86.61	± 0.23	± 0.12
6–8	96.16	± 0.20	± 1.12
8–10	83.15	± 0.61	± 0.79
10+	80.89	± 0.65	± 1.34
Total	90.63	± 0.15	± 0.43

Table B.3: Combined muon efficiency as a function of p_T with statistical and systematic uncertainties in data.

	Inner Detector Probe		
η bin	Signal	Max Signal	Min Signal
(-3)–(-2)	2093.2 (1926.4)	2118.2 (1967.9)	2068.3 (1884.8)
(-2)–(-1)	9315.5 (10287.5)	9334.9 (10319.9)	9296.1 (10255.2)
(-1)–0	11142.5 (12339.8)	11154.8 (12360.4)	11130.1 (12319.2)
0–1	11503.4 (11273.3)	11515.8 (11294.0)	11490.9 (11252.5)
1–2	9592.6 (9484.0)	9611.5 (9515.5)	9573.7 (9452.5)
2–3	1964.2 (2005.0)	1991.6 (2050.7)	1936.8 (1959.3)

Table B.4: Measured signal as a function of η for a signal region of 3σ (5σ) for inner detector probes in data.

	Muon Probe		
η bin	Signal	Max Signal	Min Signal
(-3)–(-2)	2026.2 (1691.8)	2050.4 (1693.0)	2002.1 (1690.0)
(-2)–(-1)	7760.1 (7920.5)	7761.2 (7922.4)	7758.9 (7918.5)
(-1)–0	9282.1 (9485.9)	9281.8 (9485.3)	9282.5 (9486.5)
0–1	9915.6 (10092.4)	9915.9 (10092.8)	9915.3 (10091.9)
1–2	8262.4 (8338.4)	8262.4 (8339.8)	8263.3 (8337.0)
2–3	1998.0 (1946.6)	1998.0 (1953.1)	1993.9 (1940.1)

Table B.5: Measured signal as a function of η for a signal region of 3σ (5σ) for muon probes in data.

η bin	Data Efficiency [%]	Stat. Unc. [%]	Sys. Unc. [%]
(-3)–(-2)	96.80	± 0.39	± 9.41
(-2)–(-1)	83.30	± 0.42	± 7.58
(-1)–0	83.30	± 0.39	± 7.72
0–1	86.20	± 0.35	± 3.86
1–2	86.13	± 0.38	± 2.08
2–3	101.72	± 0.30	± 4.77

Table B.6: Combined muon efficiency as a function of η with statistical and systematic uncertainties in data.

	Inner Detector Probe		
ϕ bin	Signal	Max Signal	Min Signal
(-3.2)–(-2)	8968.6 (8799.7)	8983.1 (8823.8)	8954.1 (8775.5)
(-2)–(-1)	6751.9 (7372.2)	6764.8 (7393.7)	6739.0 (7350.7)
(-1)–0	7592.6 (7772.2)	7605.6 (7794.0)	7579.5 (7750.5)
0–1	7911.5 (8155.6)	7925.0 (8178.1)	7898.0 (8133.1)
1–2	6991.7 (7335.6)	7005.3 (7358.2)	6978.2 (7313.0)
2–3.2	8081.3 (8674.4)	8095.0 (8697.3)	8067.6 (8651.6)

Table B.7: Measured signal as a function of ϕ for a signal region of 3σ (5σ) for inner detector probes in data.

	Muon Probe		
ϕ bin	Signal	Max Signal	Min Signal
(-3.2)–(-2)	6782.2 (6894.7)	6783.1 (6896.1)	6781.4 (6893.3)
(-2)–(-1)	5376.1 (5553.2)	5376.5 (5553.8)	5375.8 (5552.6)
(-1)–0	6161.1 (6291.2)	6161.3 (6291.5)	6160.9 (6290.8)
0–1	6660.9 (6799.8)	6374.5 (6800.2)	6660.7 (6799.4)
1–2	6373.7 (6583.9)	6374.5 (6585.1)	6373.0 (6582.6)
2–3.2	7024.1 (7239.5)	7024.4 (7239.9)	7023.8 (7239.1)

Table B.8: Measured signal as a function of ϕ for a signal region of 3σ (5σ) for muon probes in data.

ϕ bin	Data Efficiency [%]	Stat. Unc. [%]	Sys. Unc. [%]
(-3)–(-2)	75.62	± 0.52	± 3.61
(-2)–(-1)	79.62	± 0.55	± 5.40
(-1)–0	81.15	± 0.50	± 0.29
0–1	84.19	± 0.45	± 0.98
1–2	91.16	± 0.36	± 1.55
2–3	86.92	± 0.40	± 3.98

Table B.9: Combined muon efficiency as a function of ϕ with statistical and systematic uncertainties in data.

B.0.5 Combined Muon Reconstruction Efficiencies From Monte Carlo

	Inner Detector Probe	
p_T bin [GeV]	Signal 3σ	Signal 5σ
4–6	894986	914867
6–8	297390	304626
8–10	113693	116549
10+	102446	103964
Total	1409076	1439767

Table B.10: Measured signal as a function of p_T for a signal region of 3σ (5σ) for inner detector probes in Monte Carlo.

	Muon Probe	
p_T bin [GeV]	Signal 3σ	Signal 5σ
4–6	775732	792033
6–8	282152	287914
8–10	107872	110044
10+	96337	97460
Total	1262442	1287264

Table B.11: Measured signal as a function of p_T for a signal region of 3σ (5σ) for muon probes in Monte Carlo.

p_T bin [GeV]	Data Efficiency [%]	Stat. Unc. [%]	Sys. Unc. [%]
4–6	86.68	± 0.04	± 0.10
6–8	94.88	± 0.04	± 0.36
8–10	94.88	± 0.07	± 0.46
10+	94.04	± 0.08	± 0.29
Total	89.59	± 0.03	± 0.19

Table B.12: Combined muon efficiency as a function of p_T with statistical and systematic uncertainties in Monte Carlo.

	Inner Detector Probe	
η bin	Signal 3σ	Signal 5σ
(-3)–(-2)	57032	57946
(-2)–(-1)	299784	302427
(-1)–0	355171	358674
0–1	358429	361876
1–2	301645	304061
2–3	57171	58057

Table B.13: Measured signal as a function of η for a signal region of 3σ (5σ) for inner detector probes in Monte Carlo.

	Muon Probe	
η bin	Signal 3σ	Signal 5σ
(-3)–(-2)	57394	57742
(-2)–(-1)	273378	275909
(-1)–0	302931	305692
0–1	311390	314117
1–2	275637	277709
2–3	57479	57764

Table B.14: Measured signal as a function of η for a signal region of 3σ (5σ) for muon probes in Monte Carlo.

η bin	Data Efficiency [%]	Stat. Unc. [%]	Sys. Unc. [%]
(-3)–(-2)	100.63	± 0.03	± 0.99
(-2)–(-1)	91.19	± 0.05	± 0.04
(-1)–0	85.29	± 0.06	± 0.06
0–1	86.88	± 0.06	± 0.07
1–2	91.38	± 0.05	± 0.04
2–3	100.54	± 0.03	± 1.04

Table B.15: Combined muon efficiency as a function of η with statistical and systematic uncertainties in Monte Carlo.

	Inner Detector Probe	
ϕ bin	Signal 3σ	Signal 5σ
(-3.2)–(-2)	251892	257380
(-2)–(-1)	217221	222123
(-1)–0	222681	227515
0–1	229311	234642
1–2	229675	234806
2–3.2	257900	263369

Table B.16: Measured signal as a function of ϕ for a signal region of 3σ (5σ) for inner detector probes in Monte Carlo.

	Muon Probe	
ϕ bin	Signal 3σ	Signal 5σ
(-3.2)–(-2)	219986	224482
(-2)–(-1)	189608	193684
(-1)–0	198922	202837
0–1	212064	216362
1–2	211371	215451
2–3.2	230162	234493

Table B.17: Measured signal as a function of ϕ for a signal region of 3σ (5σ) for muon probes in Monte Carlo.

ϕ bin	Data Efficiency [%]	Stat. Unc. [%]	Sys. Unc. [%]
(-3)–(-2)	87.33	± 0.07	± 0.12
(-2)–(-1)	87.29	± 0.08	± 0.09
(-1)–0	89.33	± 0.07	± 0.18
0–1	92.48	± 0.06	± 0.27
1–2	92.03	± 0.06	± 0.27
2–3	89.24	± 0.06	± 0.21

Table B.18: Combined muon efficiency as a function of ϕ with statistical and systematic uncertainties in Monte Carlo.

Appendix C

Top-Quark Pair Production Cross Section Data Distributions

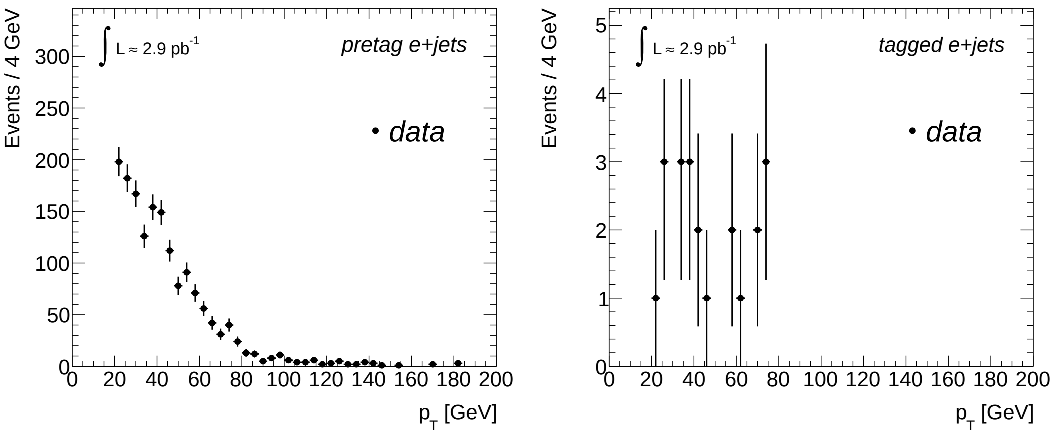

(a)

(b)

Figure C.1: Distribution of the p_T of the electron for the events passing all pre b-jet tagging event selection criteria in the electron channel (a) and after b-jet tagging (b) for events with one or more jets.

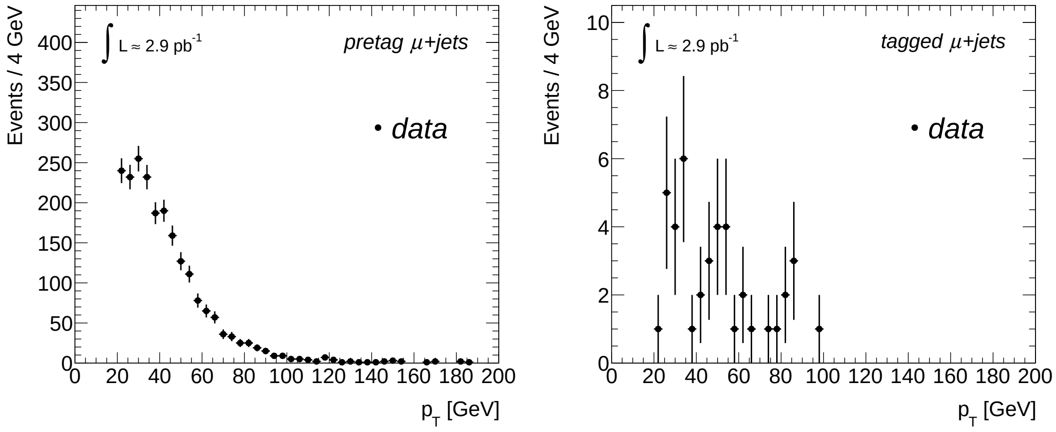

(a) (b)

Figure C.2: Distribution of the p_T of the muon for the events passing all pre b-jet tagging event selection criteria in the muon channel (a) and after b-jet tagging (b) for events with one or more jets.

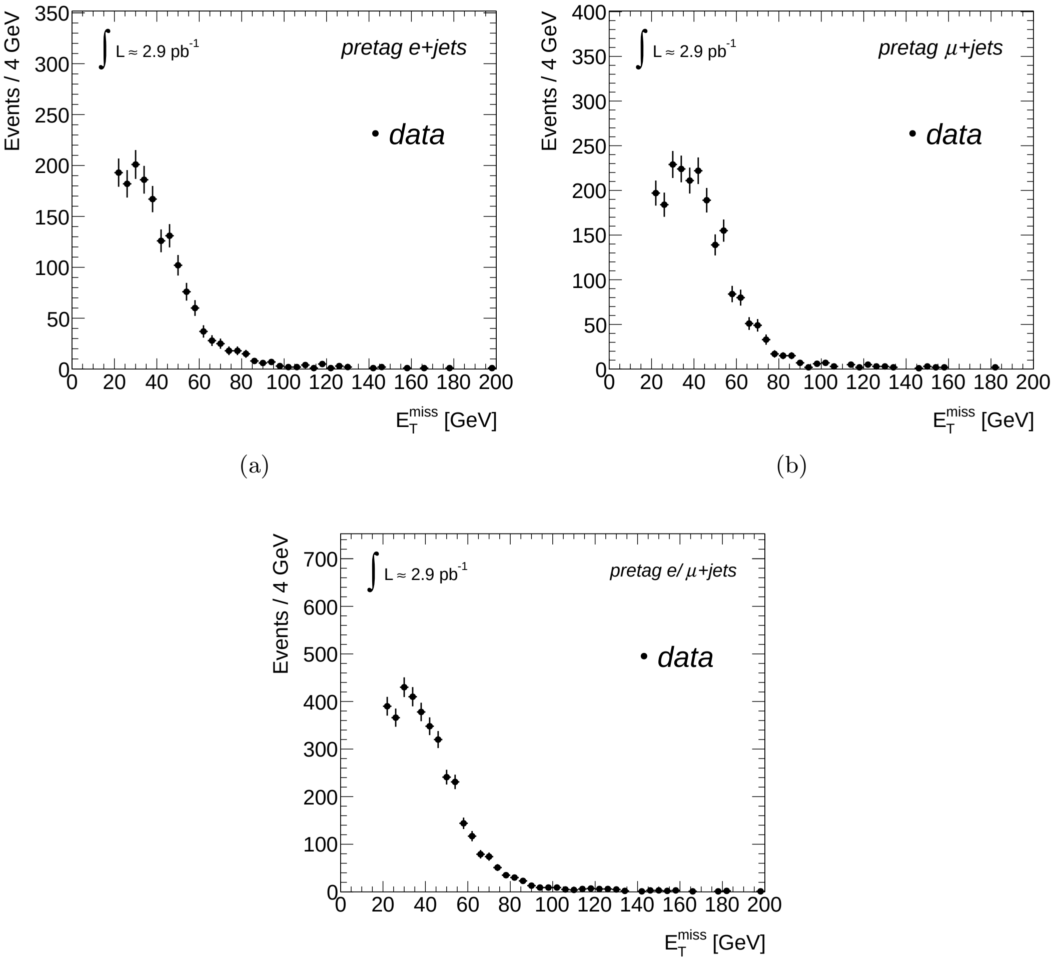

(a)

(b)

(c)

Figure C.3: Distribution of E_T^{miss} for the events passing all pre b-jet tagging event selection criteria in the electron channel (a), muon channel (b) and combining the two channels (c) for events with one or more jets.

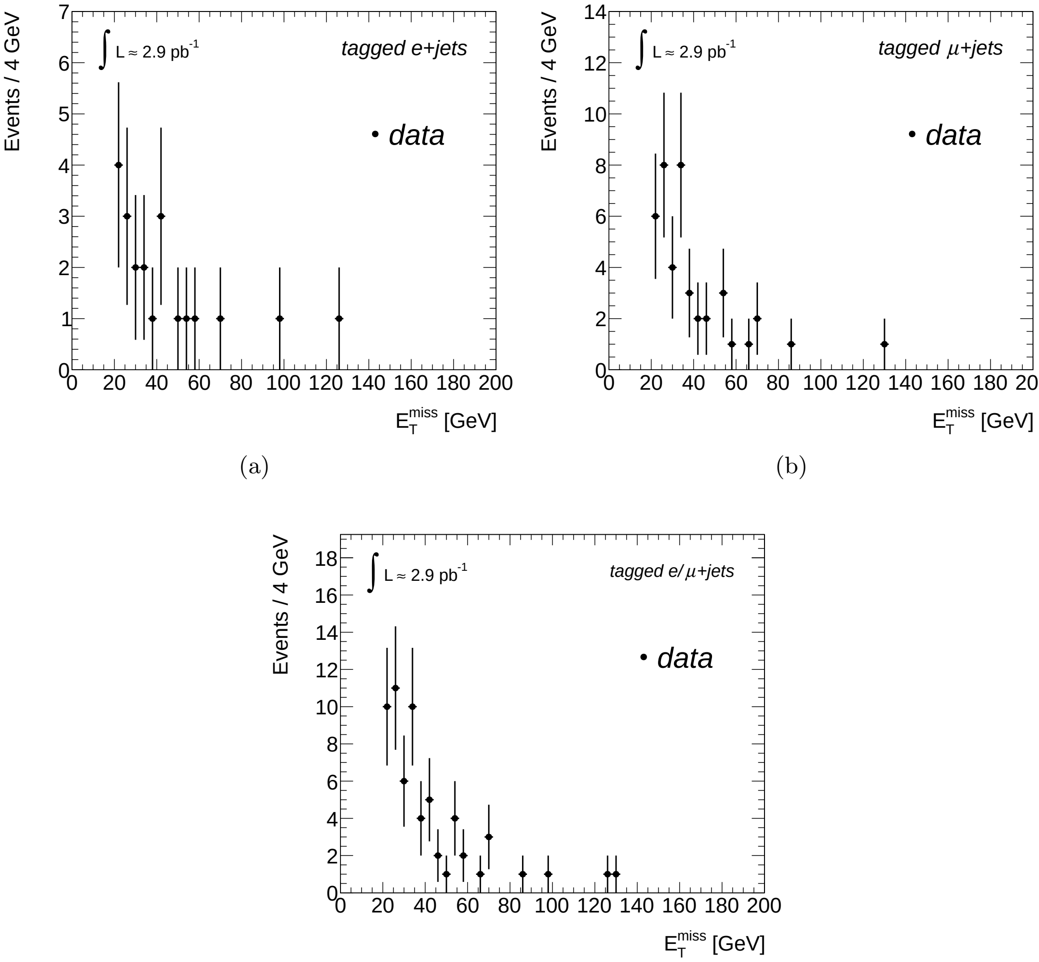

(a)

(b)

(c)

Figure C.4: Distribution of E_T^{miss} for the events passing all event selection criteria, including b-jet tagging, in the electron channel (a), muon channel (b) and combining the two channels (c) for events with one or more jets.

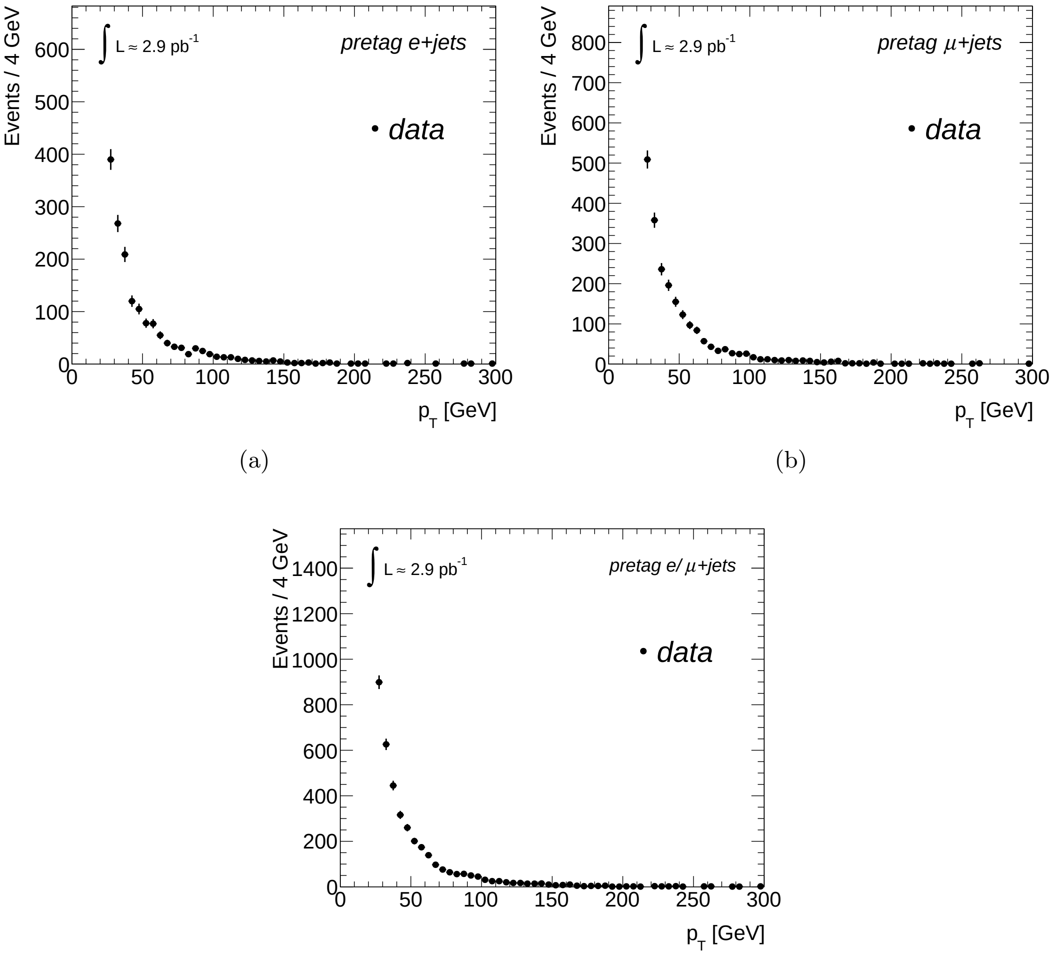

(a)

(b)

(c)

Figure C.5: Distribution of p_T of the leading jet for the events passing all pre b-jet tagging event selection criteria in the electron channel (a), muon channel (b) and combining the two channels (c).

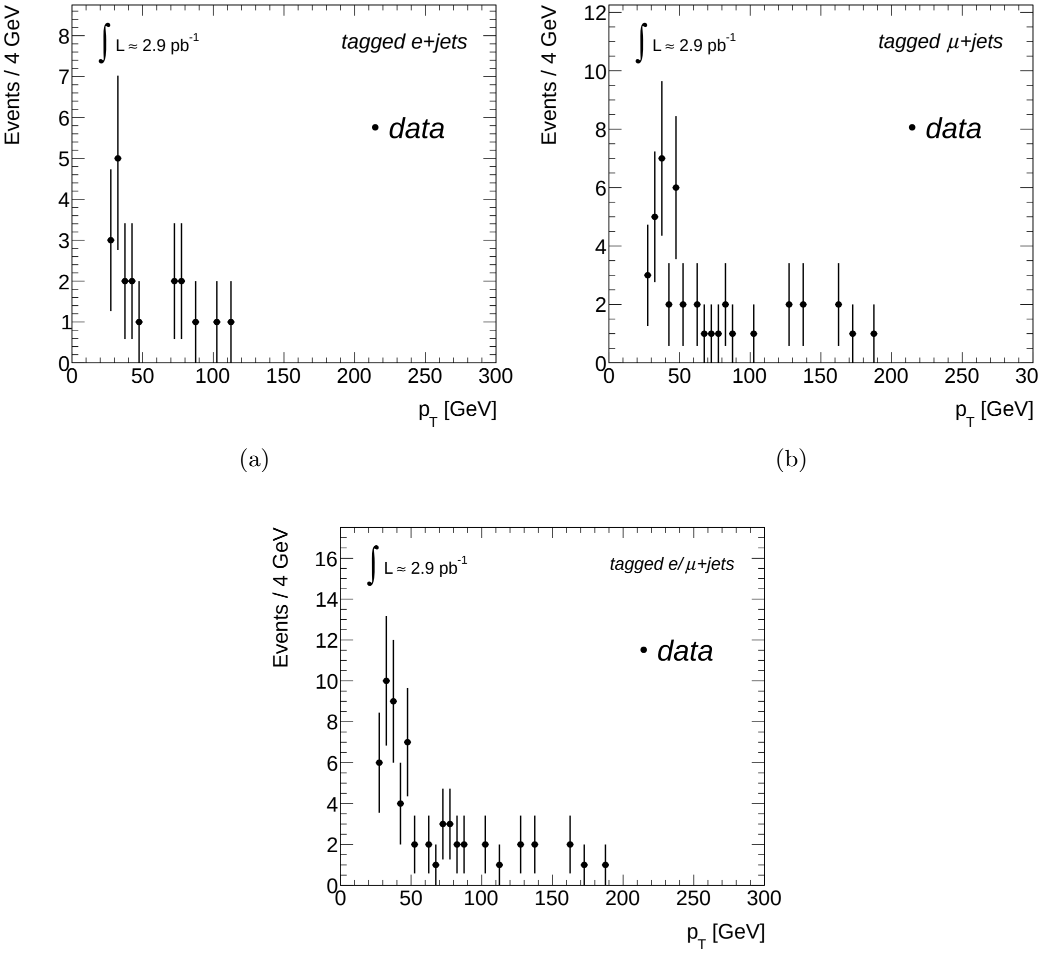

(a)

(b)

(c)

Figure C.6: Distribution of p_T of the leading jet for the events passing all event selection criteria, including b-jet tagging, in the electron channel (a), muon channel (b) and combining the two channels (c).

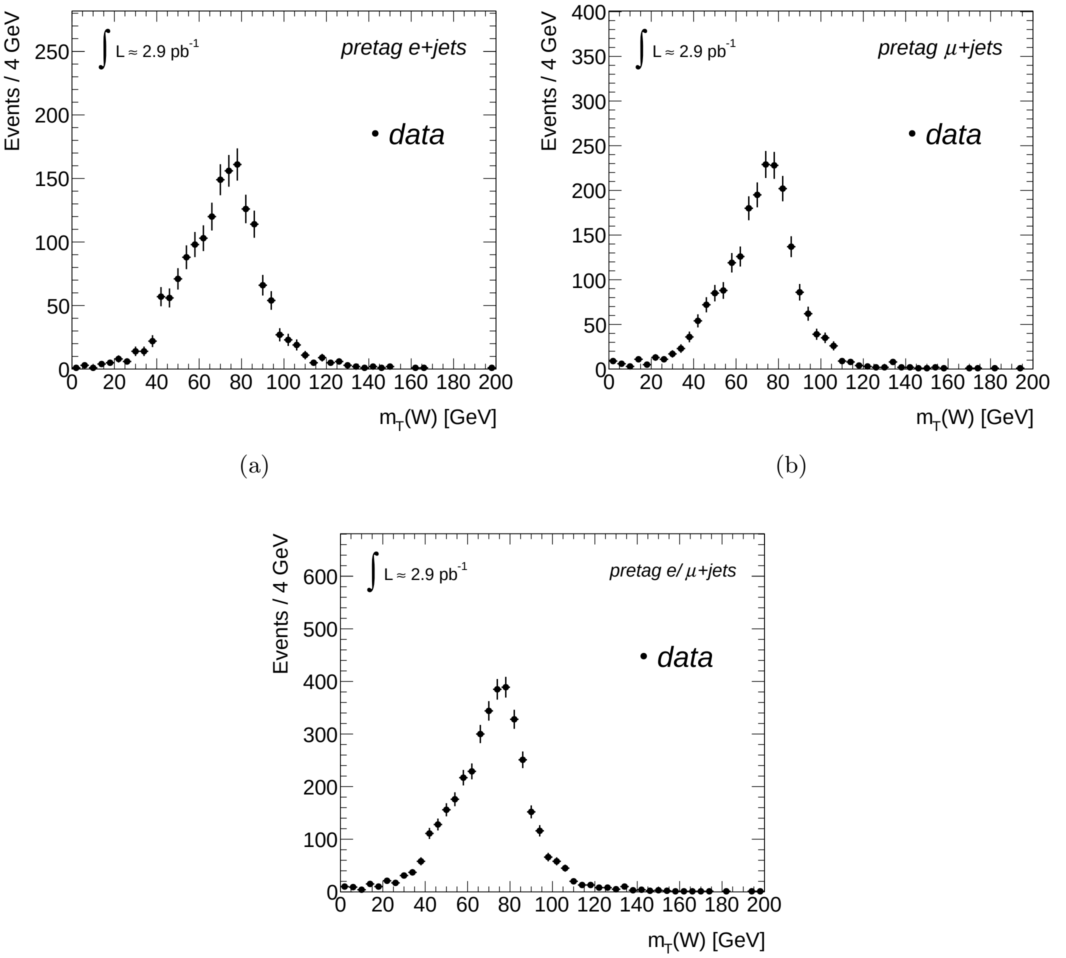

(a)

(b)

(c)

Figure C.7: Distributions showing the W transverse mass for the events passing all pre b-jet tagging event selection criteria in the electron channel (a), muon channel (b) and combining the two channels (c) for events with one or more jets.

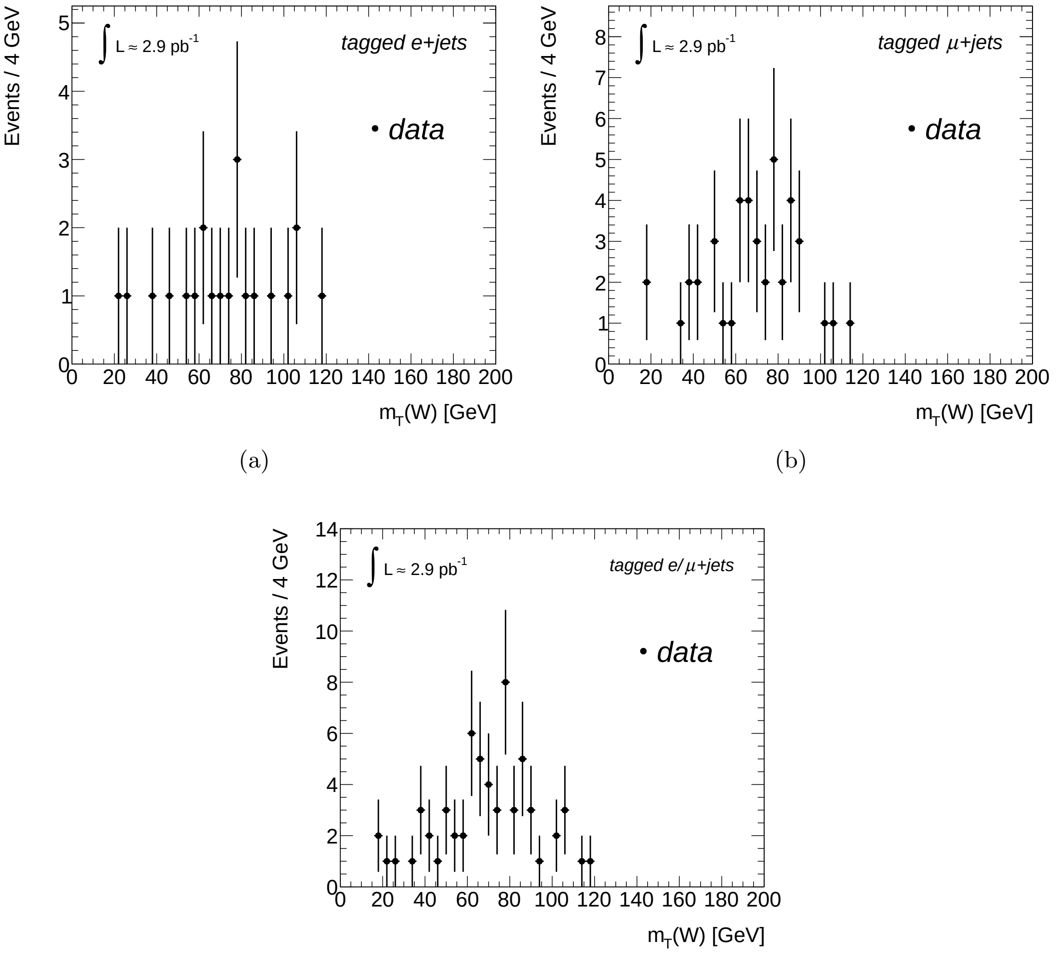

(a)

(b)

(c)

Figure C.8: Distributions showing the W transverse mass after full selection criteria, including b-jet tagging, in the electron (a), muon (b) and combining the two channels (c) for events with one or more jets.